Intermetallics

AD-A269 161

Volume 1 No. 1 1993

ISSN 0966-9795

S DTIC
ELECTE
AUG 3 1 1993
C D

1

FIRST ISSUE

Please Circulate

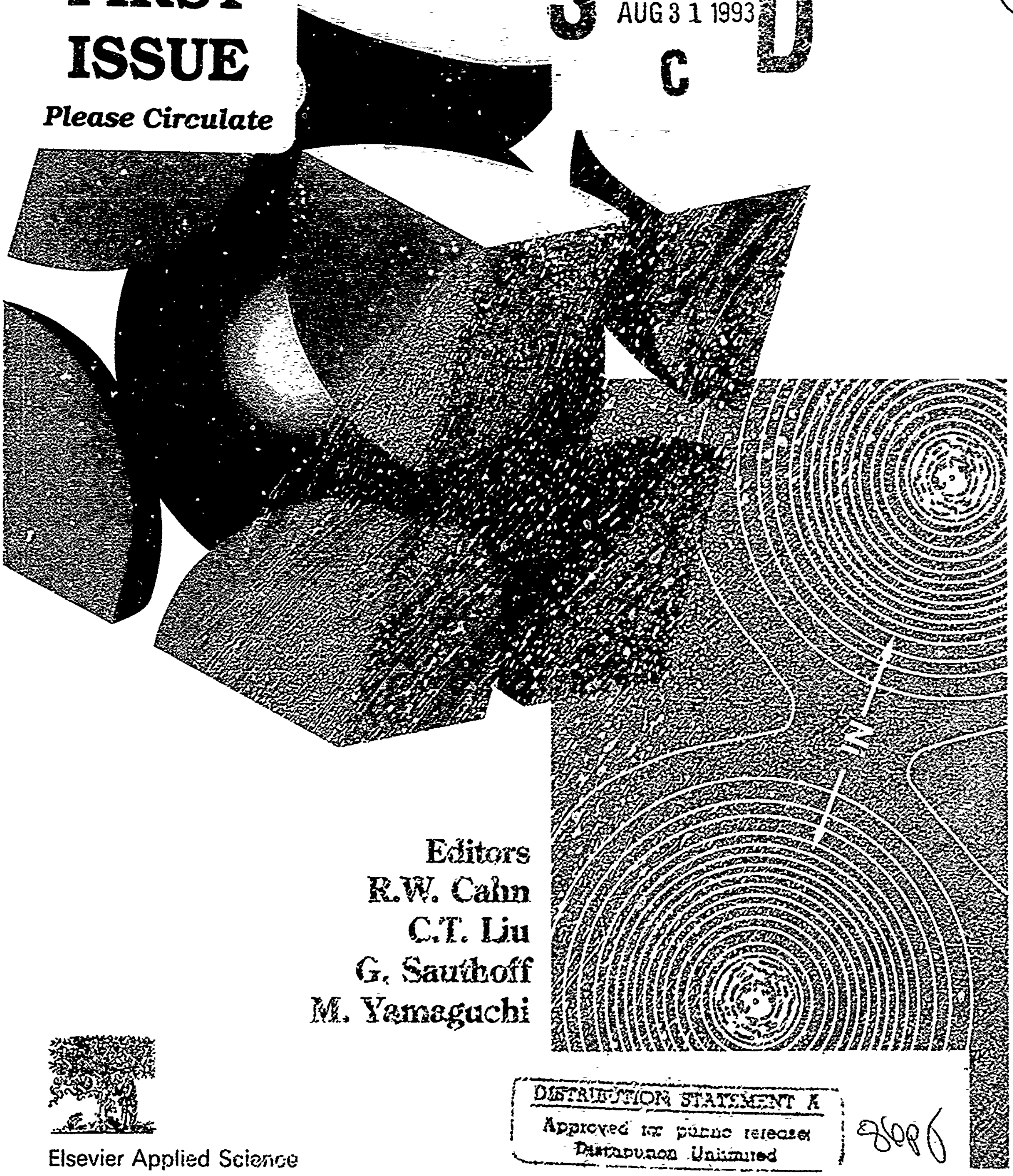

Editors
R.W. Cahn
C.T. Liu
G. Sauthoff
M. Yamaguchi

Elsevier Applied Science

DISTRIBUTION STATEMENT A
Approved for public release;
Distribution Unlimited

8086

INTERMETALLICS

Intermetallics is concerned with all aspects of ordered chemical compounds between two or more metals, notably with their applications.

On the fundamental side, the journal covers: the crystal chemistry and bonding theory of intermetallics; determination of phase diagrams; the nature of superlattices, antiphase domains and order–disorder transitions; the geometry and dynamics of dislocations in intermetallics: theory of flow stress, work-hardening, fatigue and creep; response of deformed intermetallics to annealing; magnetic and electrical properties of intermetallics; structure and property of grain and interphase boundaries; the effect of deviations from stoichiometry on physical and mechanical properties; crystallization of intermetallics from the melt or from amorphous precursors. The principles governing microstructural features of multiphase intermetallic alloys will also be included, as will experimental and theoretical work on diffusion in intermetallics. Papers on metal hydrides will also be accepted.

With regard to application, the journal publishes papers on: all aspects of processing, including melting, casting, fabrication, sintering and hot-pressing and self-sustaining high-temperature synthesis; the microstructural response of multiphase alloys to heat-treatment and the effect of such treatment on properties; environmental effects on mechanical and magnetic properties and their interpretation and control; practical applications of intermetallics; multiphase intermetallic alloys for dental use; hard magnetic material based on intermetallics.

Editors

Professor R. W. Cahn
(*Chairman*)
Department of Materials and Metallurgy, Cambridge University, Pembroke Street, Cambridge, UK, CB2 3QZ

Dr C. T. Liu
Metals and Ceramics Division, Oak Ridge National Laboratory, PO Box 2008, Oak Ridge, TN 37831-6115, USA

Dr G. Sauthoff
Max-Planck-Institut für Eisenforschung, Max-Planck-Str. 1, Postfach 140444, D-4000 Düsseldorf, Germany

Professor M. Yamaguchi
Department of Metal Science and Technology, Kyoto University, Sakyo-ku, Kyoto 606, Japan

Editorial Board

Dr D. L. Anton
United Technologies Research Center, East Hartford, CT, USA

Professor I. Baker
Dartmouth College, Hanover, NH, USA

Professor H. Bakker
Universiteit van Amsterdam, The Netherlands

Dr D. Banerjee
Defence Metallurgical Research Laboratory, Hyderabad, India

Professor Y. A. Chang
University of Wisconsin–Madison, Madison, WI, USA

Professor G. Chen
University of Science and Technology, Beijing, China

Professor W. K. Choo
KAIST, Taejon, Korea

Professor J. M. D. Coey
Trinity College, University of Dublin, Ireland

Dr R. A. Darolia
General Electric Company, Cincinnati, OH, USA

Professor L. Delaey
Katholieke Universiteit Leuven, Belgium

Professor R. Ferro
Università di Genova, Italy

Professor H. L. Fraser
Ohio State University, Columbus, OH, USA

Professor R. M. German
The Pennsylvania State University, University Park, PA, USA

Professor R. Gibala
The University of Michigan, Ann Arbor, MI, USA

Professor G. Gottstein
RWTH, Aachen, Germany

Professor S. Hanada
Tohoku University, Sendai, Japan

Dr S.-E. Hsu
Chung Shan Institute of Science of Technology, Lung-Tan, Taiwan

Dr S. C. Huang
General Electric Corporate R. & D. Schenectady, NY, USA

Dr T. Khan
ONERA, Châtillon, France

Professor N. J. Kim
POSTECH, Pohang, Korea

Professor R. Kratochvil
Charles University, Prague, Czechoslovakia

Dr K. S. Kumar
Martin Marietta Laboratories, Baltimore, MD, USA

Professor D. Lin
Shanghai Jiao Tong University, Shanghai, China

Professor M. H. Loretto
The University of Birmingham, UK

Professor H. Mecking
Technical University of Hamburg, Germany

Dr D. Miracle
Wright Patterson Air Force Base, Dayton, OH, USA

Dr Y. Mishima
Tokyo Institute of Technology, Yokohama, Japan

Professor D. G. Morris
Université de Neuchâtel, Switzerland

Dr Michael V. Nathal
NASA Lewis Research Center, Cleveland, OH, USA

Professor Minoru Nemoto
Kyushu University, Fukuoka, Japan

Professor Kazuhiro Otsuka
University of Tsukuba, Japan

Professor D. G. Pettifor
University of Oxford, UK

Dr I. S. Polkin
All-Russia Institute of Light Alloys, Moscow, Russia

Professor David P. Pope
University of Pennsylvania, Philadelphia, PA, USA

Professor Juan M. Sanchez
University of Texas at Austin, TX, USA

Professor Stephen L. Sass
Cornell University, Ithaca, NY, USA

Dr W. Smarsly
MTU Motoren-und-Turbinen-Union München GmbH, München, Germany

Professor Norman S. Stoloff
Rensselaer Polytechnic Institute, Troy, NY, USA

Dr Takayuki Takasugi
Tohoku University, Sendai, Japan

Dr Masao Takeyama
National Research Institute for Metals, Tokyo, Japan

Professor Yukichi Umakoshi
Osaka University, Japan

Dr Patrick Veyssière
CNRS-ONERA, Châtillon, France

Professor Richard Wagner
GKSS-Forschungszentrum Geesthacht GmbH, Geesthacht, Germany

Dr Michael J. Weaver
Defence Research Agency Aerospace Division, Farnborough, UK

Professor Shyi-Kaan Wu
National Taiwan University, Taipei, Taiwan

Dr Man H. Yoo
Oak Ridge National Laboratory, TN, USA

SUBSCRIPTIONS

1993—One volume, four issues per volume. Subscription price (Volume 1): £154.00/US$293.00. The £ sterling price is definitive. US$ prices are subject to exchange rate fluctuation. All prices include postage and packing. All journals are distributed worldwide by air-speeded delivery at no extra cost to the subscriber. Second class postage paid at Newark, NJ. *Postmaster:* Send all USA address changes to *Intermetallics*, c/o Virgin Mailing and Distribution, Cargo Building 150, Newark International Airport, Newark, NJ 07114, USA.

Subscription orders should be addressed to:

ELSEVIER SCIENCE PUBLISHERS LTD
Crown House, Linton Road, Barking, Essex IG11 8JU, England

In the United States and Canada: For further information contact
Elsevier Science Publishing Co., Inc., Journal Information Center,
655 Avenue of the Americas, New York, NY 10010. Tel. (212) 989-5800

Intermetallics

Volume 1 1993

Editors

Professor R. W. Cahn
(Chairman)
Dr C. T. Liu
Dr G. Sauthoff
Professor M. Yamaguchi

Available for $240.24 from Elsevier Science
Publishing Co. Inc., 52 Vanderbilt Ave.,
New York, NY 10017

JK 8/31/93

Accesion For
NTIS CRA&I ☒
DTIC TAB ☐
Unannounced ☐
Justification ________

By $ 240.24
Distribution /

Availability Codes	
Dist	Avail and / or Special
A-1	21

ELSEVIER APPLIED SCIENCE

DTIC QUALITY INSPECTED 3

93-20132

93 8 27 032

© 1993 Elsevier Science Publishers Ltd

All rights reserved. No part of this publication may be reproduced, stored in a retrieval system, or transmitted in any form or by any means, electronic, mechanical, photocopying, recording, or otherwise, without the prior written permission of the publisher, Elsevier Science Publishers Ltd, Crown House, Linton Road, Barking, Essex IG11 8JU, England.

Special regulations for readers in the USA. This journal has been registered with the Copyright Clearance Center, Inc. Consent is given for copying of articles for personal or internal use, or for the personal or internal use of specific clients. This consent is given on the condition that the copier pay through the Center the per-copy fee stated in the code on the first page of each article for copying beyond that permitted by Sections 107 or 108 of the US Copyright Law. The appropriate fee should be forwarded, quoting the code number at the end of this paragraph, to the Copyright Clearance Center, 21 Congress Street, Salem, MA 01970, USA. If no code appears in an article, the author has not given broad consent to copy and permission to copy must be obtained directly from the author. This consent does not extend to other kinds of copying, such as for general distribution, resale, advertising and promotion purposes, or for creating new collective works. Special written permission must be obtained from the publisher for such copying. 0966-9795/93/$06.00.

Special regulations for authors. Upon acceptance of an article by the journal, the author(s) will be asked to transfer copyright of the article to the publisher. The transfer will ensure the widest possible dissemination of information.

Note. No responsibility is assumed by the Publisher for any injury and/or damage to persons or property as a matter of products liability, negligence or otherwise, or from any use or operation of any methods, products, instructions or ideas contained in the material herein.

Although all advertising material is expected to conform to ethical standards, inclusion in this publication does not constitute a guarantee or endorsement of the quality or value of such product or of the claims made of it by its manufacturer.

Printed in Great Britain by Galliard (Printers) Ltd, Great Yarmouth

Intermetallics 1 (1993) 1

Editorial

We proudly present to our readership this first issue of a new journal devoted to ordered intermetallics in all their numerous ramifications. It is, of course, the product of a close collaboration: the editors, the authors, the editorial advisers and the publisher have all played essential parts. We have every reason to be grateful for the ready and prompt collaboration we have been accorded by all concerned.

The journal is to cover fundamental and applied aspects; mechanical, magnetic and electrical properties; phase equilibria, crystal structure and chemistry, stability calculations, microstructure, dislocation geometry, diffusion; processing, including heat-treatment, environmental effects, applications of many sorts—to cite just the central categories. Clearly, this first issue can exemplify only a few of these fields. Publishers are always constrained during the first year of any new journal to proceed cautiously and need to impose a firm page limit. Accordingly, in 1993 we shall be publishing just four issues averaging 64 pages each, and it will take all four issues for us to be able to demonstrate the breadth of the intended range of the journal. If things continue to progress as well as they have begun, then in 1994 we shall expect to increase the number of pages. Our ambition, which we believe to be realistic, is to ensure a delay of not more than 4–5 months between acceptance of a paper and its publication. We prefer to measure publication time from the date of acceptance, since the rigorous refereeing procedure needed to guarantee quality unavoidably requires additional time: usually, the better written the paper, the shorter the time taken by the referees!

Our editorial advisers are ensuring that we are put in touch with many potential authors, in many countries. Indeed, it is an essential part of our plans for *Intermetallics* that the papers we publish should span the globe, to mark the worldwide research activity in our chosen field. We emphasize, however, that intending authors should feel entirely free to contribute papers direct to the editors; they are very welcome to go through the editorial advisers but they need not do so. We particularly invite potential authors of review articles to write to one or other of the editors, explaining what they have in mind. Review articles will in due course be an important part of *Intermetallics*, and we shall commission them as well as responding to offers.

Finally, feedback from you, our readers, is vital and we hope to hear from you, whether what you have to say is complimentary or otherwise, either direct or via the editorial advisers. We promise that we shall attend to what you have to say.

Robert Cahn
Chain Liu
Gerhard Sauthoff
Masaharu Yamaguchi

Intermetallics 1 (1993)—© 1993 Elsevier Science Publishers Ltd, England. Printed in Great Britain

Intermetallics 1 (1993) 3–20

The effects of chromium on NiAl intermetallic alloys: Part I. Microstructures and mechanical properties

J. D. Cotton

Los Alamos National Laboratory, Los Alamos, New Mexico 87545, USA

R. D. Noebe

NASA—Lewis Research Center, Cleveland, Ohio 44135, USA

&

M. J. Kaufman

University of Florida, Gainesville, Florida 32611, USA

(Received 1 October 1992; accepted 8 January 1993)

The effects of Cr on the microstructure and mechanical properties of NiAl have been characterized. It is shown that Cr is an efficient solid solution strengthener in NiAl, effectively tripling the 0·2% yield strength at the 1 at. % level; this is also its maximum solubility. The presence of Cr also increases the BDTT of NiAl by approximately 150K and reduces the already limited ductility to essentially zero. Larger alloying additions produce fine α-Cr precipitation. However, the associated hardening contribution due to precipitation is relatively minor compared with solid solution effects. Independently of Cr content, stoichiometric deviation was observed to produce significant increases in strength and BDTT. It is shown that hardening due to both intrinsic and extrinsic substitutional defects is ultimately a function of the solubility, site preference, and alloying strategy (e.g., a particular Ni/Al ratio, or Cr substituted solely for either Ni or Al) of the Cr addition.

Key words: nickle aluminides, solid solution strengthening, brittle–ductile transition, atomic site preference, Hall–Petch Analysis

INTRODUCTION

Intermetallic-base alloys are being considered for elevated-temperature structural applications—in particular, for jet turbine engine components. Of the many intermetallic compounds available, NiAl is especially attractive due to its ease of production, the low cost of its components, and its property advantages relative to superalloys. These include low density, high thermal conductivity, high melting point and good cyclic oxidation resistance.[1–3] Therefore, if alloys based on NiAl are successfully developed, substantial increases in engine performance and efficiency may be realized.

β-NiAl has the simple cubic B2 (CsCl) structure, which is similar to the body-centred-cubic structure. Strong directional bonding between Ni and Al atoms in the $\langle 111\rangle$ directions exists,[4,5] and has important implications with respect to plastic deformation in NiAl, as addressed in Part II.[6] NiAl also exists over a wide composition range (more than 20 atomic percent (at.%) at 1673K), as shown by the Ni–Al binary phase diagram in Fig. 1.[7] Since NiAl is a Hume–Rothery β electron compound (electron-to-atom ratio $\leq 1{\cdot}5$),[8,9] deviations from stoichiometry are accommodated by the substitution of Ni atoms onto Al sites (antisite defects) in Ni-rich compositions and by the formation of Ni vacancies in Al-rich compositions.[10] Both types of constitutional point defects are potent strengthening agents.[11]

One critical shortcoming of NiAl in structural applications is its low ductility and toughness at temperatures below its brittle-to-ductile transi-

Intermetallics 0966-9795/93/$6.00 © 1993 Elsevier Science Publishers Ltd, England. Printed in Great Britain

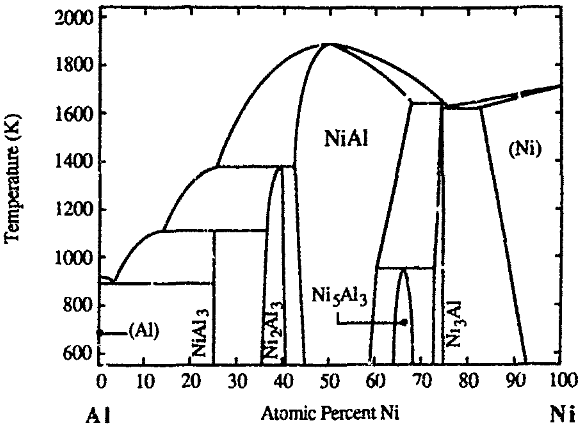

Fig. 1. Binary Ni–Al phase diagram. After Ref. 7.

tion temperature (BDTT).[1,12–15] Usually, less than about 2% tensile elongation is observed at ambient temperatures, depending upon purity, processing and composition, while extensive deformation is possible above the BDTT.[13,16–18] Strength and ductility are also markedly affected by the composition of the compound, with a maximum in ductility and a minimum in flow strength observed at the stoichiometric composition. Another shortcoming is the lack of strength above the BDTT. However, recent work has shown that elevated temperature strength may be enhanced by composite reinforcement[19–22] or ternary alloying additions,[1,2,23–25] although usually at the expense of ductility.

Moderately tougher NiAl-based materials have been produced by macro-alloying with additions to produce multiphase microstructures, such as $\beta + \gamma'$ or $\beta + (\gamma + \gamma')$;[26–29] however, this approach also increases density while decreasing melting point, oxidation resistance and, often, creep strength, thereby negating many of the original advantages of NiAl. In these types of structures, toughening relies upon crack blunting, deflection, and slip transfer by the more ductile second phase. Another similar approach results from the existence of a number of pseudobinary eutectic systems, which include β-NiAl and a body-centred-cubic refractory metal phase (e.g. V, Cr, Mo, W or Re).[30–35] These systems can result in rod or lamellar eutectic microstructures, for which some degree of toughening has been observed.[3,36] Still, this approach also requires sacrifices in melting point, density and oxidation resistance.

Ideally, the low temperature ductility of NiAl should be improved by altering or enhancing the basic process of plastic deformation, without detracting from its other essential properties. Important parameters which influence plastic deformation by slip are activation of five independent slip systems, ease of dislocation nucleation, dislocation mobility and ease of slip transferal across structural boundaries. All of these processes are necessary to achieve tensile plasticity at temperatures where diffusive mechanisms are unimportant. NiAl slips along $\langle 100\rangle\{011\}$ and/or $\langle 100\rangle\{001\}$ systems, which results in a maximum of three independent slip systems for general deformation.[37,38] As a result, one emphasis of current research on NiAl is to increase the number of independent slip systems through alloying. To this end, Law and Blackburn reported[39] that the addition of about 5 at. % Cr to NiAl caused the preferred slip system to shift from $\langle 100\rangle\{011\}$ to $\langle 111\rangle\{112\}$, thereby providing the five independent slip systems necessary to satisfy the Von Mises criterion.[37] However, limited mechanical testing in the same investigation showed that the Cr-containing alloy remained brittle, more so in fact, than binary, stoichiometric NiAl.

These observations raise several important questions. First, why are the above alloys brittle if they deform by $\langle 111\rangle$ slip? Secondly, how and to what extent does Cr causes the slip system to shift from $\langle 100\rangle\{011\}$ to $\langle 111\rangle\{112\}$?. And finally, what is the effect of Cr on the microstructure and the resulting mechanical properties of NiAl? There are also related questions with regard to the solubility of Cr in NiAl, its site preference, α-Cr precipitation and point defect hardening in the β-NiAl phase. Many of these issues are not well understood, particularly solid solution hardening in intermetallic compounds.[40]

Two recent studies on the effects of Cr on directionally-solidified[41] and single crystal[25] NiAl-based alloys suggest that enhanced $\langle 111\rangle$ dislocation activity in [001]-oriented crystals may be due to greater hardening of the $\langle 100\rangle\{011\}$ systems over the $\langle 111\rangle\{112\}$ system in the alloyed compound. However, since both of these studies were conducted on crystals oriented to discourage $\langle 100\rangle$ slip, alternate slip vectors, such as $\langle 111\rangle$, are to be expected[42-47] and Law and Blackburn's results,[39] which were for polycrystals, are not corroborated. Furthermore, neither study examined a sufficient composition range within the ternary system to determine the effects of Cr level, Ni/Al ratio (stoichiometry), α-Cr precipitation and impurity content on strength, or the effect of site preference on solubility. These factors are also important because they control or restrict glide process.

This work is divided into two parts. Part I examines the effects of Cr on the microstructure and

Table 1. Nominal compositions (at. %) of cast and homogenized alloys

Alloy number	Ni (%)	Al (%)	Cr (%)	Wt loss (%)	Ni/Al ratio
1	52	48	0	−0·11	1·083
2	50	50	0	−0·07	1·000
3	48	52	0	−0·09	0·923
4	52	47	1	−0·19	1·106
5	50	49	1	−0·18	1·020
6	49·5	49·5	1	−0·32	1·000
7	49	50	1	−0·22	0·980
8	47	52	1	−0·17	0·904
9	50	48	2	−0·20	1·042
10	49	49	2	−0·14	1·000
11	48	50	2	−0·41	0·960
12	50	45	5	−0·33	1·111
13	47·5	47·5	5	−0·20	1·000
14	45	50	5	−0·24	0·900
15	46·3	48·5	5·2	na	0·953

na = not analyzed.

mechanical properties of NiAl as a function of ternary composition, processing route and test temperature. Both tensile and compressive properties, as well as hardness, are interpreted in terms of various strengthening mechanisms and related to microstructure. Part II reports the effect of Cr in modifying the slip behavior of NiAl at room temperature by a thorough microstructural characterization of the dislocations present both before and following plastic deformation.[6]

EXPERIMENTAL

Materials

Fifteen castings and five extrusions were characterized in this study, the compositions of which are shown in Tables 1 and 2. The compositions were chosen to produce three different alloy series in which Cr was substituted for either Al, Ni, or both components equally. The alloys studied are plotted in the ternary phase diagram in Fig. 2.

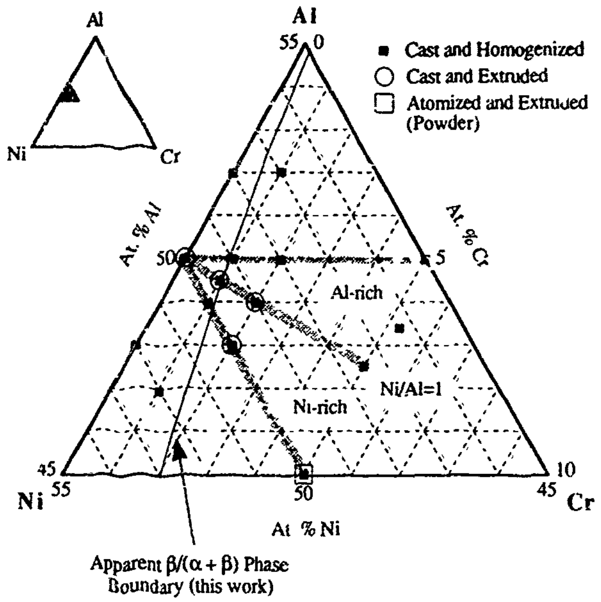

Fig. 2. Ternary diagram showing alloy compositions of the current study. Note that the temperature of the $\beta/(\alpha+\beta)$ boundary cannot be specific since the alloys were not quenched from the homogenization temperature. See text for details.

Five of the casting compositions coincided with the extrusion compositions. The castings were produced by nonconsumable arc melting 0·070 kg of constituent elements (99·95 wt % Ni, 99·999 wt % Al, 99·99 wt % Cr) in a water-cooled copper-bowl under Al to produce buttons, and then inverting and remelting twice more to promote homogeneity. The buttons were then cast into a Cu mold to produce 50 mm × 13 mm × 13 mm rectangular castings with a small hot top to reduce pipe shrinkage.

Total weight losses for each casting were less than 0·5%, indicating the actual compositions were very close to the intended compositions. The castings were then homogenized by heating under slow-flowing commercial purity argon gas for 24 h at 1673K, using heating and cooling rates of 0·083K s^{-1}. Twenty-one other compositions were also produced by casting and homogenization, as

Table 2. Nominal and analyzed compositions (at. % or wppm) of extruded alloys

		Nominal			Analyzed						
Extrusion number	Billet type	Ni (%)	Al (%)	Cr (%)	Ni (%)	Al (%)	Cr (%)	Fe (%)	C (wppm)	N (wppm)	O (wppm)
1	VIM cast	50	50	0	50·2	49·8	na	na	82	nd	42
2	VIM cast	49·5	49·5	1	49·7	49·3	0·94	na	110	na	35
3	VIM cast	49	49	2	49·2	49·9	1·9	na	79	na	38
4	VIM cast	50	48	2	50·1	48·0	1·9	na	70	na	42
5	Powder	50	45	5	50·9	44·6	4·4	0·08	21	nd	120

nd = not detected (less than 0·2 wppm).
na = not analyzed.

described above, for the sole purpose of microhardness testing.

The extrusions were produced by induction melting 1 kg charges of constituent elements together under vacuum to make 150 mm × 50 mm diameter billets. One composition, Ni–45Al–5Cr, was vacuum atomized by Homogeneous Metals, Inc., to produce prealloyed powder. The cast billets (or powder) were enclosed in 1018 steel cans by tungsten–inert gas welding. The cans were then evacuated and sealed by electron beam close-out welds. Each canned alloy was heated at 1400K for 4 hr and then extruded in a Loewy vertical hydraulic 340 ton press at a 16:1 reduction ratio. The extruded product was cut into 50 mm lengths and the steel can chemically removed by immersion in an aqueous solution of 50 vol. % HNO_3 and 2 vol. % of H_2SO_4 for 1 h at 300K. The composition of each extrusion was verified by plasma analysis and found to be within experimental error of the intended composition, as shown in Table 2.

Metallography

Transverse cross-sections of the castings and transverse and longitudinal sections of the extrusions were removed by abrasive wheel cutting and metallographically prepared using standard mounting, grinding and polishing procedures. Optical microstructures were revealed by etching with saturated molybdic acid (0·100 kg MoO_3, 50 ml HF and 150 ml H_2O) for 10–120 s. Light optical micrographs were recorded using both bright field (BF) and differential interference contrast (DIC) to illuminate particular microstructural features.

Transmission electron microscopy

Compression specimens were sliced into disks approximately 300 μm thick with a low-speed Buehler saw using 250 μm thick SiC blades lubricated with water. Each disk was then wet ground by hand on 600 grit SiC paper to approximately 150 μm thickness and then twin jet-electropolished to perforation in a solution of 6 vol.% perchloric acid, 10% butyl cellusolve, 14% H_2O and 70% ethanol, at 273K, 32 V and 150 mA using a Struers TENUPOL-3 polishing unit. The pumping speed of the jets was minimized to avoid damage to the foils on perforation.

All observations were made on a JEOL 100C transmission electron microscope (TEM) operated at an accelerating voltage of 120 kV with a double-tilt stage allowing ± 60°C and ± 30° tilts. The microstructures were generally characterized in terms of the type and distribution of phases present. In addition, a determination of the site preference of Cr on the NiAl lattice was made by axial atom location by channelling enhanced microanalysis (ALCHEMI)[48] of a TEM specimen of extruded Ni–49·5 Al–1Cr along the [110] axis. This alloy was chosen because the Cr was entirely in solid solution, which prevented error due to the fluorescence of α-Cr precipitates.

Compression testing

Compression specimens were produced from each cast or extruded alloy by either electrostatic discharge machining (EDM) or centerless grinding to approximate dimensions of 6·0 mm in length by 3·0mm diameter. At least four compression tests were conducted to failure, or to well beyond the yield point for each composition. Failure was considered to have occurred upon observation of the first discontinuity in the load–displacement curve, regardless of any subsequent increase in load. The 0·2% offset compressive yield strength (CYS), ultimate compressive strength (UCS) and strain-to-fracture (ε_p) were calculated from the load-time charts, assuming volume constancy and correcting for machine compliance. All test were conducted at 300K in an Instron load frame, at approximately $1{\cdot}3 \times 10^{-4}\ s^{-1}$ strain rate. In specimens designated for Burger's vector analysis, less than 1% strain was usually applied, as measured directly from the change in specimen length, since larger strains produced a dislocation density that was too high for individual analysis on the TEM.

Tensile testing

Bottonhead tensile specimens of 3·2 mm diameter and 30 mm gauge length were machined from the extruded rods by centerless grinding followed by electropolishing to remove surface defects. The same Instron load frame and parameters were used as described for the compression tests. In addition, a series of elevated temperature tests were conducted to determine the BDTT of each extruded composition using a three-zone resistance furnace in air.

Microhardness testing

Microhardness determinations were made on each cast and homogenized composition with a Buehler

Micromet III microhardness testing machine using a calibrated Vickers indenter. The indenter load was 0·5 kg, with a load duration of 15 s. The specimens were metallographically prepared (unetched) prior to indentation and were indented 10 to 15 times in five well-separated areas on each cross-section. Each indentation was optically examined for cracking or subsurface prior to measurement; any questionable indentations were disregarded. The resulting compilation of hardness values was average for each alloy.

RESULTS

Microstructural analysis

Cast and homogenized alloys

Figure 3 shows representative optical micrographs of the cast and homogenized alloys. The microstructures may be categorized as single phase, as containing fine (less than 1 μm diameter) precipitates, or as containing slightly larger precipitates (approximately 1 μm diameter). In the first category are the three binary alloys and the ternary alloys containing 1% Cr. An example of single phase microstructures is shown in Fig. 3(a). Compositions which contained fine precipitates, such as Ni–49Al–2Cr and Ni–50Al–2Cr, are typified by Fig. 3(b). The NiAl grain boundaries were heterogeneous nucleation sites for second phase precipitation and the precipitates are coarser in those regions. Figures 3(c) and (d) show typical cast and homogenized microstructures of the 5% Cr alloys, which had the largest precipitates. One interesting feature of the two-phase alloys, particularly those containing 50% Al, is the tendency of the precipitates to be aligned in discrete rows. The rows were not associated with grain or subgrain boundaries or any other feature which might provide an easy nucleation site. The microstructure of Ni–48·5Al–5·2Cr, the composition previously reported[39] to display ⟨111⟩ slip, was similar to that of Ni–45Al–5Cr, Fig. 3(c).

The TEM results generally supported the optical microscopy observations. Typical electron micrographs of deformed cast specimens are shown in Figs. 4–8 (ε_p indicates the amount of

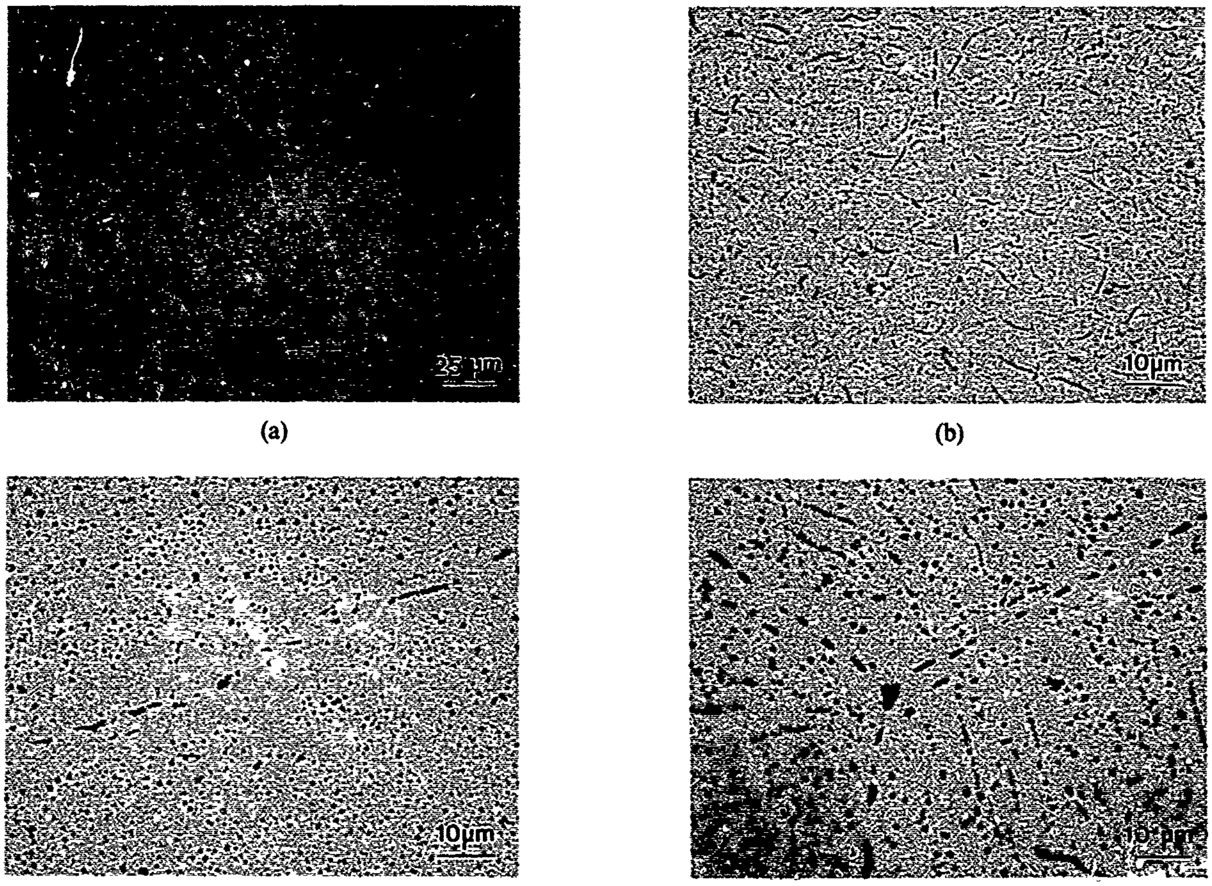

(a) (b)

(c) (d)

Fig. 3. Optical microstructures of cast and homogenized NiAl–Cr Alloys. (a) Ni–48Al; (b) Ni–50Al–2Cr; (c) Ni–45 Al–5Cr; (d) Ni–50Al–5Cr.

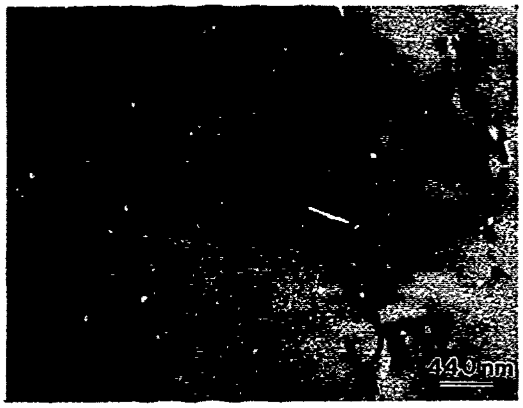

Fig. 4. Transmission electron microscope bright field (TEMBF) image of cast and homogenized Ni–50Al ($\varepsilon_p = 0{\cdot}3\%$).

deformation beyond 0·2% strain). All cast and homogenized alloys exhibited very large grains, typically 5000 μm, such that few grain boundaries were encountered during TEM analysis. The binary alloys were confirmed to be single phase, with only Ni–50Al containing a significant dislocation density (Fig. 4). These dislocations were generally homogeneously distributed in the form of elongated loops or short, bent segments.

Of the alloys containing 1% Cr, alloys with less than 50% Al were confirmed to be single phase; however, the Ni–50Al–1 Cr alloy contained a fine dispersion of spherical and rod-like α-Cr precipitates, approximately 50 nm in diameter, which were not visible by optical metallography–Fig. 5 (see also Fig. 4 in Part II). The precipitates were associated with what appeared to be prismatically-punched dislocation loops and frequent tangles at the precipitate–matrix interface. Within the matrix, bent dislocation segments and small dislocation loops were observed.

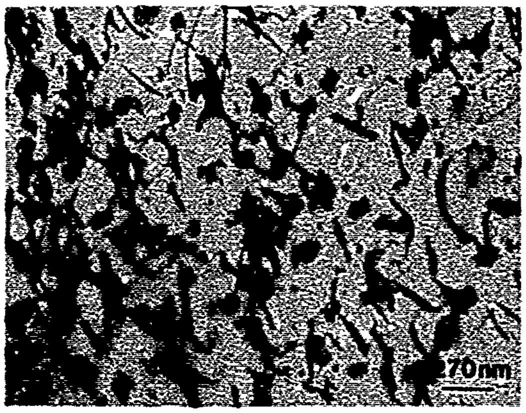

Fig. 5. TEMBF image of cast and homogenized Ni–50Al–1Cr ($\varepsilon_p = 0{\cdot}7\%$).

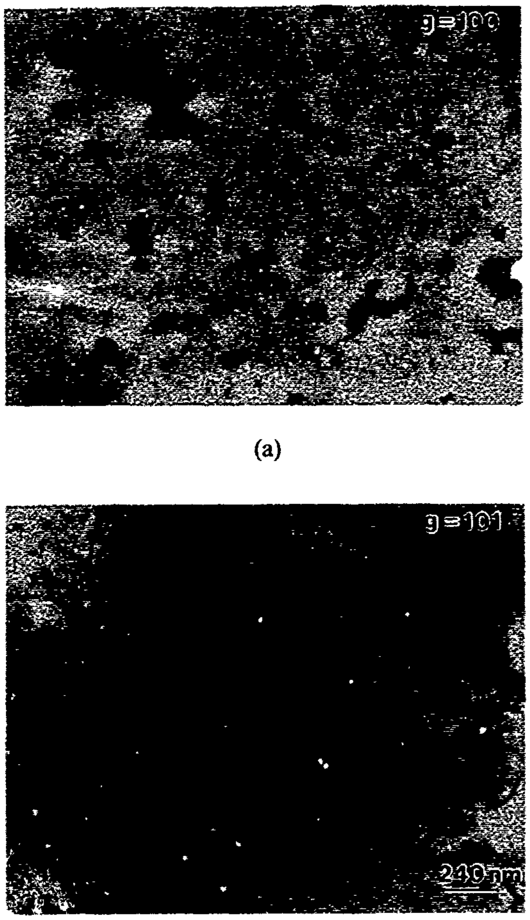

Fig. 6. TEMBF images of cast and homogenized Ni–50 Al–2Cr ($\varepsilon_p = 0{\cdot}2\%$). (a) precipitate coherency is indicated by strain contrast; (b) dislocation segments pinned by precipitates.

The cast alloys with 2% Cr contained spherical precipitates of α-Cr, as shown in Fig. 6. The precipitation in these alloys appear to be of a narrow size distribution, 10 to 50 nm diameter, although somewhat larger precipitates were sometimes noted in Ni–49Al–2Cr and Ni–50Al–2Cr. The larger precipitates were often associated with dislocation tangles, while the smaller precipitates appeared to pin matrix dislocations. The precipitation was semicoherent or coherent, as demonstrated by the 'double-arced' strain contrast surrounding the precipitates in Fig. 6(a).

Cast alloys containing 5% Cr, i.e. Ni–45Al–5Cr, Ni–47·5Al–5Cr, Ni–48·5Al–5·2Cr and Ni–50Al–5Cr, exhibited more extensive α-Cr precipitation than the Cr-leaner alloys–Fig. 7 and 8. Precipitation in the first two alloys was generally bimodal in size distribution, with typical diameters of 10–25 nm and 500 nm. The finer precipitates were spherical, while the coarser precipitates were often irregular or blocky in morphology (Figs 7(c) and 8), and may have resulted from incomplete dissolution of the interdendritic α–Cr during homogenization. Precipitation in Ni–50Al–5Cr was trimodal in size

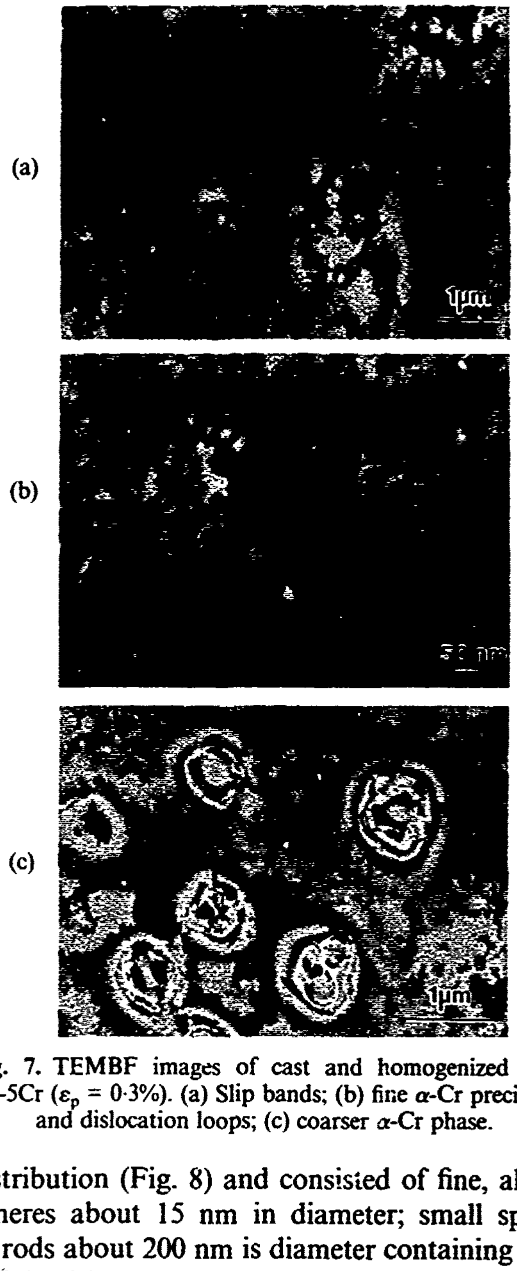

Fig. 7. TEMBF images of cast and homogenized Ni-45 Al-5Cr (ε_p = 0·3%). (a) Slip bands; (b) fine α-Cr precipitates and dislocation loops; (c) coarser α-Cr phase.

distribution (Fig. 8) and consisted of fine, aligned spheres about 15 nm in diameter; small spheres or rods about 200 nm is diameter containing interfacial dislocation networks; and large, aligned α–Cr particles of approximately square cross-section (about 1 μm in width) with interfacial dislocation networks. The orientation relationship between the α-Cr precipitates and the β-NiAl matrix was determined to be 'cube-on-cube,' i.e. $\langle 100\rangle_\alpha\{001\}_\alpha // \langle 100\rangle_\beta\{001\}_\beta$; see Fig. 8. Pinning of matrix dislocations by the finest precipitates was observed in all the 5% Cr alloys.

Cast and extruded alloys

The longitudinal optical microstructures of the as-extruded alloys are shown in Fig. 9. The Ni-50Al and Ni-49·5Al-1Cr alloys both contained fully recrystallized structures of nearly equiaxed grains, which have probably also undergone some degree of grain growth following extrusion,—Figs 9(a)

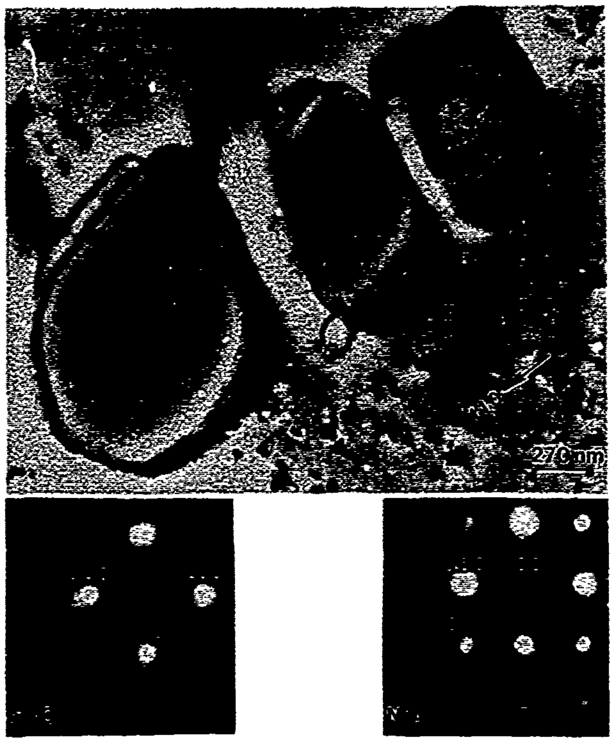

Fig. 8. TEMBF images of cast and homogenized Ni-50 Al-5CR (ε_p = 0·4%). (a) α-Chromium precipitation and dislocations; (b) SADPs demonstrating cube-on-cube orientation relationship between NiAl matrix and α-Cr precipitates.

and (b). The Ni-48Al-2Cr and Ni-49Al-2Cr alloys, which were very similar, Figs 9(c) and (d), were also recrystallized, but to a less advanced stage owing to grain boundary pinning by α-Cr precipitates. The extruded powder alloy, Ni-45Al-5Cr, displayed the finest grain structure and was fully also recrystallized, Fig. 9(e). Stringers of second phase extending in the extrusion direction could be discerned in the latter three alloys.

TEM of the extruded alloys revealed a fine structure, with grains typically 10 to 20 μm in diameter and a tendency towards a ⟨111⟩ fiber texture. The microstructure of as-extruded Ni-50Al was generally featureless, with the exception of a small number of dislocation loops and short segments. The Ni-49·5Al-1Cr extruded alloy was also single phase (Fig. 10). Room-temperature compressive deformation (0·6% strain) of Ni-49·5Al-1Cr produced concentrated slip bands emanating from the grain boundaries Fig. 10(b). This is confirmed by the presence of dislocation half-loops with both ends attached to the boundary, also shown in Fig. 10(b).

The Ni-48Al-2Cr and Ni-49Al-2Cr alloys were similar with respect to microstructure and dislocation substructure. Dense, homogeneous

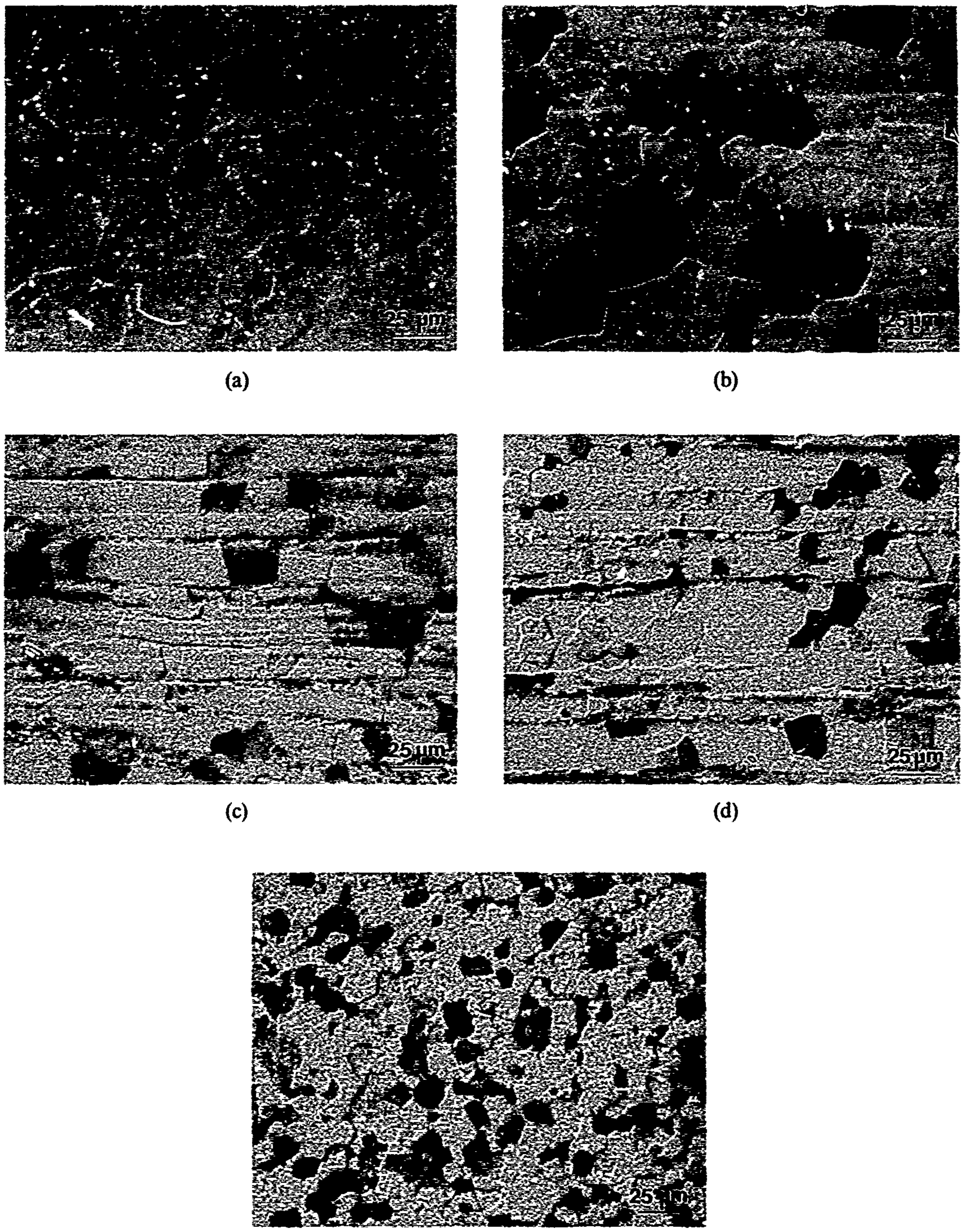

(a) (b) (c) (d) (e)

Fig. 9. Optical microstructures of extruded NiAl and NiAl–Cr alloys. Longitudinal sections: (a) Ni–50Al; (b) Ni–49·5 Al–1Cr; (c) Ni–48 Al–2Cr; (d) Ni–49 Al–2Cr; (e) Ni–45 Al–5Cr.

precipitation of 25 nm diameter α-Cr particles was observed throughout, as shown in Fig. 11. Numerous slip bands have nucleated at grain boundaries, and appear to extend into the grain centers after room temperature deformation (Fig. 2 in Part II). Within the slip bands, small ⟨100⟩ dislocation loops, 10 to 20 nm in diameter, were observed and appeared to be single Orowan bypass loops surrounding the fine α-Cr precipitates.

The extruded Ni–45Al–5Cr alloy contained a higher volume fraction of α-Cr precipitation than the previous alloys, Fig. 12, although the precipitate diameter was similar. Room temperature deformation (0·6% strain) increased the dislocation density, but in a more homogeneous fashion than the other alloys, with fewer slip bands and more evenly spaced dislocations (Fig. 12(b)). Dislocation pinning by the precipitates was

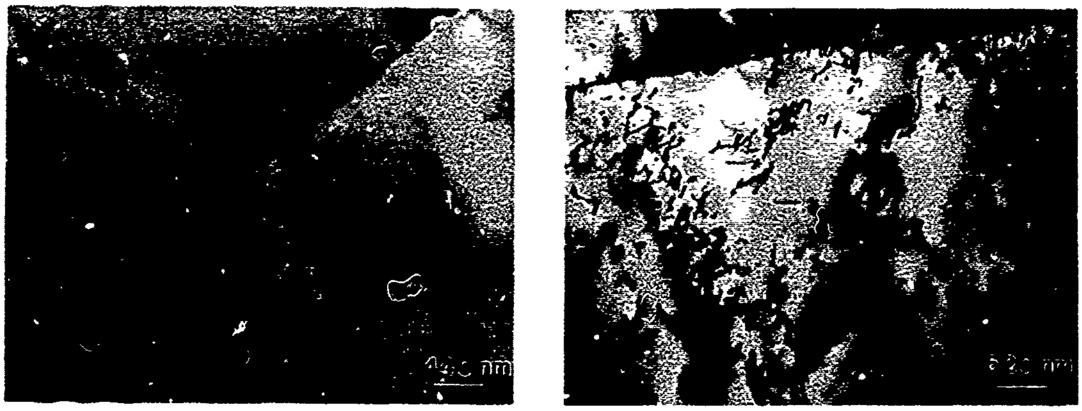

(a) (b)

Fig. 10. TEMBF of extruded Ni—49·5 Al—1Cr. (a) As-extruded; (b) deformed 0·7 in compression at 300 k.

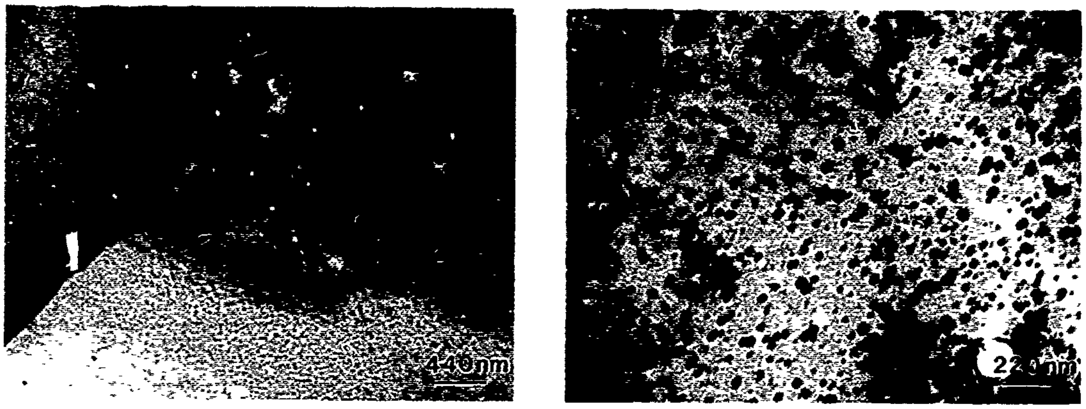

(a) (b)

Fig. 11. TEMBF of as-extruded Ni–49 Al–2Cr. (a) Triple point grain boundary; (b) fine α-Cr precipitation.

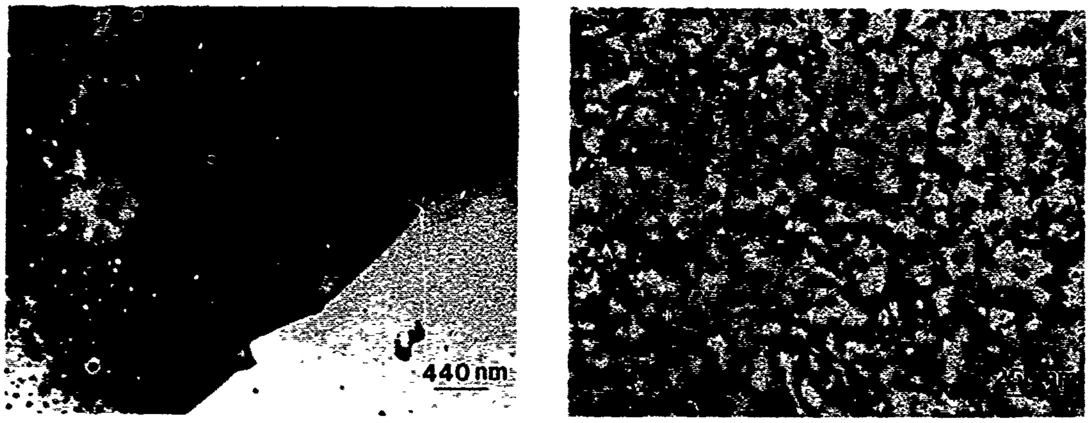

(a) (b)

Fig. 12. TEMBF of extruded Ni–45 Al–5Cr. (a) As-extruded; (b) deformed 0·6% in compression at 300K.

observed, as were dislocation loops, which occasionally surrounded the precipitates.

The microstructural observations may be summarized by the line in Fig. 2 as an apparent NiAl/(NiAl + α-Cr) 'solvus' trace. However, since the specimens were not quenched from the homogenization temperature, this boundary only approximates the general shape of the true phase boundary at some unknown intermediate temperature. Nonetheless, it provides an upper bound for the solubility of Cr in NiAl at near-ambient temperatures. Thus, the apparent solubility of Cr in NiAl varies with the Al (or Ni) content, being higher for lower Al percentages. This implies that Cr has a site preference for Al, which was confirmed by the ALCHEMI results plotted in Fig. 13 for the extruded Ni–49·5Al–1Cr alloy determined along the [110] zone axis. Since the

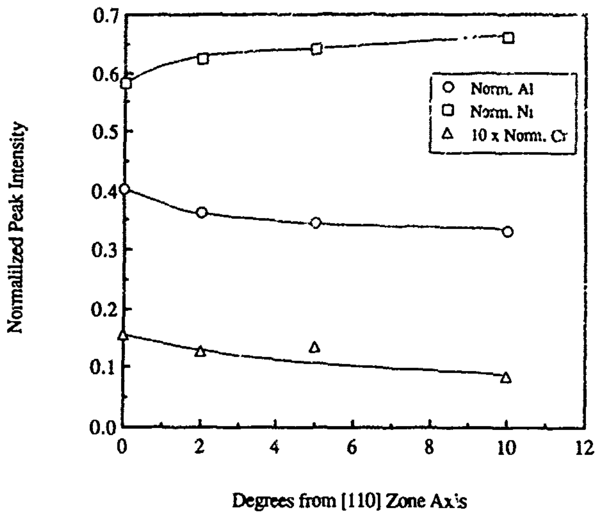

Fig. 13. ALCHEMI analysis. The intensity of the Kα X-ray peaks for Ni, Al and Cr are plotted as a function of angular deviation of the electron beam from the [110] zone axis. A preference of Cr for the Al site is demonstrated.

intensities of both the Cr and the Al X-ray peaks decrease, while that for the Ni increases, with deviation from the [110] axis, a stronger preference of Cr for the Al site than for the Ni sites is demonstrated.

Mechanical properties

Cast and homogenized alloys

The room temperature compression test results are given in Table 3 and the 0·2% CYS is plotted in Fig. 14 as a function of composition. Rather large standard deviations in the mean property values were observed, presumably as a result of the large grain size (relative to specimen size) and casting heterogeneities.

Table 3. Compression test data of cast and homogenized NiAl + Cr alloys at 300 K

Alloy	0.2% CYS (MPa)	UCS (MPa)	Plastic strain (%)	Number of tests
Ni–48Al	462 ± 25	527 ± 34	0·4 ± 0·3	8
Ni–50Al	148 ± 29	468 ± 171	12 ± 10	8
Ni–52Al	834 ± 186	867 ± 238	0·35 ± 0·2	7
Ni–47Al–1 Cr	543 ± 72	606 ± 64	0·73 ± 0·4	8
Ni–49Al–1 Cr	450 ± 56	534 ± 68	0·5 ± 0·2	9
Ni–49·5Al–1 Cr	403 ± 100	457 ± 70	0·9 ± 0·8	9
Ni–50Al–1 Cr	461 ± 97	514 ± 92	0·5 ± 0·4	8
Ni–52Al–1 Cr	no data	246	no data	2
Ni–48Al–2 Cr	461 ± 49	500 ± 49	0·5 ± 0·2	8
Ni–49Al–2 Cr	440 ± 42	560 ± 49	0·7 ± 0·3	9
Ni–50Al–2 Cr	571 ± 81	599 ± 69	1·0 ± 0·8	8
Ni–45Al–5 Cr	753 ± 69	870 ± 63	0·6 ± 0·1	8
Ni–47·5Al–5 Cr	453 ± 68	608 ± 9	1·3 ± 1·5	7
Ni–50Al–5 Cr	816 ± 151	885 ± 94	0·2 ± 0·3	7

Error = standard deviation.

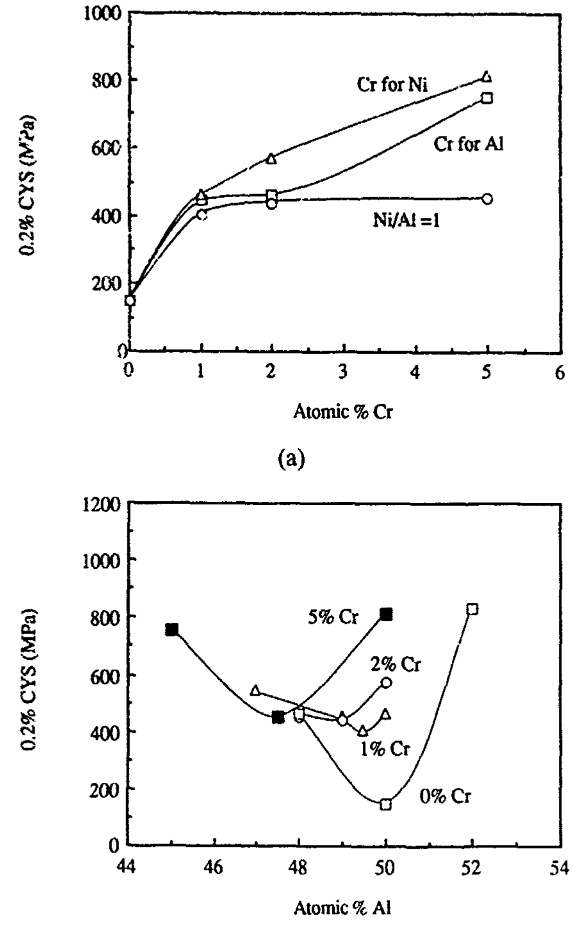

Fig. 14. The 0·2% CYS of the cast and homogenized alloys as a function of (a) Cr content and (b) Al content.

The measurement of microhardness was used as an alternative route to estimating strength variations as a function of composition, and 21 additional ternary NiAl–Cr alloys, in addition to the original 15, were produced by casting in like manner for the sole purpose of hardness measurement

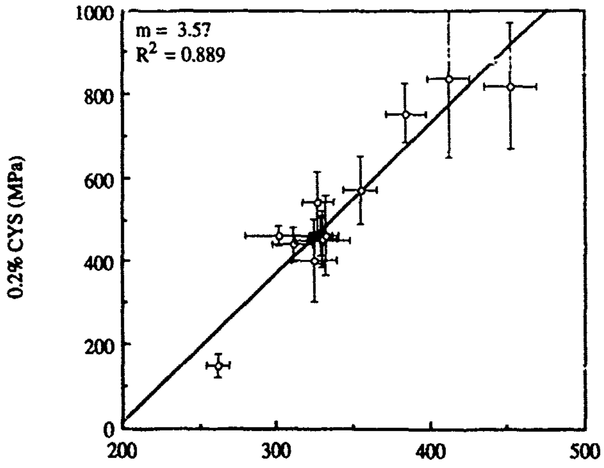

Fig. 15. Linear relationship between microhardness and 0·2% CYS for cast and homogenized NiAl and NiAl–Cr alloys.

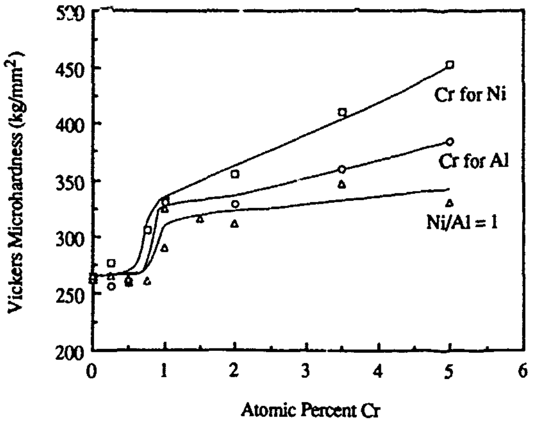

Fig. 16. Vickers microhardness of cast and homogenized NiAl-Cr alloys as a function of Cr content and alloying strategy.

to better describe this dependence. Despite the complex stress states induced by a hardness test, a linear correlation was obtained with the room temperature 0·2% yield strength values (Fig. 15). The dependence of hardness upon composition for the ternary alloys is plotted in both two-dimensional and three-dimensional coordinate systems in Figs. 16 and 17, respectively.

Both the compressive yield strength and hardness show a strong dependence upon composition, with the most pronounced dependence on Al level (or Ni/Al ratio). Alloys for which the Ni/Al ratio is unity invariably correspond to a hardness or strength minimum, regardless of Cr content. However, in all three alloy series, a three-fold increase in strength over binary Ni–50Al occurred with the addition of 1% Cr, which was independent of α-Cr precipitation. Beyond about 1% Cr, the smallest degree of hardening occurs when Cr is substituted equally for both Ni and Al, whereas the greatest hardening occurs when Cr is substituted for Ni.

Cast and extruded alloys

The 0·2% CYS data for the extruded alloys are given in Table 4. Values for strain-to-fracture and UCS were not recorded, since compressive strains in excess of 10% were readily accomplished without catastrophic failure in all alloys. Plotting the 0·2% CYS of the cast and homogenized alloys versus the extruded alloys, for identical alloy compositions, Fig. 18, shows that the compositional dependence of the 0·2% CYS is similar to the cast and homogenized alloys, although the extruded material is consistently about 17% stronger. Much less scatter in the data was also noted for the cast and extruded materials.

The 0·2% TYS and ductility as a function of test temperature are plotted for each extruded alloy in Fig. 19. Comparison of the data shows that the presence of Cr causes an approximately three-fold increase in yield strength, as observed for the cast

Table 4. Compressive yield strengths of extruded NiAl + Cr alloys at 300 K

Alloy	0.2% CYS (MPa)	Number of tests
Ni–50Al	189 ± 6	5
Ni–49·5Al–1 Cr	441 ± 16	4
Ni–48Al–2 Cr	530 ± 7	4
Ni–49Al–2 Cr	559 ± 13	4
Ni–45Al–5 Cr	818 ± 9	7

Error = standard deviation.

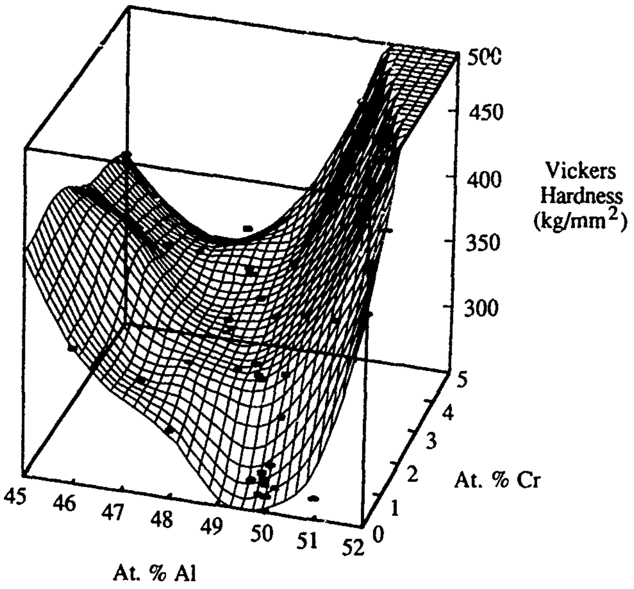

Fig. 17. Three-dimensional surface describing microhardness as a function of ternary composition in cast and homogenized NiAl + Cr alloys.

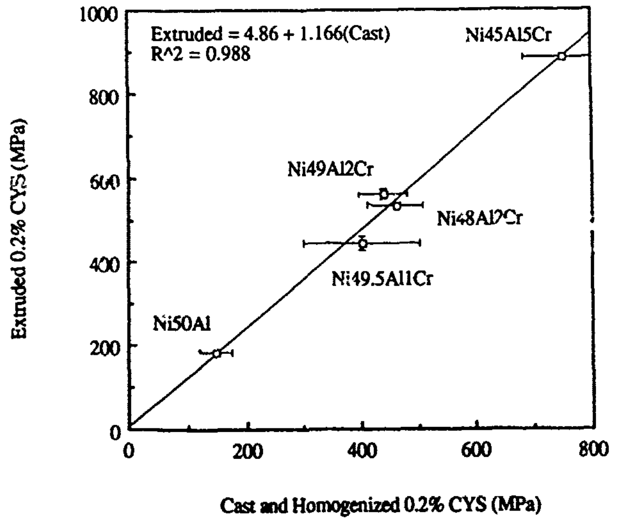

Fig. 18. Linear relationship between 0·2% CYS of NiAl–Cr cast and homogenized and cast and extruded alloys.

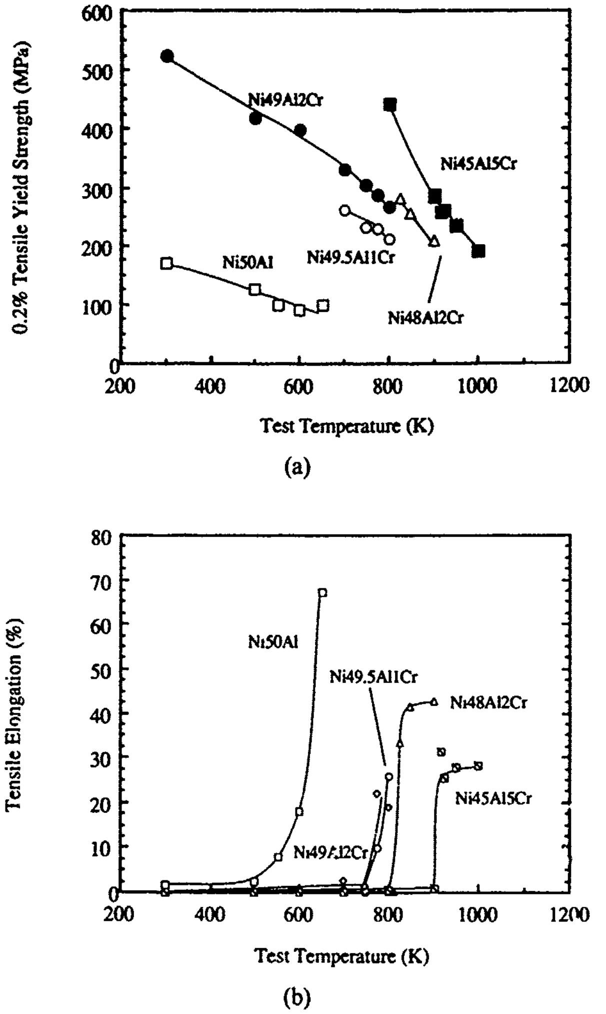

(a)

(b)

Fig. 19. Tensile properties of cast and extruded NiAl–Cr alloys as a function of test temperature: (a) 0·2% TYS; (b) percent tensile elongation.

alloys. Less than 0·2% elongation was obtained for the ternary alloys below about 700 K (except for the Ni–49Al–2Cr alloy) and thus, yield strength values were not determined. Alloys for which the Ni/Al ratio is not unity (Ni–48Al–2Cr and Ni–45Al–5Cr) displayed a greater temperature dependence of strength than those for which it is equal to unity. A similar relationship is manifest in the ductility, Fig. 19(b). Binary, stoichiometric Ni–50Al had a BDTT of about 550 K. The addition of Cr to alloys for which the Ni and Al contents are equal, such as Ni–49·5Al–1Cr or Ni–49Al–2Cr, raises the BDTT 150 K, independently of Cr level. In contrast, Ni–48Al–2Cr and Ni–45Al–5Cr display higher BDTTs, not necessarily as a result of higher Cr levels, but due to lower Al content, i.e. deviation of the Ni/Al ratio from unity. This dependence of the BDTT upon the compound stoichiometry is shown by the plot in Fig. 20. The room temperature tensile fracture surfaces were predominantly transgranular for the ternary alloys and intergranular for the binary Ni–50Al alloy.

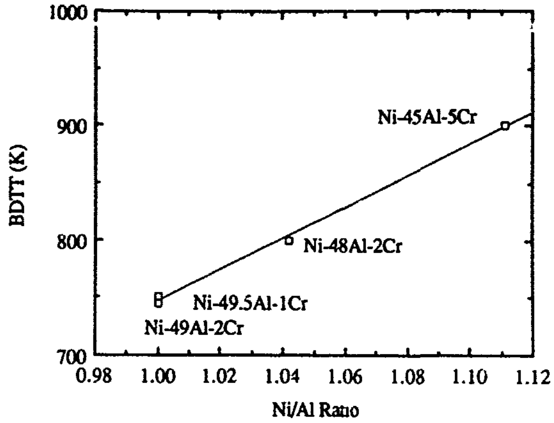

Fig. 20. Variation of BDTT with Ni/Al ratio of extruded NiAl–Cr alloys.

DISCUSSION

Microstructural evolution

A pseudobinary eutectic system occurs between the B2 β-NiAl and BCC α-Cr phases, Fig. 21.[30,49] Although Cr solubility decreases with increasing Al content, this diagram is useful to describe microstructual evolution in this regime. The retrograde shape of the β-NiAl solvus trace indicates that alloys containing more than about 1–2% Cr should consist of α-Cr precipitates in a β-NiAl matrix. However, in practice, nonequilibrium solidification is expected to produce some degree of coring and interdendritic Cr-rich liquid (eutectic).

Homogenization at 1673 K should produce a

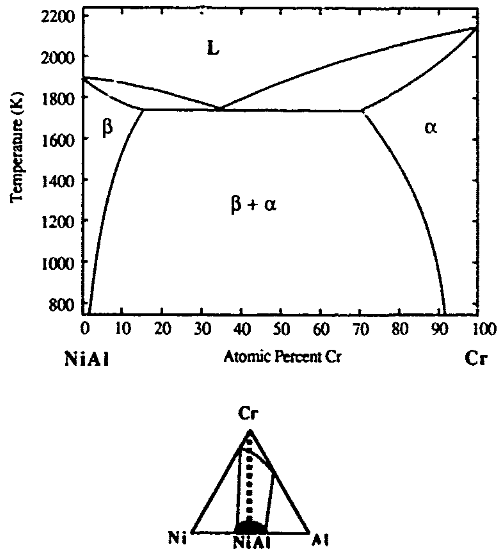

Fig. 21. Pseudobinary eutectic phase diagram for β-NiAl and α-Cr. After Ref. 30.

single phase β structure at this temperature for all the compositions in this study. This should also be true for the extrusions, which, although thermally equilibrated at 1400 K prior to extrusion, remained within the single phase regime during processing. The alloys with higher Cr content are expected to contain a larger precipitate size distribution, since precipitation occurs over a wider temperature range, consistent with the microstructures in Figs 3 and 12. Alloys with less solute, such as Ni–49Al–2Cr, would not encounter the $\beta/(\beta + \alpha)$ solvus until relatively low temperature, e.g. 800 K, and the precipitate size and size distribution are expected to be small (Fig. 11). In all alloys, grain boundaries, operating as heterogeneous nucleation sites, produced larger precipitates which were surrounded by precipitate-free zones.

The cube-on-cube orientation relationship displayed between the NiAl matrix and α-Cr precipitates is not unexpected given the similarity in structure and lattice parameters (a_{NiAl} = 0·28864 nm and a_{Cr} = 0·2884 nm).[50] Cline *et al.*[51] demonstrated this orientation relationship previously in Ni–33Al–33Cr (quasibinary eutectic composition) alloys. However, the pronounced alignment of the α-Cr precipitates shown in Figs 3(b), 3(d) and 8 deserves comment. Precipitate alignment was most pronounced in castings with Al contents near 50%, yet was essentially nonexistent in the extrusions. Since the precipitates in the extrusions did not exhibit alignment, it is likely that, in the castings, interdentritic Cr was not completely dissolved during homogenization; or assuming complete dissolution, insufficient time was allowed for complete solute redistribution. Incomplete dissolution would cause local Cr-rich regions to remain which, during slow cooling, may spheroidize into discrete aligned precipitates. The extended time in the single phase field experienced by the extrusions, combined with the mechanical work of extrusion, probably assisted in more completely distributing the Cr throughout the matrix. Alternatively, precipitate alignment could have result from the elastic interactions associated with the coherency strains, as observed in Ni_3Al precipitates in certain superalloys.[52] While precipitate alignment was not observed in the extruded alloys, perhaps the slower cooling rate of the casting following the homogenization anneal, relative to the fast air cool of the extrusions, encouraged precipitate coarsening and alignment.

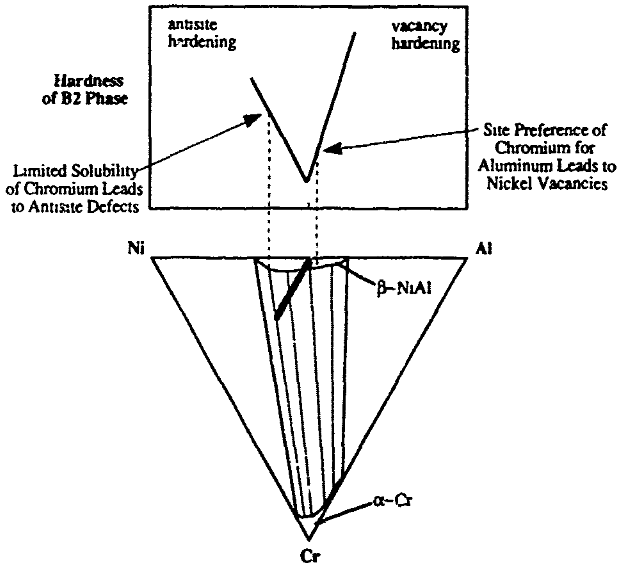
antisite hardening
vacancy hardening
Hardness of B2 Phase
Limited Solubility of Chromium Leads to Antisite Defects
Site Preference of Chromium for Aluminum Leads to Nickel Vacancies
Ni
Al
β-NiAl
α-Cr
Cr

Fig. 22. Indirect effects of Cr additions on hardening mechanisms due to limited solubility and site preference. This example is for the case of Cr substituted solely for Al in the overall alloy composition.

Composition–structure–property relationships

The mechanical behavior of these alloys is considered below in terms of solid solution, precipitate, grain size and texture effects on strength. It will be shown that solid solution strengthening appears to be the most influential of these various effects.

The alloys in this study contained Cr as a ternary addition which was usually added in one of three systematic ways: substitution solely for Al; substitution solely for Ni; and equal substitution for both Ni and Al (Ni/Al = 1), Fig. 2. In this manner, it was hoped that the effect of site occupation might be understood. For example, is Cr a more potent strengthener on the Ni site than on the Al site? Furthermore, there appear to be other important solid solution effects, besides the direct contribution of Cr solute, which affect mechanical properties. The limited solubility of Cr in NiAl must be considered here, since the addition of Cr beyond the solubility limit for either Ni and Al shifts the composition of the B2 phase away from exact 50/50 stoichiometry. This has the effect of inducing intrinsic point defect hardening by antisite or vacancy defects, as observed in off-stochiometric binary NiAl alloys.[10,11,16] The schematic diagram in Fig. 22 illustrates an example of this effect for an alloy such as Ni–45Al–5Cr. In this figure, Cr is substituted completely for Al in the overall alloy composition. Its limited solubility causes the B2 composition to lie on increasingly Ni-rich tie-lines in the two-phase region of the ternary isotherm as Cr is added. This leads to a B2 phase which is hardened by both Cr and Ni atoms on Al sites.

Another potentially important and related parameter affecting mechanical properties is the site preference of Cr. The ALCHEMI results, as well as previous research,[25] indicate that Cr prefers the Al site in NiAl when substituted evenly (i.e. keeping %Ni/%Al = 1). Even substitution is necessary to clearly establish site preference, since this gives an equal chance for the solute to choose either site. This behavior should cause Cr to behave like an Al atom, effectively creating a surplus of Al sites in the structure unless %Cr + %Al ≤ %Ni. Since Al atoms do not reside on Ni sites in NiAl,[8,10,11] it is likely that the presence of Cr in an alloy such as Ni–49·5Al–1Cr increases the vacancy concentration on the Ni sublattice and produces the high hardening rate usually associated with this type of point defect.[11,16] However, such an effect was not obvious in the experimental data shown in Table 3 and Figs 14 and 16. For example, the 0·2% CYS values for Ni–49Al–1Cr and Ni–49·5Al–1Cr are 450 ± 56 and 403 ± 100, respectively, which are not significantly different (to 95% confidence). In this case, if Cr actually occupied the Al site at the expense of creating in vacancies, then a hardening increment similar to that observed in a Ni–50·5Al binary alloy is expected. However, such a small deviation (0·5%) from exact stoichiometry has not been conclusively shown to cause an increase in yield strength[13,16–18,53] and is difficult to verify chemically; thus, it cannot be expected to yield a difference here.

In light of the above discussion, the hardening observed in alloys containing more than about 1% Cr is mostly due to constitutional antisite or vacancy defects. This must be true, since the increases in strength with percent Cr beyond the solubility limit is relatively flat when Ni/Al = 1. Furthermore, the precipitate distributions are similar for all three alloy series, so precipitation strengthening cannot account for the differences.

Although not an initial part of the study, the effect of tramp interstitial elements (C, N, O) cannot be ignored when considering mechanical properties in NiAl-based alloys. Both B and C have been shown to be very potent hardeners in NiAl.[54] Since C is a common impurity in Ni shot, the source of Ni in these alloys, it is of the most concern. The flat hardening response at low Cr levels, up to about 0·75% Cr, shown by the hardness curves in Fig. 16 suggests that Cr is being removed from solution, perhaps by a gettering reaction with C. A number of $Cr_{23}C_6$ carbides were observed in all sample types in this study, supporting this view. Field *et al.*[25] also noted the presence of Cr carbides, although of the Cr_7C_3 structure, in their single crystal work on NiAl–Cr alloys. Because of the stoichiometry of the observed carbide, only approximately 500 wppm C would be required to react with 0·75 at.% Cr, which is easily within an order of magnitude of the measured values for the extrusions given in Table 2.

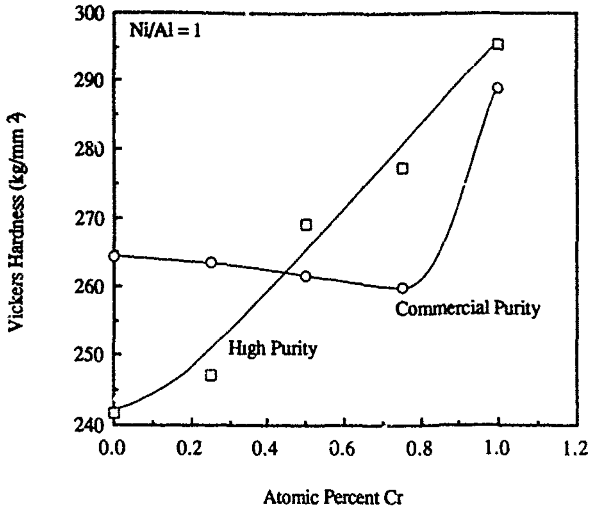

Fig. 23. Hardening response of NiAl–Cr alloys as a function of Cr level comparing alloys produced from purified Ni shot and commercial purity Ni shot. In all alloys the Ni/Al ratio was kept at unity.

To further investigate this effect, a small amount of melt-refined Ni shot was obtained and used to produce a series of arc-cast button melts containing up to 1% Cr, substituted evenly in NiAl (Ni/Al = 1). The hardness of these alloys was measured and compared to 'commercial-purity' NiAl–Cr alloys of the same nominal composition. These results are plotted in Fig. 23 and suggest that impurities in the Ni stock are removing Cr from the matrix. Statistical testing by a Student's *t*-test determined the hardness means between the two 0% Cr and 0·25% Cr alloys were significantly different to 95% confidence.

Notwithstanding the above analysis, the flat hardening response at low Cr levels could also be a result of an unknown influence of Cr on constitutional defect hardening mechanisms. For example, point defect concentrations may be reduced, or perhaps aggregated into fewer, larger defects. Softening (or at least a lack of significant hardening) has been observed in 'soft' orientation NiAl single crystals containing 0·05 and 0·2 at.% Cr[25] as well as other ternary elements[1] although similar effects have not been reported for polycrystals. The mechanism for microalloy-induced softening remains unknown.

There are several sources of solid solution strengtnening in NiAl–Cr alloys due to point defects. These include:

1. Constitutional (Ni_{Al} and V_{Ni}).
2. Substitutional (Cr_{Ni} or Cr_{Al}).
3. Interstitial (C, O, etc.).

All of these types of defects are important in determining the degree of solution hardening. The slopes of the curves in Fig. 14(a) between zero and 1% Cr show that substitutional Cr is an effective strengthing element in NiAl at room temperature, with a hardening rate of typically 300 MPa/% Cr. If one assumes that, within this interval, three-quarters of the Cr forms carbides, as suggested by the hardness data in Fig. 16, then the true hardening rate is approximately 1200 MPa/% Cr. This compares with 157 and 343 MPa/% Cr for Ni_{Al} and V_{Ni} defects, respectively, in the binary, off-stoichiometric alloys. Therefore, while Cr is a potent strengthening element in NiAl, its low solubility limits the net hardening increment due to Cr_{Ni} and Cr_{Al} to less than that possible by Ni_{Al} and V_{Ni} defect strengthening. This, combined with the fact that minima in strength and hardness occur when Ni/Al = 1 (or possibly Ni/(Al + Cr) = 1), demonstrates that constitutional defects are more important in determining the mechanical properties than substitutional defects when the solubility for the substitutional element is low.

As already mentioned, α-Cr precipitates were observed in alloys containing more than about 1% Cr. Most of the precipitates were fine, less than about 1 μm in diameter, and either coherent or semicoherent. No sheared particles were observed in the deformed specimens during TEM observation, although a number were surrounded by dislocation loops, usually when lying within a slip band. These were assumed to be Orowan loops, which is further evidence that the precipitates were not sheared, although it does not rule out loop collapse into the precipitate. This observation is contrary to the behavior of most precipitation-hardened metals, in which coherent particles are usually sheared and not by-passed by loop formation.[55] The effective particle strength may be augmented by the cube-on-cube orientation relationship which encourages a change in slip vector from ⟨100⟩ to ⟨111⟩ at the precipitate–matrix interface. Coherency strains, interfacial dislocations and the high Peierls stress of Cr itself also increase the effective particle strength.

Such a structure is amenable to treatment by classical precipitation-hardening theory[55] from which an estimate of the contribution of the precipitates to the overall alloy strength may be derived. For simplicity, pure edge dislocations and a homogeneous distribution of spherical particles are assumed. The increase in shear strength of the alloy due to precipitation is given by

$$\Delta\tau = \frac{\mu \mathbf{b}}{2\pi(\lambda - d)} \ln\left(\frac{d}{\mathbf{b}}\right)$$

where **b** is the Burgers vector, μ is the shear modulus of the matrix, d is the particle diameter and λ is the interparticle distance. By assuming a random array of particles and applying basic stereological principles, λ may be approximated by $2d/3f_p$, where f_p is the volume fraction of particles in the microstructure. In turn, f_p may be determined directly from the pseudobinary NiAl–Cr phase diagram (Fig. 21) based on the concentration of Cr in the alloy, c, according to the lever rule. That is,

$$f_p = (c - 0{\cdot}015)/(0{\cdot}95 - 0{\cdot}015)$$

Thus, the increase in yield strength, $\Delta\sigma_p$, due to precipitation of α-Cr in NiAl + Cr alloys may be estimated by

$$\Delta\sigma_p = \frac{\mu \mathbf{b}}{\pi d\left(\dfrac{0{\cdot}623}{c - 0{\cdot}015} - 1\right)} \ln\left(\frac{d}{\mathbf{b}}\right)$$

Substitution of appropriate values of μ (72 GPa)[56] and **b** (0·2886 nm)[50] indicates that an alloys which contains 5% Cr and α-Cr precipitates of about 10 nm diameter will experience an increase of about 132 MPA in yield strength due to precipitate–dislocation interactions. Since a considerable volume fraction of the precipitation occurs as larger particles, this value is an upper bound. By comparison, a homogeneous distribution of 250 nm diameter particles would produce a strength increment of only 10 MPa.

The experimentally observed increase in strength due to precipitation alone is estimated by comparing the 0·2% CYS of Ni–49·5Al–1Cr (single phase) and Ni–47·5Al–5Cr (with precipitates). In these alloys, the amount of Cr in solid solution is approximately equal, and the strengthening from constitutional point defects is similar since Ni/Al ~ 1 for both compositions. Therefore, any difference in strength should be due primarily to α-Cr precipitation in Ni–47·5Al–5Cr. The experimental difference in 0·2% CYS between these two alloys is about 50 MPa, within a factor of three of the upper-bound estimate calculated above.

This calculation suggests that precipitation hard-

Table 5. Hall–Petch constants of binary NiAl alloys[57]

Ni/Al ratio	Composition (at.%)	σ_0 (MPa)	k (MPa/μm$^{1/2}$)
1·000	Ni–50 Al	120	155
1·041	Ni–49 Al	195	654
1·083	Ni–48 Al	450	1 231
1·222	Ni–45 Al	548	1 565

ening only contributes a relatively small amount to the yield strength in these alloys. It also explains why the CYS curve in Fig. 14 for the Ni/Al = 1 alloys has a small slope ($d\sigma/dc$) beyond about 1% Cr. Although the precipitates are an effective size for precipitation hardening, their volume fraction is too small to increase the strength of the alloy significantly.

As indicated by Fig. 18, processing by extrusion causes a linear strength increase of about 17% over casting and homogenization. Aside from texture effects (discussed below), the principal microstructural difference between the cast and homogenized material and the extrusions is the grain size, roughly 20 and 5000 μm, respectively. Recent work[2,57] has shown that the yield strength dependence of NiAl on grain size increases with deviation from stoichiometry. Based on the general form, $\sigma_y = \sigma_0 + kd^{-1/2}$, where σ_o is the lattice resistance, k is the Hall–Petch slope and d is the grain size in micrometers, the Hall–Petch constants for binary NiAl are given in Table 5.[57]

Applying the appropriate equation to the Ni–50Al alloys in the current study, a strength differential between extruded and cast alloys of about 33 MPa is predicted, which is reasonably close to the experimental values for Ni–50Al (34 MPa) and Ni–49·5Al–1Cr (38 MPa). However, the other alloys, particularly Ni–48Al–2Cr and Ni–45Al–5Cr, should behave similarly to off-stoichiometric binary alloys since they lie on a different tie-line, and therefore display a much larger Hall–Petch effect. For example, Ni–48Al–2Cr contains, presumably, about 1% Cr in solution residing on the Al sites. Consequently, the β-phase consists of about 49% Al (and Cr_{Al}) sites and 51% Ni sites. Application of the Hall–Petch equation for Ni–49Al leads to a predicted strength differential due to grain size of 137 MPa, whereas the measured differential was 69 MPa. Similar analysis of Ni–45Al–5Cr predicts a differential of 258 MPa, in contrast to the measured difference of 131 MPa. These departures from the predicted behavior for off-stoichiometric ternary alloys (Ni/Al $\neq$ 1) are perhaps explained by noting that grain refinement strengthening is only effective when the mean free path of dislocation travel exceeds the grain size. In the alloys containing precipitates, dislocation motion is hindered by their presence. This is especially important for the cast and homogenized alloys, which displayed a coarser grain size.

Another possible explanation of the difference in strength between the cast and homogenized materials and the extrusions is a greater thermal point defect concentration in the extrusions. Since the extrusions were air-cooled at a relatively fast rate, while the casting were furnace cooled, the extrusions are expected to contain a greater point defect concentration. Similar behavior was observed by Bowman *et al.*[14] for binary Ni–50Al in which specimens cooled at 1·33 K s^{-1} exhibited a yield strength of 325 MPa, while those cooled at 0·025 K s^{-1} exhibited a yield strength of 260 MPa, a difference of 65 MPa.

The elevated temperature yield strengths of the extruded alloys, Fig. 19(a), decreased with increasing test temperature, and a slightly greater slope, $d\sigma/dT$, was noted for higher Cr levels. This may be explained on grounds similar to those discussed above for the room temperature properties. That is, solid solution strengthening by Cr, Ni or vacancies is primarily responsible for the strength variation with composition (aside from interstitial impurities). Furthermore, the slopes correlate with the Ni/Al ratio. For example, the curves for Ni–49Al–2Cr and Ni–49·5Al–Cr are approximately parallel and both of their Ni/Al ratios are unity. The Ni–48Al–2Cr and Ni–45Al–5Cr $d\sigma/dT$ slopes scale with deviation of their Ni/Al ratios from unity. Since the elevated temperature properties are at least partially controlled by diffusion-assisted processes, this correspondence is logical, as off-stoichiometric binary NiAl alloys are known to display enhanced diffusivity relative to the stoichiometric compound.[58]

The elongations as a function of test temperature, Fig. 19(b), indicate that Cr in solid solution elevates the DBTT about 150 K relative to binary NiAl. As for the yield strength, comparison of the curves for Ni–49Al–2Cr and Ni–49·5Al–1Cr indicates that the Ni/Al ratio is again the primary factor controlling the BDTT. These alloys exhibit the lowest BDTT of the ternary alloys, while increasing deviation of NiAl from unity elevates the BDTT for the other ternary alloys. This is analogous to the effects of stoichiometry on the BDTT for binary NiAl alloys.[59]

The cause of the BDTT in NiAl is not fully understood. However, recent evidence[14,15] points to at least a partial dependence on thermal activation of an alternate deformation mechanism at the BDTT. The 150 K elevation of the BDTT in the ternary alloys of this study may be a result of solute drag by Cr in solid solution, delaying activation to higher temperatures. Furthermore, since the yield strength is more dependent on temperature than fracture strength, increases in the flow stress due to alloying will lower the amount of allowable strain below the BDTT.

SUMMARY

The effects of Cr additions on the microstructure and mechanical properties of NiAl-base alloys have been characterized over a range of compositions (0 to 5% Cr and 45 to 52% Al) and different processing methods. Chromium has a limited solubility in NiAl at lower temperatures, typically about 1 at.%. The solubility also depends on the Ni/Al ratio, is slightly greater in alloys containing less than 50% Al, and is related to the site preference of Cr for Al in NiAl. Higher alloying levels of Cr produce coherent or semicoherent α-Cr precipitation upon slow cooling from homogenization temperatures; these are typically quite fine. The mechanical property data show Cr is an effective solid solution strengthener in NiAl, essentially tripling the 0·2% yield strength at temperatures below the BDTT. The stoichiometry (Ni/Al ratio) also plays a major role in determining mechanical properties, analogous to binary NiAl alloys, such that minor deviation of the Ni/Al ratio from unity causes significant increases in yield strength over and above Cr effects. In addition, deviation from stoichiometry causes reduced ductility at lower temperatures, and a greater temperature dependence of strength at intermediate temperatures. This behavior has implications with respect to ternary compositions in the $\alpha + \beta$ field, because the resulting Ni/Al ratio of the B2 phase (NiAl) may deviate significantly from unity, depending on the exact tie-line it terminates. Finally, there is a strong indication that interstitial elements (particularly C) play an important role in mechanical properties, both due to their specific strengthening contribution and as a result of gettering reactions with Cr.

Acknowledgments

J.D.C. and M.J.K. express their appreciation for the financial and technical support of the NASA–Lewis Research Center under grant number NAG 3-1079. The guidance of M. V. Nathal and the suggestions of S. V. Raj are sincerely acknowledged. Special thanks are also due to Dr L. S. Chumley for providing the high purity Ni shot and to M. K. Behbehani for his assistance in mechanical testing.

REFERENCES

1. Darolia, R., *JOM*, **3** (1991) 44.
2. Noebe, R. D., Bowman, R. R. & Nathal, M. V., *Int. Mater. Rev*, in press.
3. Darolia, R., *et al.*, in *Ordered Intermetallics—Physical Metallurgy and Mechanical Behavior*, ed. C. T. Liu *et al.* Kluwer Academic Publishers, the Netherlands, 1992, p 679.
4. Fox, A. G. & Tabbernor, M. A., *Acta Metall*, **39** (1991) 669.
5. Cooper, M. J. *Phil Mag.*, **8** (1963) 811.
6. Cotton, J. D., Noebe, R. D. & Kaufman, M. J., *Intermetallics*, **1** (2) (in press).
7. Massalski, T. B., ed., *Binary Alloy Phase Diagrams*, Vol. 1. American Society for Metals, Metals Park, Ohio, 1986, p. 140.
8. Lipson, H. & Taylor, A., *Proc. Roy Soc.*, **173** (1939) 232.
9. Hume-Rothery, W., *The Structure of Metals and Alloys*. Chemical Publishing Co., New York, 1939, p. 103.
10. Bradley, A. J. & Taylor, A., *Proc. Roy. Soc. A*, **159** (1937) 56.
11. Westbrook, J. H., *J. Electrochem. Soc.*, **103** (1956) 54.
12. Noebe, R. D., Bowman, R R., Cullers, C. L., & Raj, S. V., in *High-Temperature Ordered Intermetallic Alloys IV MRS Symp Proc.*, **213** (1991) 589
13. Rozner, A. G. & Wasilewski, R. J., *J. Inst Metals*, **94** (1966) 169.
14. Bowman, R. R., Noebe, R. D., Raj, S. V & Locci, I. E., *Metall. Trans. A.*, **23A** (1992) 1493.
15. Noebe, R. D., Cullers, C. L. & Bowman, R. R., *J. Mater. Res.*, **7** (1992) 605.
16. Pascoe, R. T. & Newey, C. W A., *Metal Sci. J.*, **2** (1968) 138.
17. Ball, A. & Smallman, R. E, *Acta Metall.*, **14** (1966) 1349.
18. Hahn, K. H. & Vedula, K., *Scripta Metall. Mater.*, **23** (1989) 7.
19. Whittenberger, J. D., Arzt, E & Luton, M. J., *J. Mater. Res*, **5** (1990) 271.
20. Whittenberger, J. D., Viswanadham, R. K., Mannan, S. K. & Sprissler, B., *J. Mat. Sci.*, **25** (1990) 35.
21. Whittenberger, J. D., Arzt, E. & Luton, M J., in *Intermetallic Matrix Composites MRS Symp. Proc*, **194** (1990) 211.
22. Noebe, R. D, Bowman, R. R. & Eldridge, J. I., in *Intermetallic Matrix Composites II* (1992) 323.
23. Whittenberger, J. D., Reviere, R., Noebe, R. D. & Oliver, B. F., *Scripta Metall. Mater.*, **26** (1992) 987.
24. Takeyama, M. & Liu, C. T., *J. Mater. Res.*, **5** (1990) 1189.
25. Field, R. D., Lahrman, D. F. & Darolia, R., *Acta Metall.*, **39** (1991) 2961.
26. Pank, D. R., Nathal, M. V. & Koss, D. A., *J. Mater. Res.*, **5** (1990) 942.
27. Noebe, R. D., Ritzert, F. J., Misra, A. & Gibala, R., NASA TM-103796, NASA—Lewis Research Center, Cleveland, Ohio, 1991.
28. Ishida, K., Kainuma, R., Ueno, N. & Nishizawa, T., *Metall. Trans. A*, **22A** (1991) 441.

29. Larsen, M., Misra, A., Hartfield-Wunsch, S., Noebe, R. & Gibala, R., in *Intermetallic Matrix Composites, MRS Symp. Proc.*, **194** (1990) 191.
30. Merchant, S. M. & Notis, M. R., *Mater. Sci. Eng.*, **66** (1984) 47.
31. Pellegrini, P. W. & Hutta, J. J., *J. Crys. Growth*, **42** (1977) 536.
32. Cotton, J. D., Kaufman, M. J. & Noebe, R. D., *Scripta Metall. Mater.*, **25** (1991) 1827.
33. Maslenkov, S. B., Udovskii, A. L., Burova, N. N. & Rodimkina, V. A., *Russian Metallurgy (Metally)*, **1** (1986) 198.
34. Nash, P., Fielding, S. & West, D. R. F., *Metal Sci.*, **17** (1983) 192.
35. Webber, J. G. & Van Aken, D. C., *Scripta Metall.*, **23** (1989) 193.
36. Subramanian, P. R., Mendiratta, M. G., Miracle, D. B. & Dimiduk, D. M., in *Intermetallic Matrix Composites. MRS Symp. Proc.*, **194** (1990) 147.
37. Von Mises, R., *Z. Angew Math. Mech.*, **8** (1928) 161.
38. Groves, G. W. & Kelly, A., *Phil. Mag.*, **81** (1963) 877.
39. Law, C. C. & Blackburn, M. J., Report No. ED/GPD FR-18674-4, United Technologies Corp., Pratt and Whitney Group, 1985.
40. Dimiduk, D. M. & Rao, S, in *High-Temperature Ordered Intermetallic Alloys IV. MRS Symp. Proc.*, **213** (1991) 499.
41. Miracle, D. B., Russell, S. & Law, C. C., in *High-Temperature Ordered Intermetallic Alloys III. MRS Symp. Proc.*, **133** (1989) 225.
42. Loretto, M. H. & Wasilewski, R. J., in *The Strength of Metals and Alloys. American Society for Metals Conf. Proc.* 1970, p 113.
43. Loretto, M. H. & Wasilewski, R J., *Phil. Mag.*, **23** (1971) 1311.
44. Campany, R. G., Loretto, M. H. & Smallman, R. E., *J. Microscopy*, **90** (1973) 174.
45. Veyssière, P. & Noebe, R. D., *Phil. Mag. A*, **65** (1992) 1.
46. Field, R. D., Lahrman, D. F. & Darolia, R., *Acta Metall. Mater.*, **39** (1991) 2951.
47. Kim, J. T. & Gibala, R., in *High-Temperature Ordered Intermetallic Alloys IV. MRS Symp. Proc.*, **213** (1991) 216.
48. Taftø, J. & Spence, J. C. H., *Science*, **218** (1982) 49.
49. Kornilov, I. I. & Mints, R. S., *J. Inorg Chem. (USSR)*, **3** (1958) 699.
50. Villars, P. & Calvert, L. D., *Pearson's Handbook of Crystallographic Data for Intermetallic Phases 2.* American Society for Metals, Metals Park, Ohio, 1985.
51. Cline, H. E., Walter, J. L., Koch, E. F. & Osika, L. M., *Acta Metall.*, **19** (1971) 405.
52. Ricks, R. A., Porter, A. J. & Ecob, R. C., *Acta Metall.*, **31** (1982) 43.
53. Raj, S. V., Noebe, R. D. & Bowman, R. R., *Scripta Metall.*, **23** (1989) 2049.
54. George, E. P. & Liu, C. T., *J. Mater. Res.*, **5** (1990) 754.
55. Gerold, V., in *Dislocations in Metallurgy*, ed. F. R. N. Nabarro. North-Holland Publishing Company, New York, 1979, p. 219.
56. Tressler, R. E., Hellmann, J. R. & Hahn, H. T., Report No. CAM-9101. The Center for Advanced Materials, 1990.
57. Baker, I., Nagpal, P., Liu, F., Munroe, P. R., *Acta Metall. Mater.*, **39** (1991) 1637.
58. Shankar, S. & Seigle, L. L., *Metall. Trans. A*, **9A** (1978) 1467.
59. Vedula, K. & Khadkikar, P. S., in *High-Temperature Aluminides and Intermetallics*, ed. S. H. Whang *et al.*, TMS, Warrendale, Pennsylvania, 1990, p. 197.

Intermetallics 1 (1993) 21–27

High-resolution electron microscopy of dislocations in $CoSi_2$ with the C1 structure

K. Suzuki & S. Takeuchi

Institute for Solid State Physics, The University of Tokyo, Roppongi, Minato-ku, Tokyo 106 Japan

(Received 5 November 1992; accepted 17 December 1992)

Weak-beam and high-resolution electron microscopy of dislocations in $CoSi_2$ with the C1 structure, introduced at room temperature by pulverization, has shown that dislocations with the $\langle 100\rangle$ Burgers vector and those with $1/2\langle 110\rangle$ are dissociated into partial dislocations by the following reactions:

$$\begin{array}{lll} \langle 100\rangle & 1/2\langle 100\rangle + 1/2\langle 100\rangle & \text{on } \{001\} \\ 1/2\langle 110\rangle & 1/4\langle 111\rangle + 1/4\langle 11\bar{1}\rangle & \text{on } \{1\bar{1}0\} \\ 1/2\langle 110\rangle & 1/6\langle 211\rangle + 1/6\langle 12\bar{1}\rangle & \text{on } \{\bar{1}11\} \end{array}$$

Stacking faults and micro-twins have also been observed by high resolution electron microscopy. Evidence that vacancies are mobile at room temperature has been obtained by observations of helical dislocations.

Key words: $CoSi_2$, high resolution electron microscopy, dislocation, dislocation dissociation, stacking fault.

1 INTRODUCTION

$CoSi_2$, having the C1 structure and melting point of 1653 K, has been used as current leads on large scale integration (LSI) devices utilizing its metallic character. The compound can also be a candidate for high-temperature materials, as can other transition metal silicides such as $MoSi_2$ and WSi_2 with the C11 structure and $CrSi_2$ and $TaSi_2$ with the C40 structure. $CoSi_2$ and $NiSi_2$ with the C1 structure have an advantage over the other silicide crystals because the C1 structure has an fcc symmetry which can provide a number of equivalent slip systems. Takeuchi *et al.*[1] have recently investigated the plasticity of polycrystalline $CoSi_2$ in a wide temperature range and showed that above 873 K, the crystal can be compressed to a strain greater than 80% without fracture. They have postulated from their results of activation analysis of plastic deformation that the ductility is due to the activity of $\{111\}\langle 110\rangle$ slip systems and that the $1/2\langle 110\rangle$ dislocations are dissociated into partial dislocations on $\{111\}$ planes as in fcc metals. It has been established that in the C1 crystals of ionic character such as CaF_2, the primary slip system is $\{001\}\langle 110\rangle$.[2] Recent slip line observations and electron microscopy of plastically deformed single crystals of $CoSi_2$ have revealed that the active slip system at room temperature is $\{001\}\langle 100\rangle$[3] and that $\{110\}\langle 110\rangle$ and $\{111\}\langle 110\rangle$ slip systems become active at high temperatures.[4] In the present paper, we have investigated dislocations in $CoSi_2$ introduced by plastic deformation with high-resolution electron microscopy.

2 EXPERIMENTAL PROCEDURES

Specimens were the same as those used in the previous deformation experiment:[1] crystals were produced by arc-melting high-purity (better than 99·99%) raw materials in an argon atmosphere.

We adopted two different methods to prepare thin foil samples for transmission electron microscopy observations. In one method, we first sliced bulk specimens compressed at high temperatures by a cutter, ground by emery paper to a thickness of 0·1 mm, made a dent by a dimple-grinder and finally thinned by ion-milling. In the other method, we pulverized an as-arc-melted crystal in a mortar at room temperature, and collected thin tiny flakes on micro-grid meshes. In the former method, dislocations introduced by high temperature compression were observed while in the latter method,

Intermetallics 0966-9795/93/$6.00 © 1993 Elsevier Science Publishers Ltd, England. Printed in Great Britain

dislocations introduced by room temperature pulverization were observed.

The electron microscope used was a Hitachi H-9000 type with a point-to-point resolution of 0·19 nm at an accelerating voltage of 300 kV. We performed lattice image observations at a defocus value of about 50 nm under a multi-beam diffraction condition with the electron beam parallel to a ⟨110⟩ axis in most cases. We also conducted weak-beam observations and determined Burgers vector of dislocations based on the $\mathbf{g} \cdot \mathbf{b} = 0$ criterion.

3 RESULTS

As shown in a previous paper,[1] a large plastic deformation of polycrystalline samples can be achieved only above 700 K, and the yield stress decreases rapidly with increasing temperature. In accordance with such a steep temperature dependence of the yield stress, the dislocation configuration in samples pulverized at room temperature was quite different from that in samples deformed at high temperatures. Dislocation pile-ups have never been observed in samples deformed at high temperatures and the activated slip systems were difficult to determine by transmission electron microscopy. On the other hand, most dislocations introduced at room temperature by pulverization were observed to be dissociated into partial dislocations. Stacking faults on {111} planes and twin bands parallel to {111} planes were also observed in samples pulverized at room temperature.

3.1 Weak-beam observations

3.1.1 Dislocations introduced at high temperatures
Figure 1(a) shows a typical dislocation structure in a sample deformed at 873 K. All the dislocations are more or less curved. No pile-ups are observed, probably because cross-slip is rather easy at high temperatures. Figure 1(b) is an example of weak-beam micrographs, showing that most of the dislocations are apparently undissociated. We observed dislocation images in the same area under three 220 two-beam diffraction conditions near a ⟨111⟩ zone axis orientation and also under three 111 two-beam diffraction conditions near three ⟨112⟩ zone axis orientations which make an angle of 19 degrees to the initial ⟨111⟩ axis. Based on the $\mathbf{g} \cdot \mathbf{b} = 0$ criterion, most of the dislocations observed were identified to have Burgers vectors of the 1/2⟨110⟩ type. However, slip planes of these dislocations could not be determined.

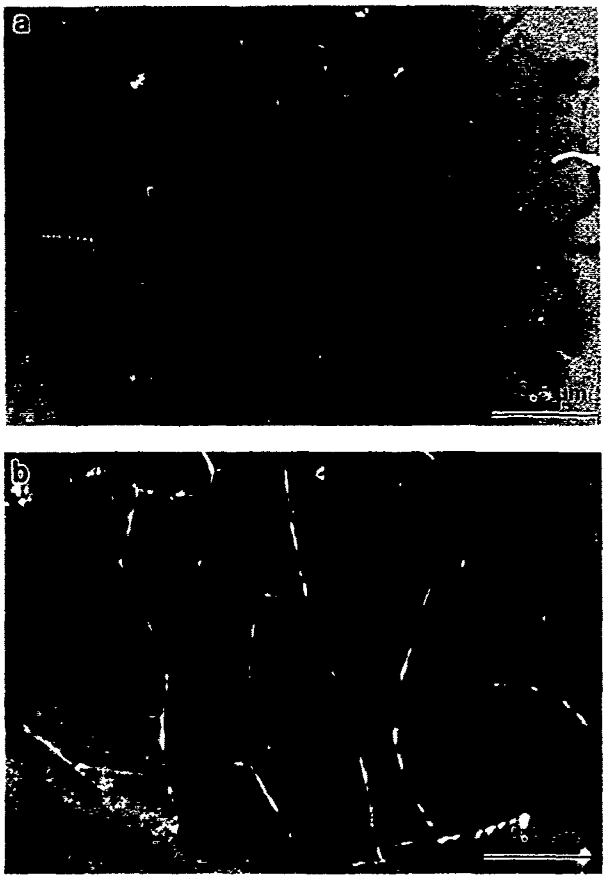

Fig. 1. (a) Typical dislocation structure in a specimen deformed at 873 K, and (b) a weak-beam micrograph of dislocations in the same specimen.

3.1.2 Dislocations introduced at room temperature
In thin samples produced by pulverization at room temperature, a high density of dislocations usually exist near the edge of thin samples; these dislocations are considered to have been introduced by high stress concentration in the cleavage process. In contrast to dislocations introduced at high temperatures, most dislocations introduced at room temperature were found to be dissociated into partial dislocations by weak-beam observations.

Figure 2 shows a series of electron micrographs of dislocations taken with five different two-beam conditions near the [111] zone axis orientation. Most dislocations are seen to be paired and such paired dislocations are almost equally visible except in Fig. 2(c) taken with $\mathbf{g} = 0\bar{2}2$, in which most paired dislocations are faint. These facts mean that paired dislocations have parallel Burgers vectors which are perpendicular to the $[0\bar{1}1]$ direction. As indicated in Fig. 2(e), taken at a higher magnification, the surface trace of a paired dislocation in a thin and flat region (the upper right of Fig. 2(e)) coincides with the trace of (010) planes: the traces of paired dislocations in a thicker part deviate from the (010) trace owing to

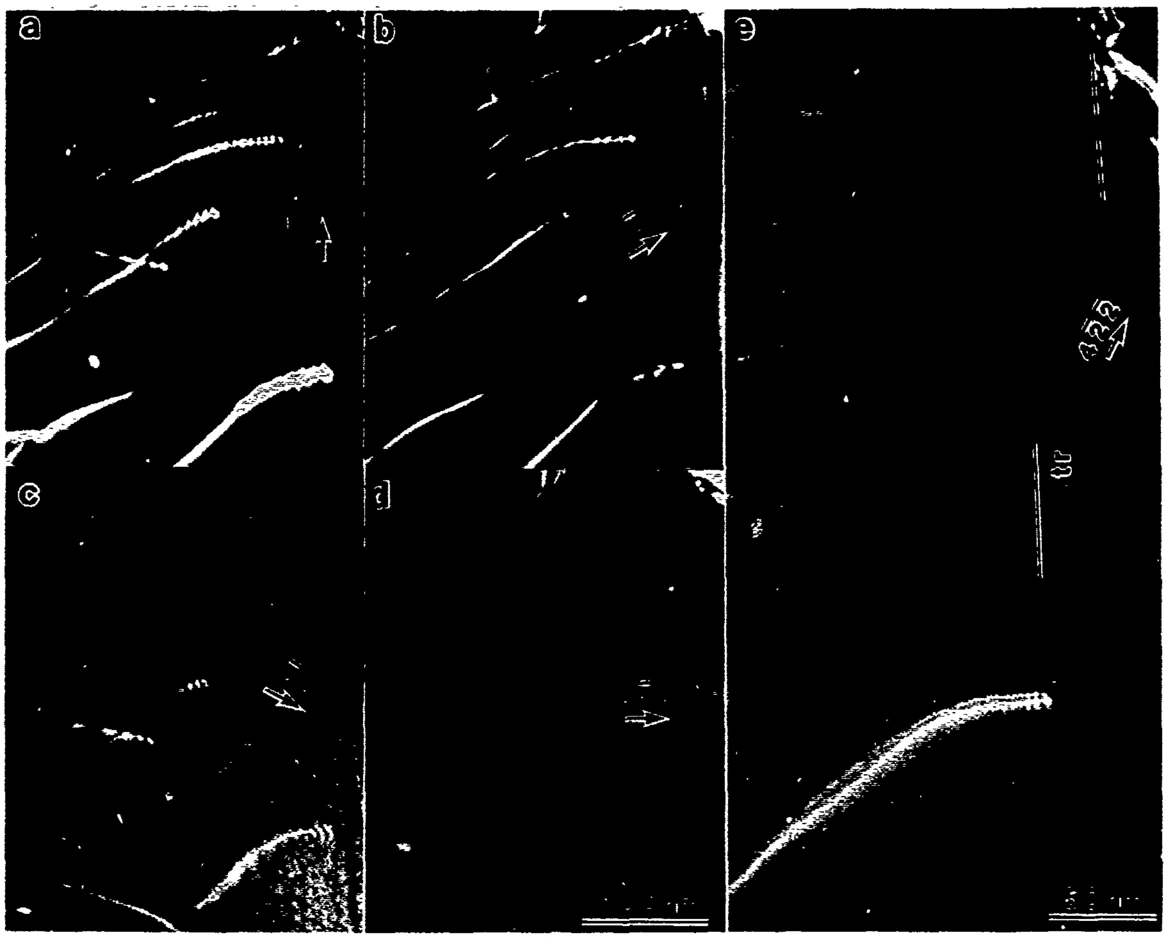

Fig. 2. Weak-beam, dark-field electron micrographs taken from [111] direction under five diffraction conditions for a pulverized sample. Arrows indicate diffraction vectors.

a considerable inclination of the specimen surface from the (111) plane as manifested by dense thickness-fringes at the thicker part. These results are reasonably explained if the dislocations have a total Burgers vector of [010] and are dissociated into two partial dislocations by the reaction

$$[010] \rightarrow 1/2[010]+1/2[010] \qquad (1)$$

but are difficult to understand by other types of dissociation. This result is in accord with the reported active slip system at room temperature, i.e. $\{100\}\langle 001\rangle$.[3]

Figures 3(a)–(d) show another series of weak-beam images of dislocations introduced at room temperature taken under different diffraction conditions near the [011] zone axis orientation. Dislocations labelled A to H are rather widely dissociated into partials and the fault fringes between them are clearly seen in Figs 3(a), (b) and (d). Partial dislocations bounding a stacking fault are labelled 1 and 2 for each dissociated dislocation in Fig. 3(b). In Fig. 3(a) taken with $\mathbf{g}_a = 11\bar{1}$, fringe contrast is clearly seen but the apparently undissociated part of the dislocations in the upper part, as well as partial dislocations, are almost invisible. In Fig. 3(b) taken with $\mathbf{g}_b = \bar{2}00$, stacking fault fringes and both partial dislocations are visible. In Fig. 3(c) taken with $\mathbf{g}_c = 02\bar{2}$, however, stacking fault fringes and partials labelled 2 in (b) are completely invisible, while partials labelled 1 in (b) are visible. In Fig. 3(d) taken with $\mathbf{g}_d = \bar{1}1\bar{1}$, partial dislocations labelled 1 in (b) as well as stacking fault fringes are visible, but partials labelled 2 in (b) are almost invisible. The surface traces of stacking fault planes coincide with the trace of (110) planes. Taking all these facts into account, we can reasonably conclude that the dislocations A to H have the total Burgers vector of $1/2[\bar{1}10]$ and are dissociated into partials on (110) planes by the following reaction:

$$\mathbf{b} = 1/2[\bar{1}10] \rightarrow \mathbf{b}_1 + \mathbf{b}_2 = 1/4[\bar{1}1\bar{1}] + 1/4[\bar{1}11] \qquad (2)$$

Note that $|\mathbf{g}_a \cdot \mathbf{b}|=0$, $|\mathbf{g}_c \cdot \mathbf{b}_1|=1$, $|\mathbf{g}_c \cdot \mathbf{b}_2|=0$, and $|\mathbf{g}_a \cdot \mathbf{b}_1|$, $|\mathbf{g}_a \cdot \mathbf{b}_2|$ and $|\mathbf{g}_d \cdot \mathbf{b}_2|$ are as small as 0·25.

Figure 4(a) is an electron micrograph taken along the [011] direction showing straight dislocations introduced at room temperature. Figure 4(b) is an electron micrograph for the same area taken

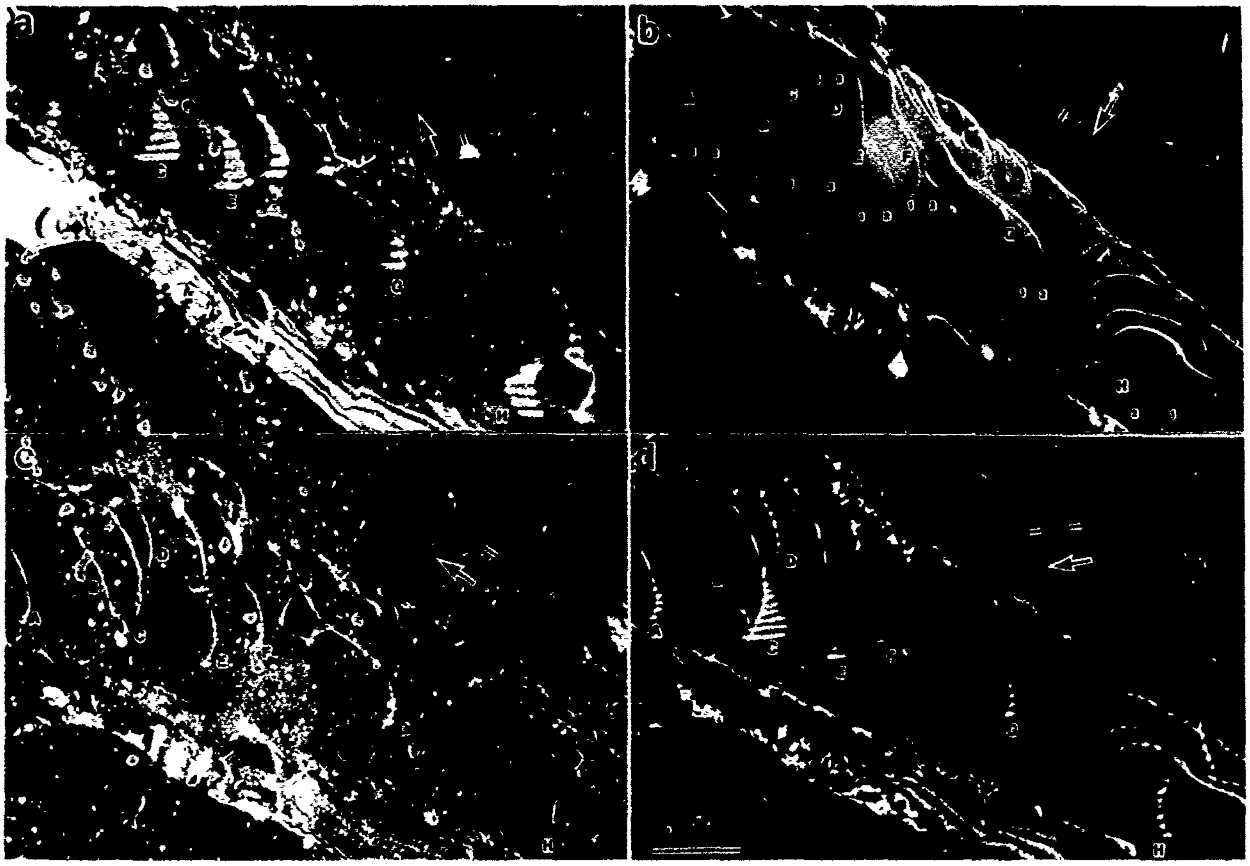

Fig. 3. Weak-beam, dark-field electron micrographs taken from [011] direction under four diffraction conditions for a pulverized sample.

with the same diffraction conditions after a lapse of a few days. It is seen that the initially almost straight dislocations have changed their shape into helical dislocations. Figure 4(c) taken with $\mathbf{g} = \bar{1}11$ which is perpendicular to the dislocation lines, shows that the dislocations are almost out of contrast, indicating that the dislocations were originally screw dislocations with $\mathbf{b} = 1/2[011]$.

The formation mechanism of the helical dislocations is considered to be as follows. The sample of Fig. 4 was prepared from an as-arc-melted crystal, and hence the sample must have contained a considerable number of excess quenched-in vacancies. These vacancies have caused the climb motion of dislocations introduced by pulverization to change them into helical dislocations. We should note that no such helical dislocations were observed in samples deformed at high temperatures. Helical dislocations were first identified by electron microscopy for CaF_2 crystals with the same crystal structure.[5]

In Fig. 4(c), we notice rather strong dotted contrast remaining along the dislocation lines. The contrast could be due to segregation or precipitation of impurities which had existed as supersaturated solid solution in the as-arc-melted sample.

3.2 High resolution electron microscopy

Figure 5 shows a high resolution electron micrograph of a dislocation on a {111} plane viewed along a ⟨110⟩ direction. The dislocation appears to be slightly dissociated on the {111} plane: the dissociation width is seen to be three atomic distances. The dissociation scheme must be the same as that in fcc metals, i.e.

$$1/2[011] \rightarrow 1/6[112]+1/6[\bar{1}21] \qquad (3)$$

In a thicker specimen, we observed an apparently widely dissociated dislocation on a {111} plane with a poor quality of lattice images, but interpretation of such a lattice image will not be straightforward because the dislocation line in the thick part may not be parallel to the electron beam. We observed only a few {111} glide dislocations.

Figures 6 and 7 respectively show an intrinsic stacking fault on {111} and micro-twins with {111} twin boundaries introduced by pulverization. The fact that stacking faults and twin boundaries are stable on {111} planes justifies dislocation dissociation on {111} planes, although Fig. 5 does not exhibit clear dissociation.

Figure 8 is a high resolution electron micro-

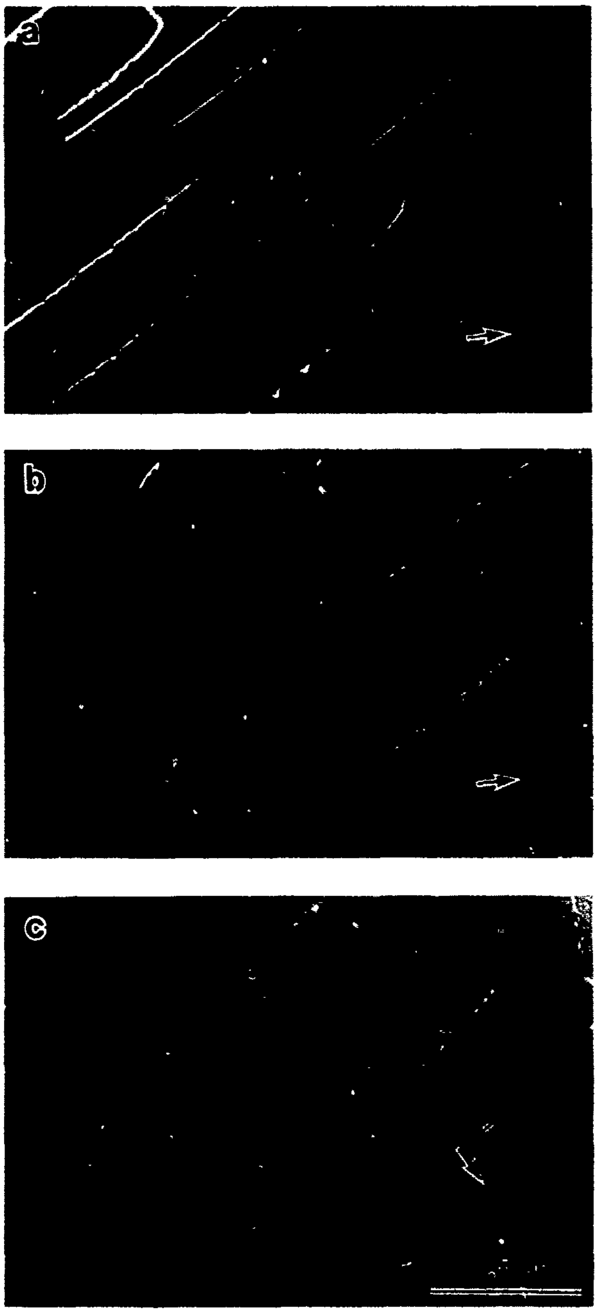

Fig. 4. (a) A weak-beam, dark-field electron micrograph of screw dislocations introduced at room temperature in a pulverized sample. (b) A micrograph as in (a) taken after a lapse of three days, and (c) a micrograph taken under a $\mathbf{g} \cdot \mathbf{b} = 0$ condition.

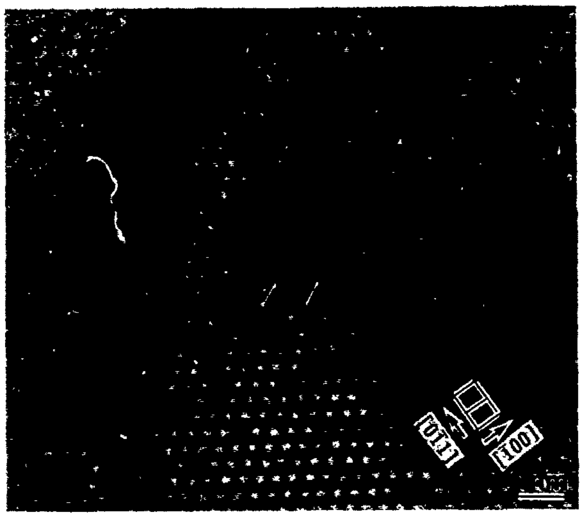

Fig. 5. A high resolution electron micrograph of an edge dislocation on a {111} plane. The projection of a unit cell is given on the micrograph.

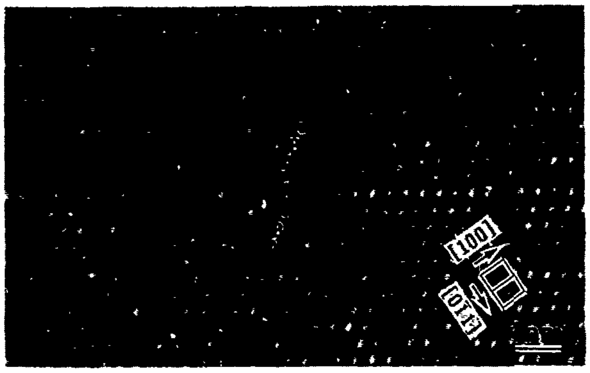

Fig. 6. A high resolution electron micrograph of a {111} stacking fault.

graph showing a special stair-rod dislocation produced possibly as a result of a reaction of two dissociated dislocations on two {111} planes. The well-known stair-rod dislocation in fcc metals is the Lomer–Cottrell dislocation with the Burgers vector $1/6[0\bar{1}1]$ formed at the corner of the stair-rod by the reaction $1/6[\bar{1}12] + 1/6[12\bar{1}] \rightarrow 1/6[0\bar{1}1]$. The reaction in Fig. 8 is not this case, but is considered to be produced as a result of the climb motion of a partial dislocation along the stacking fault plane of another dissociated dislocation after

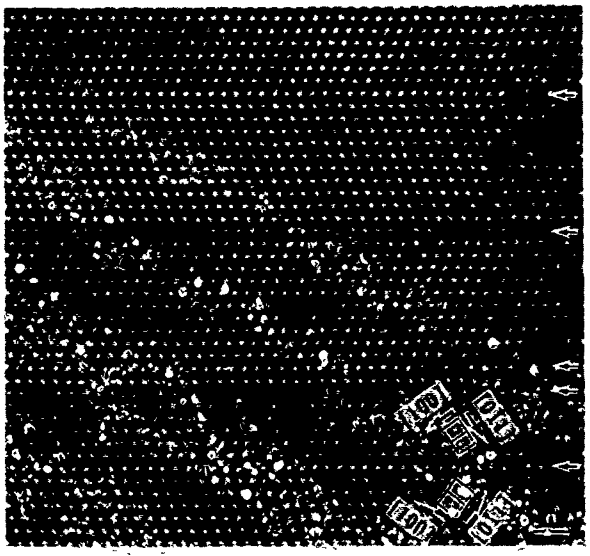

Fig. 7. A high resolution electron micrograph of micro-twins

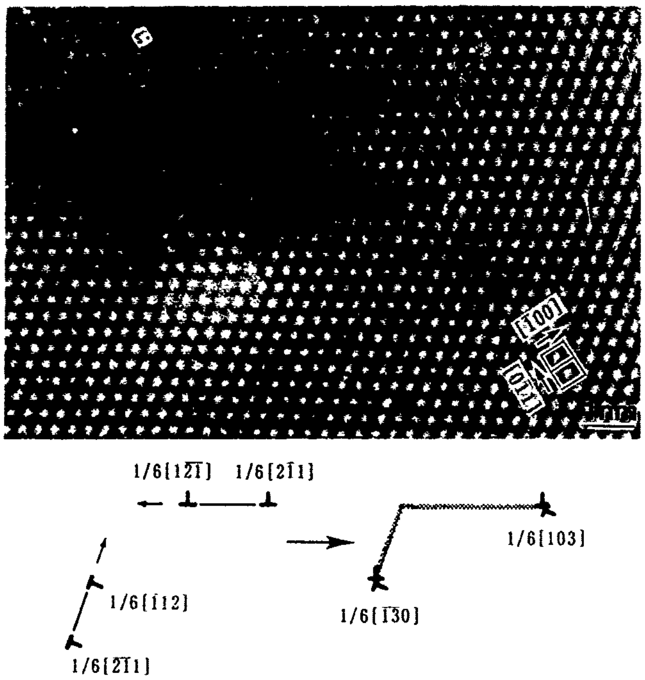

Fig. 8. A high resolution electron micrograph of a stair-rod dislocation. A possible dislocation reaction is depicted.

the encounter of the two dislocations at the intersection of the two {111} slip planes. The possible reaction is depicted in the bottom of Fig. 8. The climb motion may be caused by segregation of impurity atoms.

Figure 9 shows an example of a dissociated dislocation on a {100} plane. The dissociation scheme is probably the same as that of eqn (1) so that the Burgers vector of the partials contains a screw component. In fact, their associated strain field causes a black and white contrast around the partials. We observed a number of such dislocations. The width of dissociation in Fig. 9 is about 2 nm but in other cases, the width was greater than this.

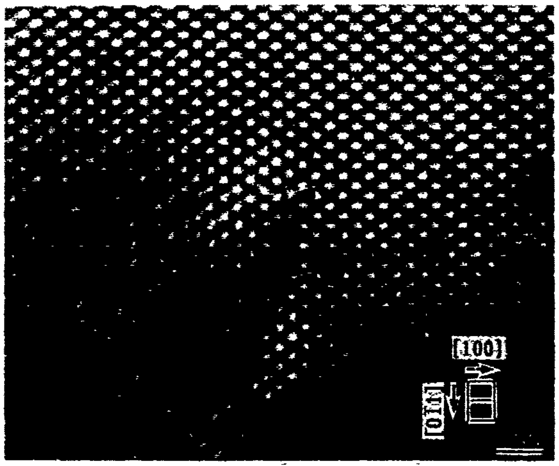

Fig. 9. A high resolution electron micrograph of a dissociated dislocation on a {100} plane.

4 DISCUSSION

The present result shows that in $CoSi_2$, stacking faults are stable on three planes, {100}, {110} and {111} with fault vectors 1/2⟨001⟩, 1/4⟨111⟩ and 1/6⟨112⟩, respectively. In Fig. 10 are shown possible atomic configurations of stacking faults of the three types, Fig. 10(a)–(c), and of a {111} twin boundary, Fig. 10(d). Among them, the atomic structure of the {111} stacking fault (Fig. 10(c)) has shuffle configuration and is a variant of the previously proposed configuration;[1] the present structure explains the high resolution micrograph of Fig. 6 better than the previous one.

As a result of the stability of these faults, dislocations are dissociated on the three different types of plane and this facilitates the operation of three slip systems, {001}⟨100⟩, {110}⟨110⟩ and {111}⟨110⟩, as observed experimentally.[4]

It is difficult to estimate the stacking fault energies, because the observed dissociation of dislocations introduced at room temperature is not necessarily in thermal equilibrium, as is evident from Fig. 3, where the dissociation width varies markedly from place to place. Only dislocations dissociated on {100} planes shown in Fig. 2 have

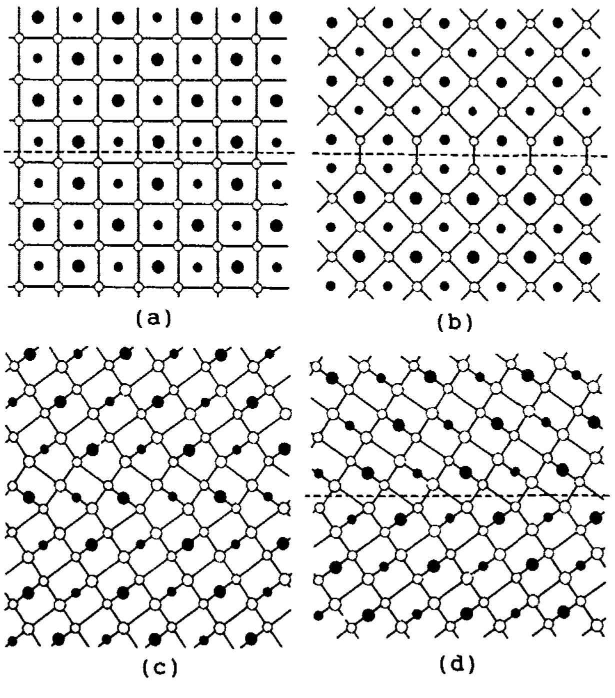

Fig. 10. Possible atomic configurations of three types of stacking faults and a twin boundary: (a) 1/2⟨100⟩ fault on {001} plane, (b) 1/4⟨111⟩ fault on {110} (there exists a displacement component perpendicular to the paper), (c) 1/6⟨112⟩ fault on {111}, and (d) {111} twin boundary. (a) and (b) are viewed along a ⟨100⟩ direction and (c) and (d) along a ⟨110⟩ direction. Closed circles are Co atoms and open circles Si atoms. The sizes of the circles represent the relative positions in the direction perpendicular to the paper.

almost the same width and may be regarded as in equilibrium; this is natural because $\{100\}$ slip is active at room temperature, while $\{110\}$ and $\{111\}$ slip are inactive. The stacking fault energy on the $\{100\}$ plane is estimated to be 17 ± 4 mJ/m^2 using elastic constants of $CoSi_2$ (M. Nakamura, personal communication). The equilibrium dissociation width of $1/2\langle 110\rangle$ dislocations on $\{111\}$ is impossible to resolve by the weak-beam technique and it is probably by the order of 1 nm. That of $1/2\langle 110\rangle$ dislocations on $\{110\}$ may also be of the same order, as inferred from the image contrast of apparently undissociated parts of dislocations A, B, C... in Fig. 3(b). Such a narrow equilibrium width of $1/2\langle 110\rangle$ dislocations on $\{111\}$ and $\{110\}$ explains apparently undissociated dislocation images in Fig. 1; $\{111\}\langle 110\rangle$ and $\{110\}\langle 110\rangle$ slip systems become more active than the $\{001\}\langle 100\rangle$ system only at high temperatures.[4]

Experiments on single crystals by Ito *et al.*[4] showed that $\{100\}$ slip is active in a lower temperature range than $\{110\}$ and $\{111\}$ slips. As a general rule, the larger the h/b value is, the more easily the slip system is activated, where h is the lattice spacing of the slip plane. In Table 1 are listed the magnitude of the Burgers vector of partial dislocations b_p, the lattice spacing of the slip plane h and the ratio h/b_p for three slip systems. It is found that the above general rule is not obeyed in $CoSi_2$; the slip system with the smallest h/b value is actually the most active. To explain the relative activities of three slip systems, more sophisticated consideration is needed.

Table 1. Magnitude of the partial dislocation b_p, lattice spacing of the slip plane h and the ratio h/b_p for three slip systems

Slip system	b_p	h	h/b
$\{001\}\langle 100\rangle$	$a/2\langle 001\rangle = a/2$	$a/4$	$1/2 = 0{\cdot}5$
$\{110\}\langle 110\rangle$	$a/4\langle 111\rangle = \sqrt{3}a/4$	$\sqrt{2}a/4$	$\sqrt{6}/3 = 0\ 816$
$\{111\}\langle 110\rangle$	$a/6\langle 112\rangle = \sqrt{6}a/6$	$\sqrt{3}a/6$	$\sqrt{2}/2 = 0{\cdot}707$

ACKNOWLEDGEMENT

The authors are indebted to T. Hashimoto and M. Ichihara for their help in the experiments.

REFERENCES

1. Takeuchi, S., Hashimoto, T. & Shibuya, T , *J. Mater Sci.*, **27** (1992) 1380.
2. Kelly, A. & Groves, G W., *Crystallography and Crystal Defects*. Addison-Wesley, Reading, Mass., USA, (1970), p. 175.
3 Ito, K., Inui, H., Hirano, T. & Yamaguchi, M. *Mater. Sci. & Eng.*, **A152** (1992) 153.
4. Ito, K., Inui, H., Hirano, T. & Yamaguchi, M. (in press).
5. Bontick, W & Amelinckx, S. *Phil. Mag.*, **2** (1957) 94.

Intermetallics 1 (1993) 29-33

Mechanically-induced phase transformation and magnetic properties of σ-CrFe

H. Yang, L. M. Di & H. Bakker

Van der Waals-Zeeman Laboratory, University of Amsterdam, Valckenierstraat 65, 1018 XE Amsterdam, The Netherlands

(Received 5 November 1992; accepted 10 December 1992)

A phase transformation of σ-CrFe to the bcc solid solution during high-energy ball milling was monitored by X-ray diffraction, AC susceptibility and high-field magnetization measurements. The saturation magnetization shows a maximum as a function of milling time. The increase is ascribed to the phase transformation, the decrease during further milling to the generation of nanocrystalline material. The phase transformation from the σ-phase to the solid solution is discussed in terms of Miedema's semi-empirical model.

Key words: intermetallic compounds, ball milling, phase transformation, magnetic properties, nanocrystalline material.

1 INTRODUCTION

Much attention has recently been given to the formation of amorphous alloys by solid state processing such as mechanical alloying (MA), mechanical milling (MM), etc. However, compounds are also found that transform to the disordered solid solution instead of to the amorphous state. This was found for the A15 compounds Nb_3Al,[1] V_3Ga,[2] and Nb_3Au,[3] and for σ-phase FeV.[4] It is well established now that ball-milling of intermetallic compounds causes atomic (chemical) disorder in those compounds. The energy stored in the form of disorder is assumed to be an important driving force for the transformation,[5] although the energy stored in grain boundaries by crystalline refinement may also contribute to some extent (see Ref. 6 and references given therein). During ball-milling, powder particles are subjected to severe mechanical deformations resulting in a crystallite size reduction to nanometre scales. Therefore, these materials have a high density of interfaces compared to 'normal' polycrystalline materials, and as a consequence, a considerable proportion of atoms are located in the grain boundaries. According to Ref. 7, nanocrystalline materials can be considered to comprise two structural components: crystallites with translational order and the disordered interfacial component, where the latter represents a variety of atomic spacings in different types of interfaces. So the interfacial structure is expected to show a broad distribution and does not exhibit the characteristic short-range order of amorphous materials.

In order to study further phase transformations by mechanical milling, we investigated a possible transformation in σ-CrFe by MM. A rough indication of what kind of transformation (to the solid solution or to the amorphous state) is to be expected is obtained from the phase diagram. In the equilibrium phase diagram the σ-phase of CrFe transforms to the α solid solution at higher temperature. This is a good argument for believing that the solid solution has a lower free energy than the amorphous state as argued in Ref. 5, and that disordering is not able to drive a transformation to amorphous. Another argument is derived from a calculation of enthalpy curves.[6,8] These curves are given in Fig. 1 and it is observed that for the chosen composition (53·5 at.% Fe) the enthalpy of the solid solution is lower than that of the amorphous state.

In the present study, structural changes were monitored by X-ray diffraction and moreover changes in magnetic properties were examined. The magnetic properties were measured by means of

Intermetallics 0966-9795/93/$6.00 © 1993 Elsevier Science Publishers Ltd, England. Printed in Great Britain

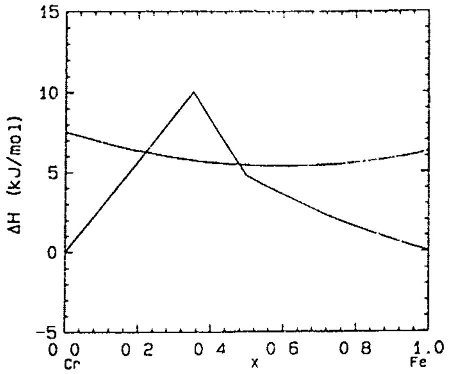

Fig. 1. The formation enthalpies of the solid solution and the amorphous state of the Cr–Fe system. The curve of the solid solution is the one that starts in (0,0) and ends in (1,0).

high-field magnetization and AC susceptibility measurements. Quenching of the α-phase was also performed for comparison.

2 EXPERIMENTAL DETAILS

The $Cr_{0.465}Fe_{0.535}$ sample was prepared from 99·9% purity starting materials. The composition was chosen near the centre of the σ-phase range. After arc-melting in an argon atmosphere, the ingot was wrapped in a tantalum foil and sealed in a quartz tube filled with argon for annealing. Annealing was performed at 800°C for one month and the sample was water quenched.

The ball-milling was carried out in a hardened-steel cylindrical vial with an inner diameter of 6·5 cm with a tungsten carbide bottom using a hardened-steel ball, which was kept in motion by a vibrating frame. The ball diameter was 6 cm. To prevent oxidation and nitridation, the vial was connected to a pumping system and the milling was performed under a vacuum of 10^{-6} Torr. During the milling process, the mill was cooled by high pressure air.

For comparison, powder particles with a diameter between 0·2 and 0·5 mm, were also quenched from above the σ-to-α transition (880°C) by means of a self-constructed quenching device, with a cooling rate of 10^4–10^5 K/s.[9]

X-ray diffraction was measured at room temperature by means of a Philips powder diffractometer using Cu Kα radiation. The magnetization measurements were carried out at 4·2 K in the high-field installation of the University of Amsterdam in fields up to 21 Tesla. The AC susceptibility measurements were performed from room temperature to liquid helium temperature in self-constructed equipment. In this apparatus the sample is mounted in a secondary coil which is connected in series with a counter-clockwise wound identical coil. The coils are placed in a primary coil which generates an AC magnetic field of a few Gauss. A voltage is induced over the secondary coil by mutual inductance which is monitored by a lock-in amplifier. A reference signal is supplied to the lock-in amplifier by a voltage generated by the AC current of the primary coil over a given resistor. Theoretically, the signal over the secondary coil is zero if there is no sample in one of the coils. The coil system with the sample is put in a sample chamber. In the sample chamber a thermometer is placed as well as a heater in order to control the temperature. The sample chamber is separated by an exchange chamber from liquid helium. The cooling of the sample is controlled by the amount of helium gas in the exchange chamber.

3 RESULTS AND DISCUSSIONS

Figure 2 shows the X-ray diffraction patterns for different periods of ball milling and after quenching from 880°C. The X-ray pattern of the starting material, marked as 0 h, is characteristic of the σ-phase. This intermetallic compound exists in the Cr–Fe phase diagram below the α-phase solid solution. From Fig. 2(a), it is clear that with increasing milling time, the intensities of the σ-phase diffraction peaks show a fast decrease, whereas the bcc peaks of the α-phase appear. The background intensity is also increased due to the disordered interfacial structure. After ten hours of milling, only bcc peaks are visible. From this pattern and also from a comparison of this pattern with that of the sample quenched from above the σ-to-α transition (marked as HTP in Fig. 2(b)) it turns out that by ball-milling the σ-phase transforms to the α-phase. Figure 2(b) shows the patterns after prolonged milling time. The samples remain in the bcc structure, but the peaks clearly broaden due to the reduction of the crystallite size. Figure 2(b) also includes the pattern of the sample quenched from 880°C, marked as HTP (high-temperature phase). As expected it is also in the bcc structure, but the peaks are much narrower than those of the ball-milled sample, revealing much bigger crystallites. The broadening of X-ray peaks indicates that the crystallite size decreased with milling time and finally arrived at a nanometre level, so that nanocrystalline material was obtained. On the other hand, the quenched sample has a 'normal' polycrystalline structure.

Let us now compare the magnetic properties of the samples. Figure 3 shows the results of high field measurements up to 21 T at 4·2 K and Fig. 4 shows

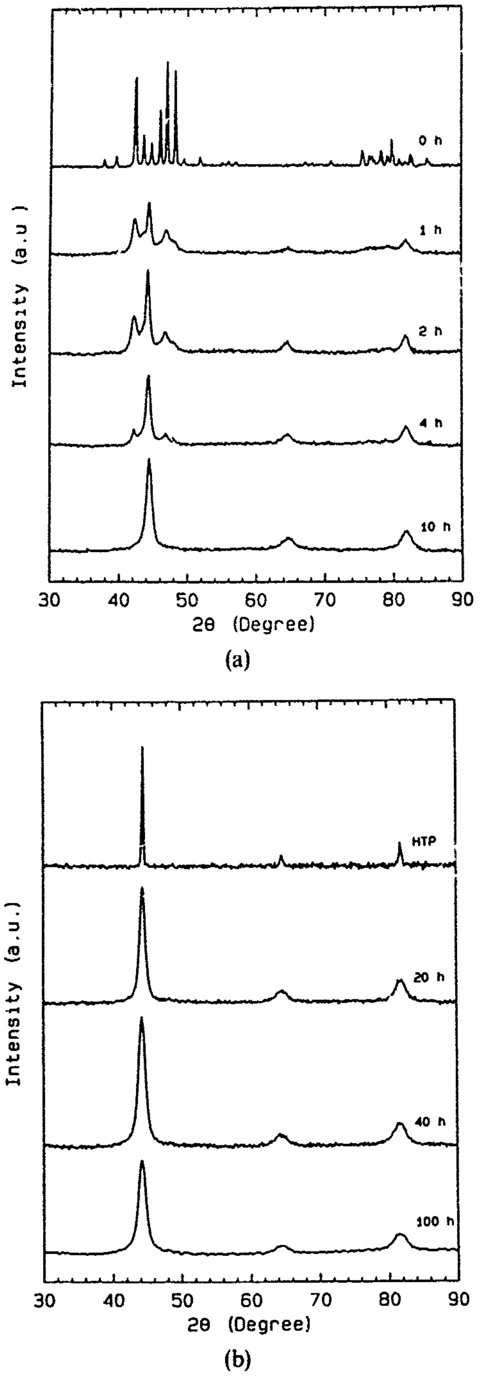

(a)

(b)

Fig. 2. X-ray diffraction patterns of CrFe after different milling times. For comparison, the X-ray diffraction pattern of a quenched CrFe sample (from 880°C) is also included (marked as HTP).

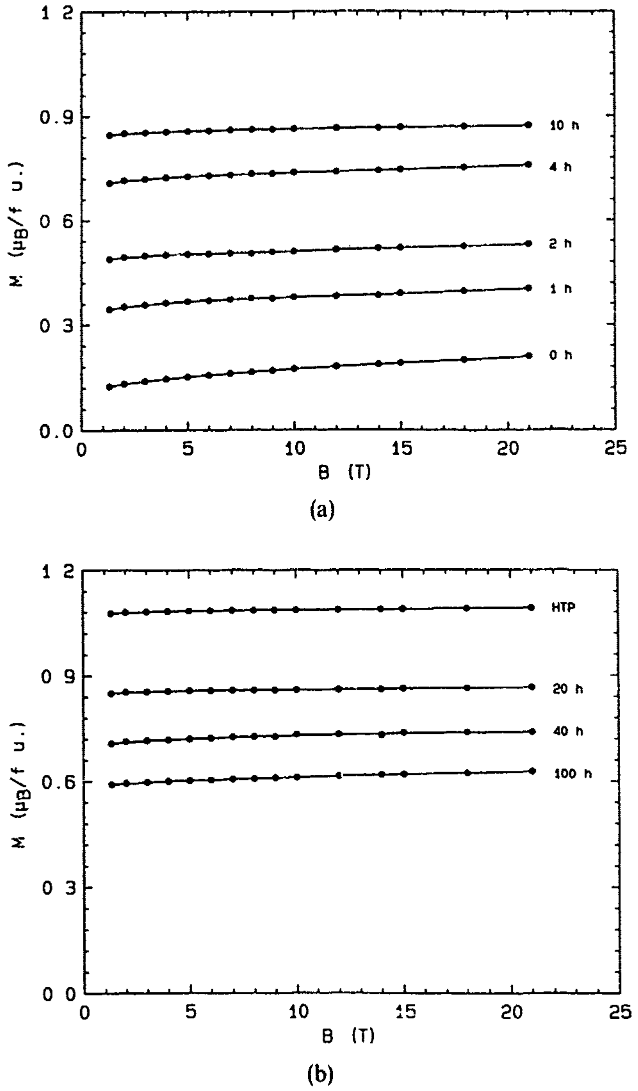

(a)

(b)

Fig. 3. Magnetization at 4·2 K of CrFe after different milling times. The magnetization at 4·2 K of the quenched CrFe sample (from 880°C) is also included for comparison (marked as HTP).

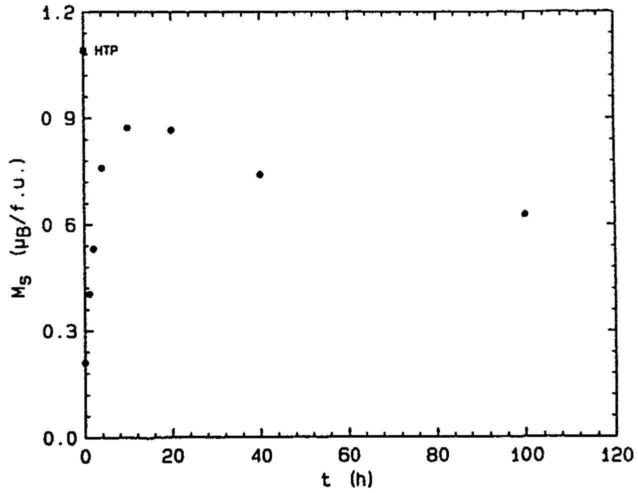

Fig. 4. The saturation magnetization M_s of CrFe as a function of milling time. For comparison, M_s of the quenched CrFe sample (from 880°C) is also included (marked as HTP).

the saturation magnetization M_s as a function of milling time. As M_s the magnetization at 21 T was used. Figure 4 also includes M_s of the quenched sample, which is about 1·1 Bohr magneton per formula unit, the same as the result of Ref. 10 at room temperature. By inspecting Fig. 4 we observe an increase in M_s up to 10 hours of milling. Such an increase is expected on the basis of the X-ray diffraction patterns. The sample transforms from the σ-phase (0 h) with a low magnetization to the α-phase (HTP) with a high magnetization. However the highest magnetization of the ball-milled sample is somewhat lower than that of the quenched sample. This can be ascribed to the finer crystallite size obtained by ball-milling. So the σ-to-α phase transformation is confirmed by these measurements of the saturation magnetization.

From Fig. 3(b) and Fig. 4 it is observed that after 20 hours of milling the saturation magnetization decreases. From the X-ray diffraction patterns (Fig. 2(b)) it is clear that the material remains still in the bcc structure. The explanation is as follows.

During ball-milling, powder particles undergo severe mechanical deformations which result in nanometre-scale crystals. So nanocrystalline material is obtained. The material has a high density of interfaces, much higher than the quenched material, which also has the bcc structure. The interfacial structure is expected to show a broad interatomic distribution. The interfacial neighbourhood strongly determines the magnetic properties of a solid. Therefore, the interfacial atomic distances, different from those in the crystalline materials, are expected to yield considerably different properties of nanocrystalline and chemically identical polycrystalline material. The ferromagnetic properties are expected to change with the interatomic distances. From Ref. 7, the saturation magnetization of nanocrystalline pure Fe appeared to be reduced by 40% in comparison with 'normal' polycrystalline Fe. In our case, the saturation magnetization was increased at first by ball-milling and then reduced with prolonged milling time. The increase during the first stage is due to the σ-to-α transformation as mentioned above. A natural explanation of the decrease in the second stage is the generation of finer and finer crystallites. In fact, what we observed in the magnetization is very similar to observations made by Koch and Lee[11] for Ni_3Al and Ni_3Si. First disordering was observed from the ordered fcc $L1_2$ crystal structure to the fcc structure, then a nanocrystalline grain structure was developed and this structure was refined as milling continued.

The results of AC susceptibility measured as a function of temperature are drawn in Fig. 5. The sample before ball-milling exhibits an obvious peak at around 18 K. With increasing milling time this peak becomes lower and lower and the width of the peak increases slightly in the meantime. After 10 hours of milling, the peak completely disappears. Following Ref. 12, the σ-phase is ferromagnetic at low temperature, and paramagnetic at room temperature. So the peak which we found is related to the magnetic transition from paramagnetism to ferromagnetism. However, the Curie temperature of our sample (about 18 K) is substantially lower than the value of 163 K in Ref. 12. The reason needs further investigation. The conclusion of the AC susceptibility measurements is that the fraction of σ-phase was reduced by ball milling and after 10 hours of milling time a complete transformation to the α-phase has occurred, which phase is ferromagnetic even at room temperature, and indeed we do not observe any magnetic transition in the temperature range up to room temperature.

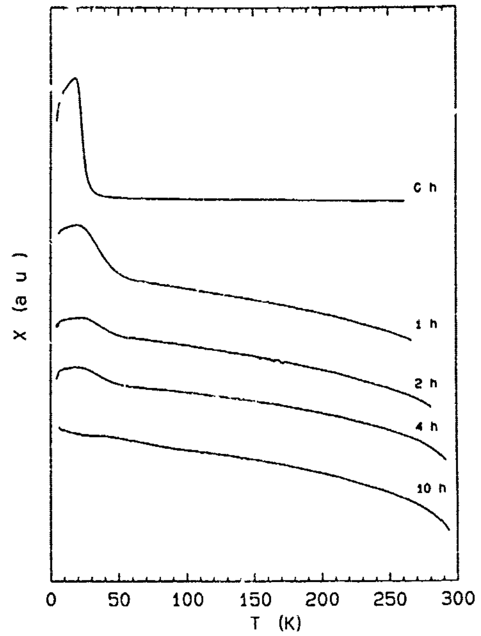

Fig. 5. The results of AC susceptibility measurement of CrFe as a function of temperature after various milling periods

Finally, we comment on the possible role of impurities introduced during the milling. The fact that the milling is performed in vacuum excludes a reaction with gases. Because of the steel vial and ball we used, a little iron may be introduced in the final product. However, with prolonged milling, the saturation magnetization decreases, so that the level of contamination must be low.

In Ref. 6 it was suggested that the small difference in enthalpies between the solid solution and the amorphous state can be overcome by the energy stored in grain boundaries, so that amorphization occurs, whereas on the basis of a diagram of the type of Fig. 1 amorphization is not expected. In the present case the final crystallite size is estimated on the basis of the Scherrer equation as 7 nm, while the enthalpy difference to overcome is only about 2 kJ/mol. From X-ray diffraction there is no indication of amorphization. In this case the grain boundary energy is apparently not high enough to drive the amorphization. To clarify this point further investigation is necessary.

The above experimental results show that ball-milling of an intermetallic compound may lead to a different crystal structure, in our case to the disordered solid solution, and no amorphization was observed. The starting material, i.e., the intermetallic compound, has a lower free energy than the final product. Johnson[13] argued that the internal energy of the compound is raised by ball milling as a result of atomic disordering. This was experimentally confirmed.[5] According to this, if the disordered compound can attain a state of energy higher than the amorphous state, then amorphization will take place. The formation enthalpies of the solid solution and the amorphous state, calculated by Miedema's semi-empirical model,[14] are drawn in Fig. 1. At the composition $Cr_{0.465}Fe_{0.535}$, the curve of the solid solution is below that of the amorphous state. The free energy of the σ intermetallic compound is lower than both of them. High-energy ball milling, the technique used for our experiments, has been confirmed to be an effective method to store energy in the material. When the stored energy in the compound is higher than the formation enthalpy of the solid solution, the transformation from the σ-phase to the α solid solution will take place. Because of the small difference between the formation enthalpies of the solid solution and the amorphous phase (2 kJ/mol), there could be a possibility that enough energy could be stored in the grain boundaries of the nanocrystalline material to overcome this small difference. In such a case amorphization could occur. Such phenomena were discussed in Ref. 6 and really observed by us in Ti_3Al.[15] In the present case there is no such effect and the material remains crystalline with the bcc structure.

4 CONCLUSIONS

The compound σ-CrFe transforms to the bcc solid solution by ball milling. No amorphization occurs. This is in agreement with calculations based on Miedema's semi-empirical model. The saturation magnetization increases as a function of ball milling period first from the σ-phase value to somewhat below the α-phase value and decreases for longer milling period due to the refinement of crystallites to nanocrystallite size.

ACKNOWLEDGEMENTS

The authors thank Dr D. M. R. Lo Cascio, G. F. Zhou and Q. A. Li for discussions and technical help. This work is part of the research programme of the Dutch Foundation for Fundamental Research on Matter (FOM), which is financially supported by the 'Nederlandse Organisatie voor Wetenschappelijk Onderzoek' (NWO).

REFERENCES

1. Oehring, M. & Bormann, R., *J. Phys. Coll.*, **14** (1990) 169
2. Di, L. M. & Bakker, H., *J. Phys. Condens Matter*, **3** (1991) 3427.
3. Di, L. M. & Bakker, H., *J. Phys.: Condens. Matter*, **3** (1991) 9319.
4. Fukunaga, T., Mori, M., Misawa, M. & Mitzutani, U., *Material Science Forum*, **88–90** (1992) 663.
5. Bakker, H. & Di, L. M., *Materials Science Forum*, **88–90** (1992) 27.
6. Yang, H. & Bakker, H., *J. Compounds and Alloys*, **189** (1992) 113.
7. Schaefer, H. E., Wurschum, R., Birringer, R. & Gleiter, H., *J. Less-Common Metals*, **140** (1988) 161.
8. Loeff, P. I., Weeber, A. W. & Miedema, A. R., *J. Less-Common Metals*, **140** (1988) 299.
9. Riemersma, A. J., Manuputy, R. J. D., Schlatter, H., Moolhuyzen, W. F., Rik, R., Lo Cascio, D M. R. & Loeff, P. I., *Rev. Sci. Instrum.*, **62** (1991) 1084.
10. Bozorth, R. M., *Ferromagnetism*. Van Nostrand, Canada, 1951, p. 229.
11. Koch, C. C. & Lee, Y. S., *Nanostruct. Mater.*, **1** (1992) 207.
12. Nevitt, M. V. & Beck, P. A., *Trans. AIME*, **203** (1955) 669.
13. Johnson, W. L., *Prog. Mater. Sci.*, **30** (1986) 81.
14. De Boer, F. R., Boom, R., Mattens, W. C. M., Midema, A. R. & Niessen, A. K., *Cohesion in Metals*, ed. F. R. de Boer & D. G. Pettifor. North-Holland, Amsterdam, 1988, p. 63.
15. Yang, H. & Bakker, H. (in press).

Intermetallics 1 (1993) 35–40

Formation of $AuSb_2$ compound clusters by spontaneous alloying

H. Mori[a] & H. Yasuda[b]

[a]*Research Center for Ultra-High Voltage Electron Microscopy,* [b]*Department of Materials Science and Engineering, Faculty of Engineering, Osaka University, Yamadaoka, Suita, Osaka 565, Japan*

(Received 24 November 1992; accepted 10 January 1993)

The alloying behavior of antimony atoms into nanometer (nm)-sized gold clusters and that of gold atoms into nm-sized antimony clusters has been studied through in-situ deposition experiments in a high-vacuum electron microscope. During experiments, clusters were supported on a carbon film that was kept at ambient temperature. In both cases, vapor-deposited solute atoms quickly dissolved into the clusters and clusters of the intermetallic compounds $AuSb_2$ were formed. This indicates that $AuSb_2$, the melting point of which is 733 K, can easily be formed by simply vapor-depositing either antimony atoms onto gold clusters or gold atoms onto antimony clusters at ambient temperature. A possible mechanism to explain such spontaneous formation of compound clusters is discussed.

Key words. atom clusters, spontaneous alloying, $AuSb_2$, in-situ experiment, transmission electron microscopy (TEM)

1 INTRODUCTION

In recent years, there has been considerable interest in understanding the structure and property of ultrafine particles in the size range of a few to several nanometers (nm), since such particles often exhibit physical and chemical properties that are significantly different from those of the corresponding bulk solids[1]. (Hereafter, such ultrafine particles are designated *atom clusters* or simply *clusters.*) Most recent studies on atom clusters have been focused on understanding their unusual electronic, optical, and magnetic properties and considerable progress has been made in this field.[1,2] To the authors' knowledge, however, only little work has been conducted on the diffusion properties of atom clusters—in particular, on the interdiffusion or alloying behavior in atom clusters. From this point of view, in our previous studies, alloying behavior in atom clusters was investigated by electron microscopy, and it was revealed that even at ambient temperature rapid dissolution of solute atoms such as copper takes place in nm-sized gold clusters[3] and that such spontaneous alloying takes place without visible translational motion of individual clusters on a supporting film.[4]

The gold–copper binary system employed in the previous work is a typical solid solution system. In the present work, we investigate alloying behavior in atom clusters in the gold–antimony binary system to see whether or not a similar spontaneous alloying takes place in such systems which form one or more compounds. The reasons for choosing the gold–antimony system are two-fold; first, not only gold but also antimony atoms possess little reactivity with residual gases in the electron microscope; and, secondly, this system forms only one compound, $AuSb_2$, as shown in Fig. 1,[5] which facilitates the analysis of the experimental results a great deal. It is here reported for the first time that the intermetallic compound $AuSb_2$, the melting point of which is 733 K,[5] can be successfully produced by spontaneous alloying at *ambient temperature.*

2 EXPERIMENTAL PROCEDURES

Preparation of gold clusters and subsequent antimony deposition onto the gold clusters, and vice versa, was carried out with a double-source evaporator set in the specimen chamber of an electron microscope. The evaporator consists of two spiral-shaped tungsten filaments. An amorphous carbon

Intermetallics 0966-9795/93/$6.00 © 1993 Elsevier Science Publishers Ltd, England Printed in Great Britain

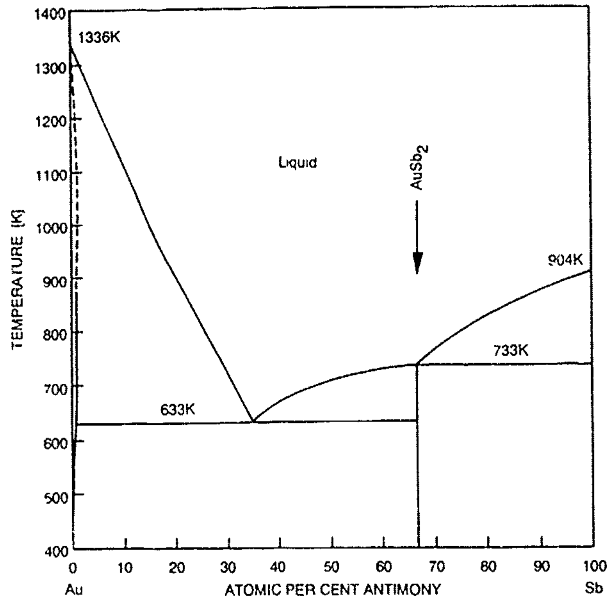

Fig. 1. Phase diagram for the gold–antimony alloy system.

film was used as a supporting film and it was mounted on a molybdenum grid kept at ambient temperature. The distance between the filaments and the supporting film (substrate) for atom clusters was approximately 100 mm. Using the evaporator, gold (antimony) was first evaporated from one filament to produce nm-sized gold (antimony) clusters on the supporting film. Antimony (gold) was then evaporated from the other filament onto the same film. The flux of depositing atoms was of the order of $10^{18}/m^2$ s. Changes in the morphology and structure of gold (antimony) clusters caused by depositing antimony (gold) atoms on the clusters were monitored by taking bright-field images (BFIs) and selected area electron diffraction patterns (SAEDs).

The microscope used was equipped with a turbo-molecular pumping system to achieve a base pressure of about 5×10^{-5} Pa in the specimen chamber and was operated at an accelerating voltage of 200 kV. The electron flux used was approximately $1{\cdot}5 \times 10^{20}$ e/m^2·s.

3 RESULTS

3.1 Formation of AuSb$_2$ compound clusters by depositing antimony atoms onto gold clusters

An example of AuSb$_2$ compound clusters produced by depositing antimony atoms onto gold clusters is shown in Fig. 2. Figures 2(a) and (a') show a BFI of gold clusters formed on a supporting film and the corresponding SAED, respectively. The mean diameter of gold clusters is about 4 nm. The Debye–Scherrer rings in the SAED are consistently indexed as those of fcc gold. Figures 2(b) and (b') depict a BFI of the clusters after antimony deposition for about 60 s and the corresponding SAED, respectively. These photographs were taken immediately after antimony deposition; that is, in less than 20 s after the antimony atom beam was turned off. With antimony deposition, the mean cluster diameter has been found to increase from about 4 to 7 nm. An enlargement of the SAED is shown in Fig. 3. As illustrated in Fig. 3, the Debye–Scherrer rings can be consistently indexed as those of AuSb$_2$, which has the C2 structure with a lattice constant of $a_0 = 0{\cdot}666$ nm.[6] These observations clearly indicate that vapor-deposited antimony atoms have come in contact with gold clusters on the supporting amorphous carbon film and dissolved quickly into the interior of gold clusters to form clusters of the intermetallic compound AuSb$_2$. It should be noted that AuSb$_2$, the bulk melting point of which is 733 K, can be easily formed by simply vapor-depositing gold atoms onto antimony clusters supported on a carbon substrate kept at ambient temperature.

3.2 Formation of AuSb$_2$ compound clusters by depositing gold atoms onto antimony clusters

An example of AuSb$_2$ compound clusters produced by depositing gold atoms onto antimony clusters is shown in Fig. 4. Figures 4(a) and (a') show a BFI of antimony clusters formed on an amorphous carbon film and the corresponding SEAD, respectively. The mean diameter of antimony clusters is about 10 nm. The number density of antimony clusters is approximately $2 \times 10^{15}/m^2$ and is lower than that of gold clusters, as seen from a comparison of Fig. 4(a) with Fig. 2(a). The lower number density of antimony clusters is ascribed to a long mean free path of antimony atoms on the carbon substrate in comparison with that of gold atoms. (Mean free path is taken as the mean distance over which atoms migrate on the substrate before they aggregate to form clusters.) Figures 4(b) and (b') show a BFI of clusters after gold deposition for about 30 s and the corresponding SAED, respectively. The flux of gold atoms was also of the order of $10^{18}/m^2$·s. These photographs were also taken immediately after gold deposition. As seen in Fig. 4(b) two distinct groups of clusters are formed by gold deposition: clusters with a mean diameter of about 4 nm and clusters with a mean diameter of about 13 nm. An enlargement of the SAED is depicted in Fig. 5.

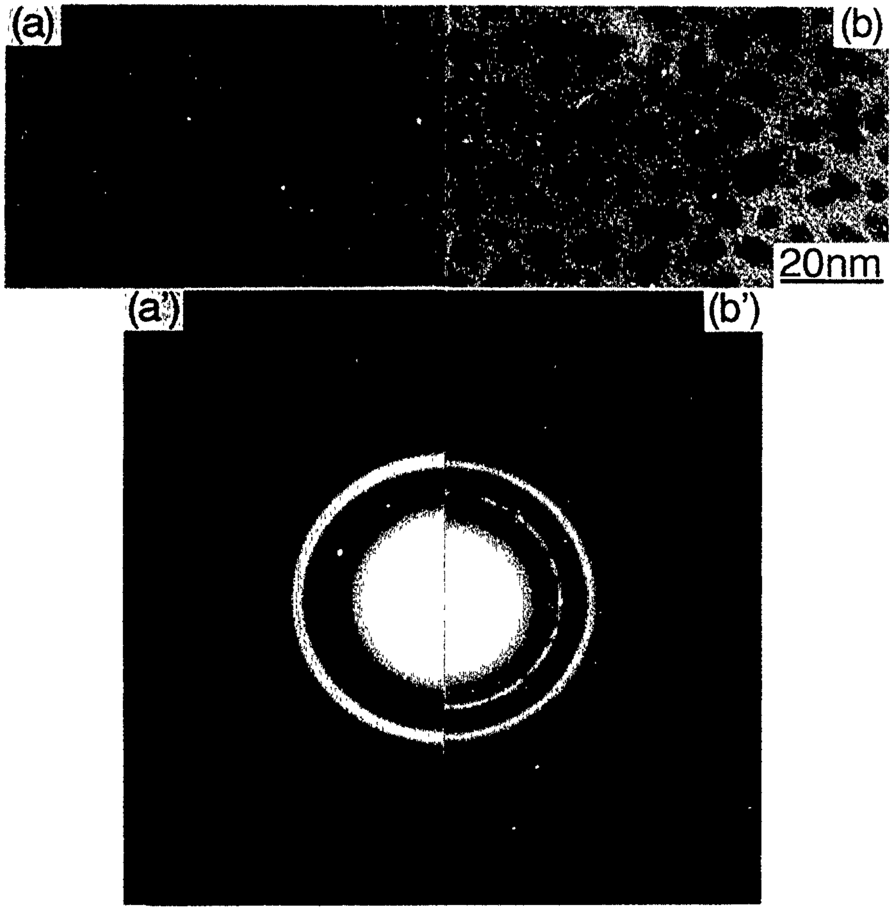

Fig. 2. Spontaneous alloying of antimony atoms into gold clusters at ambient temperature. (a) A BFI of as-produced gold clusters on an amorphous carbon film and (a') the corresponding SAED. (b) A BFI of clusters after depositing antimony atoms for about 60 s and (b') the corresponding SAED.

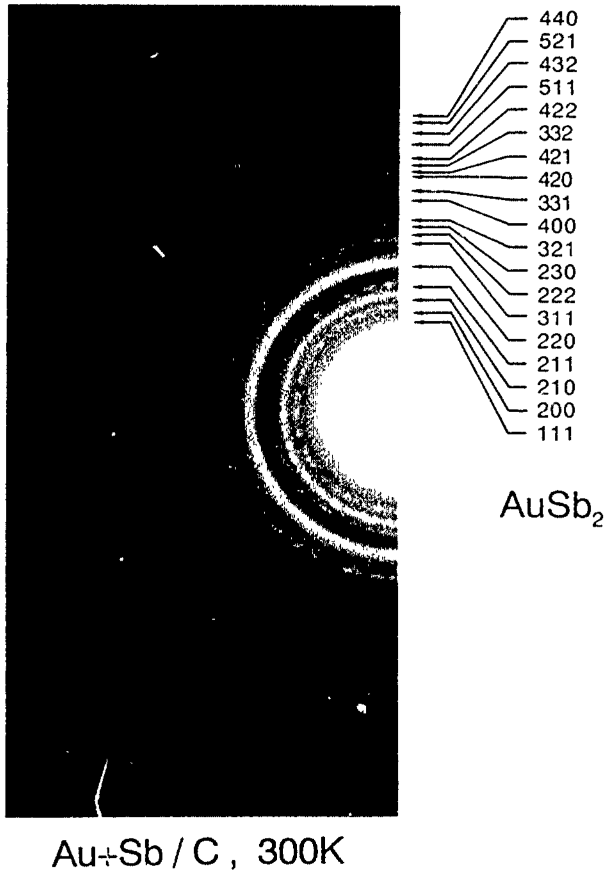
440
521
432
511
422
332
421
420
331
400
321
230
222
311
220
211
210
200
111
$AuSb_2$
Au+Sb / C , 300K

Fig. 3. An enlargement of the SAED shown in Fig. 2(b'). The Debye–Scherrer rings can be consistently indexed as those of $AuSb_2$ which has the C2 structure with a lattice constant of $a_0 = 0\ 666$ nm.

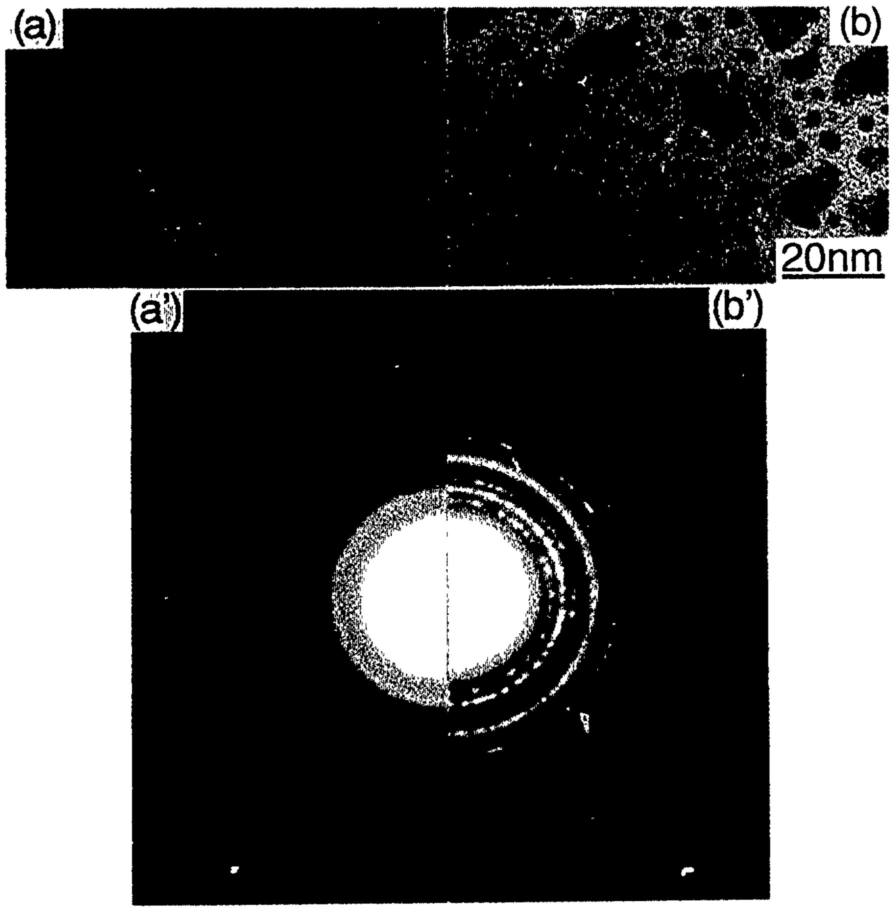

Fig. 4. Spontaneous alloying of gold atoms into antimony clusters at ambient temperature. (a) A BFI of as-produced antimony clusters on an amorphous carbon film and (a') the corresponding SAED. (b) A BFI after depositing gold atoms for about 30 s and (b') the corresponding SAED.

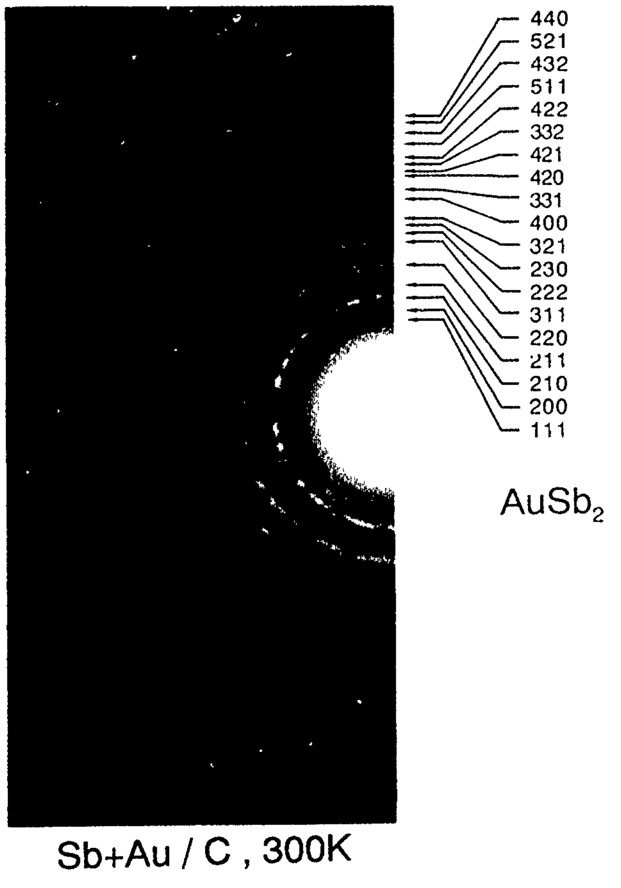
440
521
432
511
422
332
421
420
331
400
321
230
222
311
220
211
210
200
111
AuSb$_2$
Sb+Au / C , 300K

Fig. 5. An enlargement of the SAED shown in Fig. 4(b'). The Debye—Scherrer rings can be consistently indexed as those of AuSb$_2$ superimposed on those of fcc gold.

The Debye–Scherrer rings in Fig. 5 can be consistently indexed as those of $AuSb_2$ superimposed on those of fcc gold. It is, however, difficult to clearly indicate the Debye–Scherrer rings of fcc gold because (1) their intensity is weaker than that of the rings of $AuSb_2$ and (2) the 111, 002, 022, and 113 rings of fcc gold and the 220, 311, 421, and 432 rings of $AuSb_2$ are almost overlapping.

A preliminary high-resolution electron microscopy (HREM) study of such clusters as those shown in Fig. 4(b) has revealed that the smaller clusters with a mean diameter of about 4 nm correspond to clusters of fcc gold whereas the larger clusters with a mean diameter of about 13 nm correspond to those of $AuSb_2$. The formation of the smaller fcc gold clusters, which are dispersed among the larger $AuSb_2$ clusters, is ascribed to the fact that the mean free path of gold atoms is shorter than that of antimony atoms.

From these observations it is evident that, even at such reduced temperatures as ambient temperature, nm-sized antimony clusters can easily change into $AuSb_2$ clusters when an appropriate amount of gold is deposited onto them.

4 DISCUSSION

In this paper, the alloying behavior of antimony atoms into nm-sized gold clusters and that of gold atoms into nm-sized antimony clusters have been studied at ambient temperature through in-situ deposition experiments in a high-vacuum electron microscope. It is found that vapor-deposited gold (antimony) atoms quickly dissolve into antimony (gold) clusters and transform into clusters of the intermetallic compound $AuSb_2$. Of interest is that the $AuSb_2$, the melting point of which is 733 K, can be produced by such spontaneous alloying even at ambient temperature.

It should be worthwhile to estimate the diffusivity of solute atoms in nm-sized atom clusters from the present results and to compare the value obtained with the corresponding bulk diffusivity. The diffusivity of antimony in gold clusters and bulk gold can be estimated. A simple relationship

$$x = (Dt)^{1/2}$$

can be used for a rough estimate of the diffusion coefficient D, where t is the time needed to achieve appreciable diffusion of solute atoms over a distance x.[7] With $x = 2$ nm (half the average diameter of gold clusters shown in Fig. 2(a)) and $t = 20$ s, a value of 2×10^{-19} m²/s is obtained for D. This value gives a guide for the lower limit of the diffusivity of antimony in nm-sized gold clusters at ambient temperature, since the alloying takes place in less than 20 s. The diffusion coefficient of antimony in bulk gold, $D_{\rm Bulk}$ (in m²/s), can be expressed as

$$D_{\rm Bulk} = (1{\cdot}14 \times 10^{-6}) \exp(-15500/T)$$

where T is the temperature.[8] Extrapolation of this relationship to ambient temperature gives a value of $4{\cdot}2 \times 10^{-29}$ m²/s for $d_{\rm Bulk}$ at 300 K. Thus, the antimony diffusivity in nm-sized gold clusters observed in the present work is at least 10 orders of magnitude faster than that in bulk gold. Similar enhanced diffusivity of solute atoms in atom clusters has been observed for copper atoms in gold clusters in our previous work.[3,4]

The temperature of nm-sized gold clusters would be increased by (1) electron-beam heating, (2) heat of condensation, and (3) collision with antimony atoms with a kinetic energy of the order of kT. However, the temperature rises caused by these three effects were ~10, ~10^{-3} and ~10^{-5} K, respectively.[9] The maximum temperature rise is thus expected to be only ~10 K, because of electron-beam heating. This indicates that the rapid spontaneous alloying and subsequent compound formation observed in this study is not an artifact originating from the temperature rise of the atom clusters but an intrinsic property of the nm-sized clusters.

The mechanism behind such rapid spontaneous alloying is not clear yet. However, recent in-situ depositing experiments conducted at low (100–200 K) temperatures on nm-sized clusters in the gold–copper system have led to the conclusion that the spontaneous alloying proceeds not by the conventional diffusion mechanism, which predicts alloying kinetics proportional to $t^{1/2}$, but by an abrupt process which occurs once when solute atoms have come in contact with clusters.[10] Ajayan and Marks[11] have pointed out that for metal atom clusters in the size range of a few nm, the Gibbs free-energy surface as a function of the morphology of clusters is quite shallow. Then there may be a possibility that condensation of antimony atoms on a gold cluster or of gold atoms on an antimony cluster will excite the cluster from the original stable state into an unstable fluctuating state for a short period, where the cluster repeatedly changes shapes among various structures. During this period the cluster will change into an alloyed cluster, and after this short period the alloyed cluster will then fall into its own final stable state. Such a structural fluctuation of short duration, if present, may be a candidate for the one-time and abrupt process responsible for the spontaneous alloying. Studies to elucidate the process are in progress in our laboratory.

5 CONCLUSIONS

The alloying behavior of antimony atoms into nm-sized gold clusters and that of gold atoms into nm-sized antimony clusters have been studied through in-situ deposition experiments in a high-vacuum electron microscope. During experiments, clusters were supported on a carbon film that was kept at ambient temperature. In both cases, vapor-deposited solute atoms quickly dissolved into clusters and they transformed into clusters of the intermetallic compound $AuSb_2$. This indicates that the intermetallic compound $AuSb_2$, the bulk melting point of which is 733 K, can be easily produced by such spontaneous alloying, even at ambient temperature.

ACKNOWLEDGEMENTS

The authors would like to thank Mr H. Hayasaki for his technical assistance. One of the authors (H.M.) acknowledges the financial support of the Japanese Ministry of Education, Science and Culture through a Grant-in-Aid for Scientific Research on the priority area 'Intermetallic Compounds as New High-Temperature Structural Materials' (Grant number 0423-9105).

REFERENCES

1. Andres, R. P., Averback, R. S., Brown, W. L., Brus, L. E., Goddard, W. A., Kaldor, A., Louie, S. G., Moscovits, M., Peercy, P. S., Riley, S. J., Siegel, R. W., Spaepen, F. & Wang, Y., *J. Mater Res.*, **4** (1989) 704.
2. Tang, Z. X., Sorensen, C. M., Klabunde, K. J. & Hadjipanayis, G. C., *Phys. Rev. Lett.*, **67** (1991) 3602.
3. Mori, H., Komatsu, M., Takeda, K. & Fujita, H., *Phil. Mag. Lett.*, **63** (1991) 173.
4. Yasuda, H., Mori, H., Komatsu, M., Takeda, K. & Fujita, H., *J. Electron Microsc.*, **41** (1992) 267.
5. Okamoto, H. & Massalski, T. B., in *Binary Alloy Phase Diagrams* ed. T. B. Massalski *et al.* ASM, Metals Park, Ohio, 1986, p. 305.
6. Villars, P. & Calvert, L. D., *Pearson's Handbook of Crystallographic Data for Intermetallic Phases*. ASM, Metals Park, Ohio, 1985, p. 1231.
7. Barrett, C. R., Nix, W. D. & Tetelman, A. S., *The Principles of Engineering Materials*. Prentice-Hall, Englewood Cliffs, New Jersey, 1973, p. 150.
8. Girifalco, L. A., *Atomic Migration in Crystals*. Blaisdell, Waltham, Massachusetts, 1964.
9. Yasuda, H. & Mori, H., *J. Vac. Sci. B*, to be published
10. Yasuda, H., Mori, H., Komatsu, M. & Takeda, K., *J. Appl. Phys.*, 73 (1993) 1100
11. Ajayan, P. M. & Marks, L. D., *Phys. Rev. Lett.*, **60** (1988) 585.

Intermetallics 1 (1993) 41–48

Formation of ternary $L1_2$ compounds in Al_3Ti-base alloys

Y. Nakayama & H. Mabuchi

Department of Metallurgical Engineering, University of Osaka Prefecture, Osaka 593, Japan

(Received 25 November 1992; accepted 15 January 1993)

Sintering of elemental powders was carried out to form ternary intermetallic compounds in Al–Ti–X systems. It was confirmed that $L1_2$ ternary compounds are formed in Al_3Ti-base alloys containing Cr, Mn, Fe, Co, Ni, Cu, Zn, Rh, Pd, Ag, Pt, and Au. In some ternary systems, the $L1_2$ phase field and equilibrium phases surrounding the $L1_2$ phase at 1273 K or 1423 K have been established. Button ingots of some ternary $L1_2$ compounds were prepared by arc-melting to investigate their microstructure and bend ductility. In general, homogenization of as arc-melted button ingots substantially reduces the amount of second phases but introduces extensive porosity. However, no residual porosity was observed in higher Cr content alloys: $Ti_{25}Cr_{13}Al_{62}$, $Ti_{25}Cr_{14}Al_{61}$, and $Ti_{25}Cr_{16}Al_{59}$. For $Ti_{25}Cr_{14}Al_{61}$ alloy, a bend ductility as large as 0.9% was recorded at ambient temperature.

Key words: $L1_2$ trialuminides, Al–Ti–X phase diagrams, microstructure evolution, ductility improvement

1 INTRODUCTION

The intermetallic compound Al_3Ti is attractive as a potential high-temperature structural material because of its relatively high melting point, light weight, and good oxidation resistance.[1] However, it has the low-symmetry tetragonal $D0_{22}$ structure and is brittle at room temperature. Successful development of the aluminide depends on whether we can overcome its brittleness at ambient temperature. One possible approach to ductilizing ordered intermetallics with low-symmetry crystal structures is to transform their structures to those of higher symmetry. The tetragonal $D0_{22}$ structure is derived from the cubic $L1_2$ structure by displacing every (001) plane by a vector of 1/2[110]. The $D0_{22}$–$L1_2$ transition should be possible through alloying Al_3Ti with ternary alloying elements which cause relatively minor adjustments in the average atomic size and/or atomic valence of the alloy components. Indeed, it is known that replacing a certain amount of aluminum atoms in Al_3Ti with Zn, Ni Cu, or Fe transforms the structure of Al_3Ti to the $L1_2$ structure.[2-5] Recently, considerable attention has been focused on the ternary $L1_2$ structure compounds in the Al–Ti–Ni, Al–Ti–Fe, and Al–Ti–Cu systems.[6-16] More recently, Zhang *et al.*[17] and the authors[18-20] found the formation of new ternary $L1_2$ compounds in Al_3Ti-base alloys containing Mn, Cr, and Ag. Powers and Wert[21] have also reported the existence of an $L1_2$ compound with the composition $Ti_{25}Pd_8Al_{67}$ in the Al–Ti–Pd system.

Much work[22-31] has been carried out also on the mechanical properties and microstructure–mechanical property relationships of the ternary $L1_2$ tri-aluminide compounds. However, the ternary $L1_2$ compounds are still brittle in tension and/or bending, although they exhibit appreciable compressive ductility at ambient temperature. In the present work, various ternary systems, Al–Ti–X (X = V, Cr, Mn, Fe, Co, Ni, Cu, Zn, Nb, Mo, Rh, Pd, Ag, Pt, and Au), were investigated to confirm new ternary $L1_2$ compounds and a preliminary study was made on the mechanical properties, e.g., bend ductility at room temperature, and microstructure–mechanical property relationships for some of the ternary $L1_2$ compounds.

2 EXPERIMENTAL PROCEDURES

Samples in the present investigation were prepared using two different methods. First, alloys were

Intermetallics 0966-9795/93/$6.00 © 1993 Elsevier Science Publishers Ltd, England. Printed in Great Britain

Table 1. The phases and lattice parameters determined by XRD analysis in the various sintered alloys

Alloy composition at.%	Sintering conditions (K, h)	Major phase	Minor phase	Lattice parameter of $L1_2$ (nm)
$Ti_{25}V_8Al_{67}$	1423, 24	$D0_{23}$	Al_8V_5	
$Ti_{25}Cr_8Al_{67}$	1273, 12	$L1_2$		0·3960
$Ti_{25}Mn_9Al_{66}$	1273, 12	$L1_2$		0·3955
$Ti_{25}Fe_8Al_{67}$	1273, 24	$L1_2$	Al_2FeTi	0·3940
$Ti_{25}Co_8Al_{67}$	1423, 24	$L1_2$	Al_2CoTi	0·3950
$Ti_{25}Ni_8Al_{67}$	1273, 24	$L1_2$	Al_2Ni_2	0·3940
$Ti_{25}Cu_{12\cdot5}Al_{62\cdot5}$	1273, 12	$L1_2$		0·3930
$Ti_{25}Zn_9Al_{66}$	1273, 12	$L1_2$	Al_3Ti	0·3960
$Ti_{25}Nb_8Al_{67}$	1423, 24	$D0_{22}$	$TiAl_2$	
$Ti_{25}Mo_8Al_{67}$	1423, 24	$D0_{22}$	$TiAl_2$	
$Ti_{27}Rh_6Al_{67}$	1423, 24	$L1_2$		0·3965
$Ti_{25}Pd_8Al_{67}$	1423, 24	$L1_2$	?	0·3950
$Ti_{25}Ag_8Al_{67}$	1273, 12	$L1_2$		0·3990
$Ti_{27}Pt_6Al_{67}$	1423, 24	$L1_2$		0·3965
$Ti_{25}Au_9Al_{66}$	1423, 24	$L1_2$		0·3975

prepared by sintering compacts made from the elemental powders: aluminium (99·9%, 200 mesh), titanium (99·5%, 325 mesh—containing about 3500 mass ppm oxygen), and various high-purity X (X = V, Cr, Mn, Fe, Co, Ni, Cu, Zn, Nb, Mo, Rh, Pd, Ag, Pt, or Au—at least 99·9%, about 200 ~ 300 mesh) powders. These powders were mixed to obtain the nominal alloy compositions, $Ti_{25}X_8Al_{66}$, $Ti_{25}X_9Al_{66}$, $Ti_{25}Cu_{12\cdot5}Al_{62\cdot5}$, $Ti_{27}X_6Al_{67}$ (which are listed in Table 1) and $Ti_xX_yAl_z$ ($x = 0$–50, $y = 0$–60 and $z = 30$–80 at.%) (see later, Figs 2–4). The powder mixtures, approximately 2 g, were pressed at about 260 MPa into cylindrical compacts of 10 mm diameter. The compacts were sintered in a tube furnace under a vacuum of 1×10^{-4} Pa for 12 h or 24 h at 1273 K or 1423 K in order for near-equilibrium conditions to be obtained. After sintering, the specimens were quenched in blowing air from the sintering temperature to ambient temperature. Weight loss was checked after sintering and was found to be insignificant (less than 0·5%). Thus, we used the nominal compositions as the compositions of specimens. The samples were then pulverised to a 300 mesh size. The powdered specimens were analyzed by X-ray diffraction (XRD) to identify the constituent phases in the sintered products. The X-ray radiation used was CuKα.

Secondly, using pure elemental materials (Al, 99·999%; Ti, 99·9%; Cr, 99·999%; Mn, 99·99%; Ni, 99·9%; Cu, 99·99%; and Ag, 99·9%), button ingots, approximately 30 g, with the target compositions $Ti_{25}Cr_8Al_{67}$, $Ti_{25}Mn_9Al_{66}$, $Ti_{25}Ni_8Al_{67}$, $Ti_{25}Cu_{12\cdot5}Al_{62\cdot5}$, $Ti_{25}Ag_8Al_{67}$, and $Ti_{25}Cr_xAl_{75-x}$ (x = 13, 14, and 16 at.%), were prepared by nonconsumable electrode arc melting under an argon atmosphere. The arc-melted buttons were remelted several times (at least five times) to promote chemical homogeneity. Furthermore, a portion of alloy buttons was homogenized at 1423 K in vacuum for two days to assure the homogeneity of chemical composition and microstructure. The as-cast and homogenized specimens were microstructurally characterized using X-ray diffraction, optical microscopy, and scanning electron microscopy (SEM). Specimens for microscopy were mechanically polished and then electropolished with 300 ml CH_3OH + 170 ml C_4H_9OH + 30 ml $HClO_4$ solution. Compositions of the matrix and second phases were assessed by energy dispersive X-ray (EDX) spectroscopy. Vickers microhardness tests were performed on the $L1_2$ matrix phase using a 25 g load. Specimens for bend testing with dimensions of approximately $25 \times 5 \times 2$ mm^3 were prepared from the homogenized materials. The surface of the specimens was polished using 600 grid emery paper and cleaned with acetone. Three-point bend tests were then performed at ambient temperature in air using an Instron testing machine at a constant cross-head deflection rate of 0·1 mm min^{-1}. Strain was precisely measured with a strain-gage attached to the tension side of specimens.

3 RESULTS AND DISCUSSION

3.1 Examinations of sintered alloys

Figure 1 shows the change of X-ray diffraction patterns with increasing time of sintering at 1273 K for a specimen with a composition $Ti_{25}Cr_8Al_{67}$. The phases identified by X-ray analysis are presented in this figure. Calculated reflections and their estimated intensity for the $L1_2$ compound, which is expected to be obtained in the specimen, were also shown. In the early stage of sintering (1·5 h), the $D0_{22}$ compound with the Al_3Ti composition is dominantly formed since Cr is very slightly soluble in the Al_3Ti phase with the $D0_{22}$ structure. This is similar to the results of the study by van Loo and Rieck;[32] diffusion–couple experiments in the binary Al–Ti system, in which aluminum is one of the starting materials, have shown that aluminum is the only diffusing component and that only one phase, Al_3Ti, develops. However, after 6 h sintering, significant changes in the constituent phases occur as a result of interdiffusion in the Al_3Ti and residual Ti and Cr. The new dominant compound was identified as a cubic

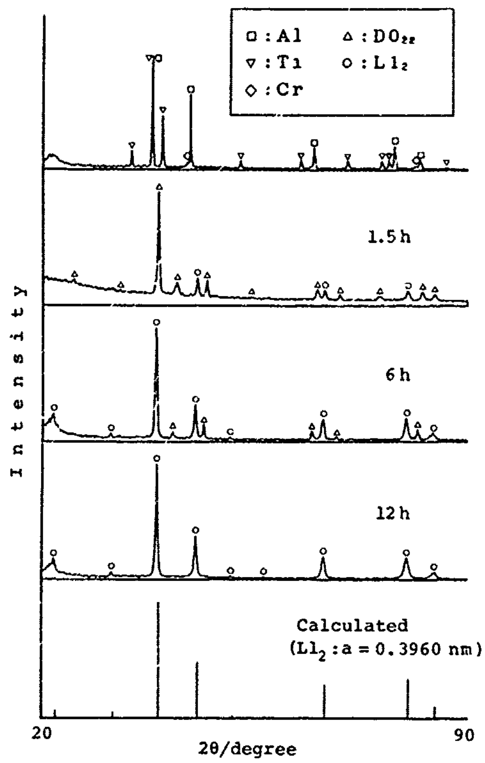

Fig. 1. X-ray analysis for sintered $Ti_{25}Cr_8Al_{67}$ specimens, showing the change of XRD patterns with increasing time of sintering at 1273 K and the calculated diffraction spectrum for the $L1_2$ structure.

$L1_2$ compound with a lattice parameter of a = 0·3960 nm. With increasing sintering time, the diffusion reaction progressed further, and finally reached the stage where only the stable $L1_2$ phase is observed. In the case of the composition $Ti_{25}Cr_8Al_{67}$, 12 h sintering was needed for the complete transformation from $D0_{22}$ to $L1_2$. In the present work, the equilibrating sintering times were 12 or 24 h at 1273 K or 1423 K (Table 1).

A summary of the stable phases determined by X-ray diffraction in the various sintered alloys is given in Table 1. The sintered $Ti_{25}Cr_8Al_{67}$, $Ti_{25}Mn_9Al_{66}$, $Ti_{25}Cu_{12.5}Al_{62.5}$, $Ti_{27}Rh_6Al_{67}$, $Ti_{25}Ag_8Al_{67}$, $Ti_{27}Pt_6Al_{67}$, and $Ti_{25}Au_9Al_{66}$ alloys were observed to be single phase $L1_2$ ternary aluminides with each third element. Similarly, the sintered $Ti_{25}Fe_8Al_{67}$, $Ti_{25}Co_8Al_{67}$, $Ti_{25}Ni_8Al_{67}$, $Ti_{25}Zn_9Al_{66}$, and $Ti_{25}Pd_8Al_{67}$ alloys are almost single phase. The dominant phase in the alloys is $L1_2$ tri-aluminide. In these alloys, except for $Ti_{25}Pd_8Al_{67}$, the minor phase is identified by X-ray powder diffraction. This indicates that these compositions deviate from the $L1_2$ single-phase compositions in these systems. In contrast, no $L1_2$ phase was formed in the sintered $Ti_{25}V_8Al_{67}$, $Ti_{25}Nb_8Al_{67}$, and $Ti_{25}Mo_8Al_{67}$ alloys. In these alloys, $D0_{23}$ or $D0_{22}$ compound and a small amount of second phase are formed.

The lattice parameters of the $L1_2$ phases obtained in the present work are also listed in Table 1. Nic *et al.*[33] have recently investigated the lattice parameters of $L1_2$-type ternary titanium aluminides containing Cr, Mn, Fe, Co, Ni, Cu, or Zn, and found that the lattice parameter of the $L1_2$ phase systematically decreases with increasing atomic number of alloying third element. Winnicka and Varin[31] showed that the ternary $L1_2$ compound containing Cr or Mn has a greater lattice parameter than that containing Fe or Cu. Our results (Table 1) basically confirmed the finding of Nic *et al.*: as the atomic number of the alloying third element varies from 24(Cr) to 29(Cu), except for 27(Co), the lattice parameter decreases. However, in the ternary $L1_2$ compounds containing fifth- and sixth-period elements such as Rh, Pd, Ag, Pt, and Au, their lattice parameter does not depend in a systematic way on the atomic number of the alloying third element.

Figure 2(a) shows the isothermal section of the Al–Ti–Cr equilibrium phase diagram at 1273 K which was estimated based on the results of the present study. This isothermal section unambiguously shows that an $L1_2$ phase field exists in the Al–Ti–Cr system. However, the phase field is very narrow, with about a 1 at.% radius and its center at $Ti_{25}Cr_8Al_{67}$. Besides the $L1_2$ phase, the pertinent phases have been also identified using several single-phase, two-phase, and three-phase alloys. They are TiAl($L1_0$-type), $TiAl_2$(tetragonal, $HfGa_2$-type), Al_3Ti($D0_{22}$-type), $Al_{17}Cr_9$(hexagonal-type), and Cr_2Al($C11_b$-type). Of these intermetallic compound phases, $TiAl_2$ phase has been found to exist in the authors' previous work.[34] The presence of $Al_{17}Cr_9$ phase has been reported by Lindahl *et al.*[35] It has been confirmed that the phase corresponding to the composition Cr_2Al, which is expected from the Al–Cr binary phase diagram,[36] becomes disordered at temperatures higher than its transformation point (1184 K).

Figure 2(b) shows the isothermal section at 1273 K of the Al–Ti–Mn system. The $L1_2$ phase field in this system closely resembles that of the Al–Ti–Cr system. However, the center composition of the $L1_2$ phase field is shifted a little toward a higher content of alloying third element compared with the Al–Ti–Cr system; the center appears to be at $Ti_{25}Mn_9Al_{66}$. In this system, it is noted that the pertinent phases are Al_8Mn_5 (hexagonal-type), TiAlMn(C14-type, Laves phase) and three compound phases in the Al–Ti binary system. The Al_8Mn_5 phase has been found in the Al–Ti–Mn system also by Meissner and Schubert.[37]

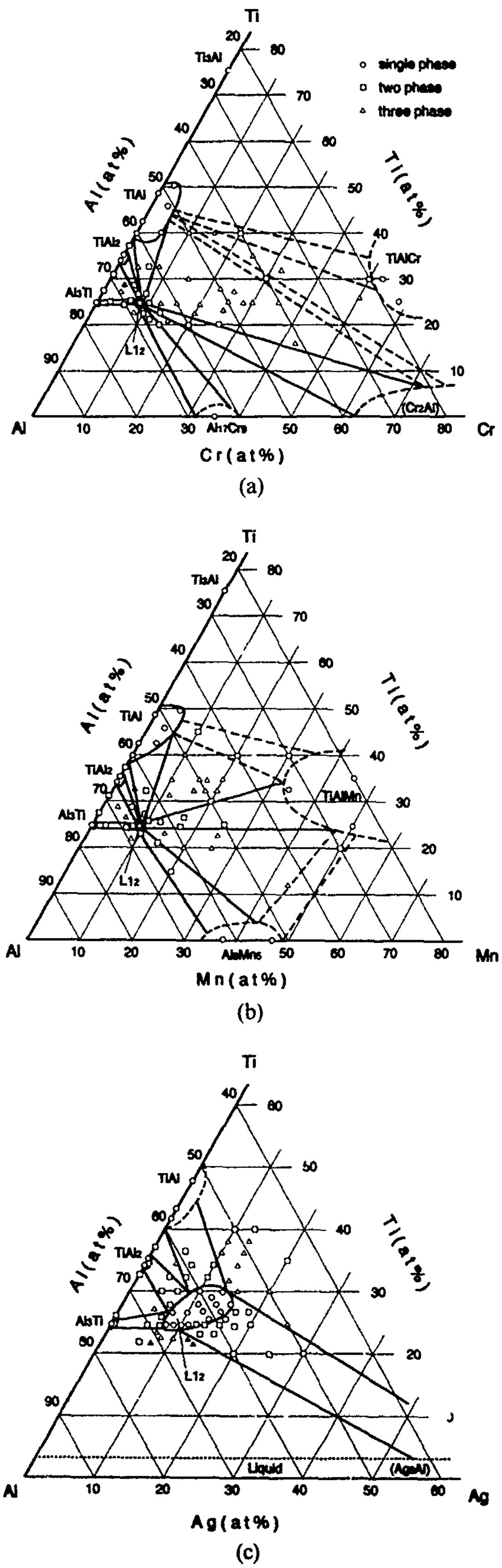

(a)

(b)

(c)

Fig. 2. Al-rich corner of the isothermal section at 1273 K of the (a) Al–Ti–Cr, (b) Al–Ti–Mn, and (c) Al–Ti–Ag systems. Solid lines are phase boundaries determined in this work. Broken lines are speculative phase boundaries. ○, □, and Δ represent single-phase, two-phase and three-phase regions, respectively.

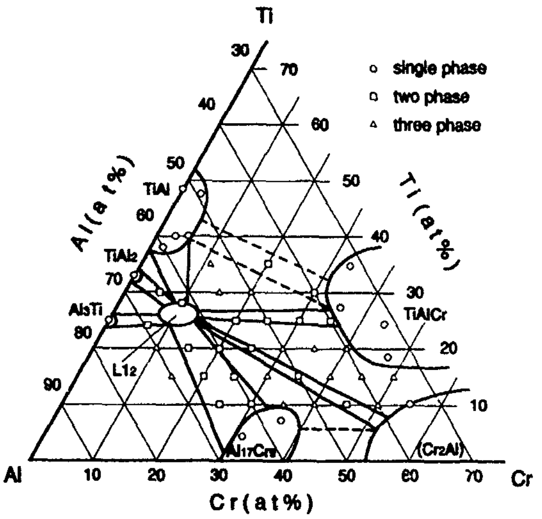

Fig. 3. Al-rich corner of the isothermal section at 1423K of the Al–Ti–Cr system. Solid lines are phase boundaries determined from this work. Broken lines are speculative phase boundaries. ○, □, and Δ represent single-phase, two-phase, and three-phase regions, respectively.

Figure 2(c) is the isothermal section at 1273 k of the Al–Ti–Ag equilibrium diagram. In this case, the extent of the $L1_2$ phase field is much larger than those in Al–Ti–Cr and Al–Ti–Mn systems. The oval-shaped $L1_2$ phase field can be given as $Ti_xAg_yAl_{100-x-y}$, where (approximately) $x = 25$–30 and $y = 8$–15 at.%, which is about the same as that previously published for the Al–Ti–Cu system.[10] A pertinent phase, Ag_2Al (liquid at 1273 K), was identified using several two-phase alloys. This phase, which is expected from the Al–Ag binary phase diagram,[36] has a disordered hcp-type structure at temperatures lower than its melting point (999 K).

Figure 3 shows the Al-rich corner of the isothermal section at 1423 K of the Al–Ti–Cr system. At this temperature, the extent of the $L1_2$ phase field clearly increases toward higher content of Cr and Ti. Thus, this observation suggests that the extent of the $L1_2$ phase field increases with increasing temperature, as previously pointed out by Mazdiyasni *et al.*[10] The extent of the pertinent phase fields, other than Al_3Ti, Al_2Ti, and TiAl, also increases with increasing temperature. The isothermal section at 1423 K shown in Fig. 3 is generally in good agreement with the 1473 K section reported recently by Nic *et al.*[28]

Figure 4 represents the extent of the $L1_2$-single phase field at 1423 K in the Al–Ti–X (X = Co, Rh, Pt, Pd, and Au) systems. The $L1_2$ phase field in the ternary systems containing Co, Rh, and Pt are much the same in extent. The composition of the center of the $L1_2$ phase field in these ternary systems can be given as $Ti_{27}X_6Al_{67}$ (X = Co, Rh, and Pt) which is similar to that for Al–Ti–Ni and

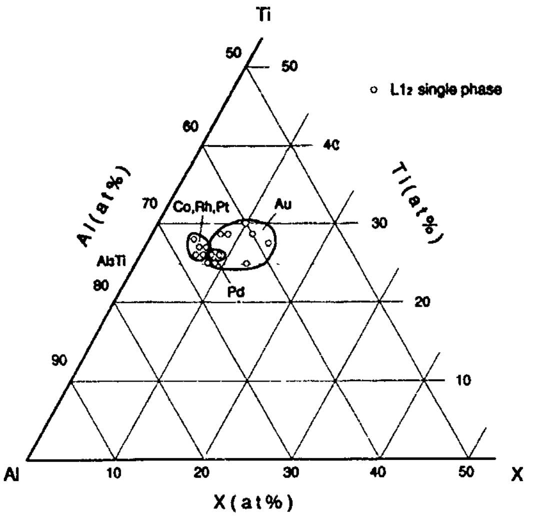

Fig. 4. The extent of the $L1_2$ phase field in the isothermal section at 1423 K of the Al–Ti–X (X= Co, Rh, Pd, Pt, and Au) systems.

Al–Ti–Fe systems by Mazdiyasni *et al.*[10] In the case of the Al–Ti–Pd system, the center appears to be at $Ti_{26}Pd_9Al_{65}$. In the Al–Ti–Au system, it is found that the extent of the $L1_2$ phase field is quite similar to that of Al–Ti–Ag and Al–Ti–Cu systems. Thus, the composition of the $L1_2$ phase in the ternary systems is similar for alloying third elements in the same group of the periodic table.

3.2 Examinations of arc-melted alloys

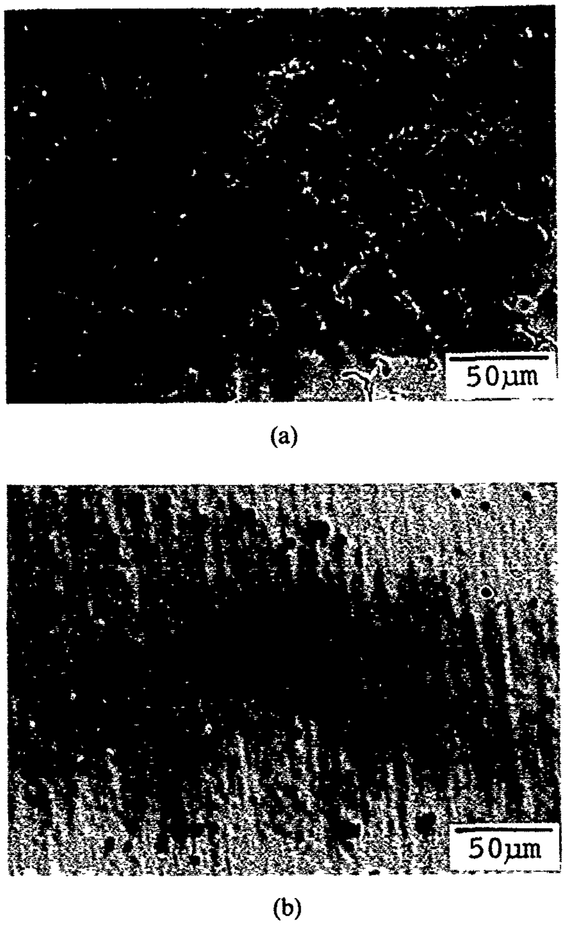

Fig. 5. Optical micrographs of (a) as-cast and (b) homogenized $Ti_{25}Cr_8Al_{67}$ alloy.

Figure 5 shows typical microstructures of an arc-melted alloy with a composition of $Ti_{25}Cr_8Al_{67}$. As shown in Fig. 5(a), the as-cast alloy contains a substantial volume fraction of second phases in the interdendritic regions. Pores that result from solidification shrinkage are also detected, although the pore volume fraction is small Most of the second phases disappear during homogenization treatment at 1423 K for 48 h (Fig. 5(b)), resulting in a nearly single phase structure. However, a large number of pores are observed. As they appear to form in place of solutionizing second phases, it is generally assumed that a Kirkendall mechanism is responsible for the formation of pores during homogenization treatment.[38]

Table 2. The second phases identified by XRD analysis and the volume fractions of second phases and porosity in the as-cast and homogenized alloys

Alloy	Second phase and porosity	
	As-cast	Homogenized
$Ti_{25}Cr_8Al_{67}$	$Al_{17}Cr_9$ (~3%) Porosity (~1%)	No second phase Porosity (~2%)
$Ti_{25}Mn_9Al_{66}$	Al_8Mn_5 (~15%) Porosity (~1%)	Nearly no second phase Porosity (~5%)
$Ti_{25}Ni_8Al_{67}$	Al_3Ni_2,Ti_5Al_{11} (~10%) Porosity (~1%)	Al_2TiNi, Al_3Ti (~5%) Porosity (~5%)
$Ti_{25}Cu_{12\ 5}Al_{62\ 5}$	$CuAl_2$ (~5%) Porosity (~1%)	Nearly no second phase Porosity (~4%)
$Ti_{25}Ag_8Al_{67}$	Ag_2Al (~20%) Porosity (~2%)	No second phase Porosity (~10%)

The second phases observed by X-ray diffraction and their volume fractions and porosities of various arc-melted alloys are summarized in Table 2. The volume fraction of the second phase was estimated from SEM micrographs, and porosity was calculated from density, which was determined by weight and dimensional measurements. X-ray diffraction, of course, verified that all five alloys had the $L1_2$ structure. However, as shown in Table 2, all as-cast materials contain an extensive amount of second phases, although the volume fraction of second phases depends on alloy system. The porosity increase after homogenization is approximately proportional to the volume fraction of second phases in the as-cast condition. The second phase in the as-cast alloys were identified by X-ray diffraction. They are $Al_{17}Cr_9$, Al_8Mn_5, Al_3Ni_2, $CuAl_2$ and Ag_2Al. In the

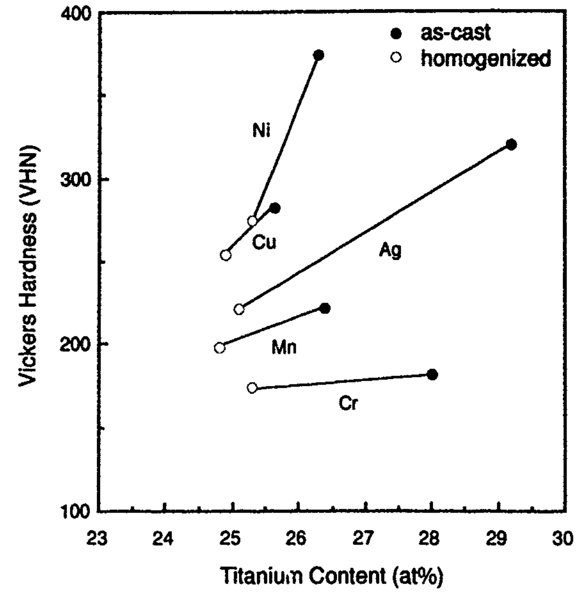

Fig. 6. Vickers microhardness (25 g load) as a function of titanium content of the $L1_2$ phases in the as-cast and homogenized alloys containing Cr, Mn, Ag, Cu, and Ni.

$Ti_{25}Ni_8Al_{67}$ alloy, the Ti_5Al_{11} ($D0_{23}$-type) phase was present and did not disappear after homogenization but changed to Al_3Ti($D0_{22}$-type) and Al_2NiTi (fcc, $Mn_{23}Th_6$-type[39]) phases.

The average compositions of $L1_2$ matrix phases in as-cast and homogenized alloys are shown in Table 3. The matrix phase in almost all the alloys is enriched with Ti and depleted of the corresponding third alloying element (X), probably because the Al–X binary phases are preferentially formed in the solidification. This indicates that the alloys in Table 3 do not solidify congruently.

Table 3. Composition of the $L1_2$ matrix phases in the as-cast and homogenized alloys

Alloy	Element	Composition (at.%) on $L1_2$ phase	
		As-cast	Homogenized
$Ti_{25}Cr_8Al_{67}$	Ti	28·0	25·3
	Al	65·7	66·7
	Cr	6·3	8·0
$Ti_{25}Mn_9Al_{66}$	Ti	26·4	24·8
	Al	65·7	66·2
	Mn	7·9	9·0
$Ti_{25}Ni_8Al_{67}$	Ti	26·3	25·2
	Al	67·4	67·2
	Ni	6·3	7·6
$Ti_{25}Cu_{12\cdot5}Al_{62\cdot5}$	Ti	25·7	24·9
	Al	61·3	61·5
	Cu	13·0	13·6
$Ti_{25}Ag_8Al_{67}$	Ti	29·2	25·1
	Al	66·2	66·5
	Ag	4·6	8·4

Table 4. Compositions of the second phase in the as-cast and homogenized $Ti_{25}Cr_xAl_{75-x}$(x = 8, 13, and 16 at.%) alloys

Alloy	Element	Composition (at.%) on second phase	
		As-cast	Homogenized
$Ti_{25}Cr_8Al_{67}$	Ti	3·3	
	Al	64·2	No second phase
	Cr	32·5	
$Ti_{25}Cr_{13}Al_{62}$	Ti	10·0	
	Al	44·2	No second phase
	Cr	45·8	
$Ti_{25}Cr_{16}Al_{59}$	Ti	14·4	15·8
	Al	35·7	38·5
	Cr	49·9	45·7

After homogenization, the composition of the matrix phase becomes close to the target composition for each ternary alloy.

Figure 6 shows the results of Vickers microhardness tests for the as-cast and homogenized specimens as a function of the Ti content of the $L1_2$ matrix phases. These ternary compounds have a significantly reduced microhardness. The lowest hardness, about 170 VHN was observed for the ternary $L1_2$ phase containing Cr. These ternary $L1_2$ phases give increasing hardness in the order Cr, Mn, Ag, Cu, and Ni. In addition, the hardness of each ternary $L1_2$ compound can be increased by increasing its Ti content, although the amount of hardness increment depends on alloy system. Similarly, Winnicka and Varin[40] have recently pointed out that Vickers hardness increases almost linearly with increasing Ti content in both as-cast and homogenized alloys.

As mentioned above and indicated in Table 2 and Fig. 6, the best microstructure and minimum microhardness were obtained for the ternary $L1_2$ compounds containing Cr. Subsequently, the influence of Cr content on their microstructure and mechanical properties were investigated. Figure 7 shows SEM microstructures of the as-cast and homogenized (at 1423 K for 48 h) specimens of alloys with compositions $Ti_{25}Cr_{13}Al_{62}$ and $Ti_{25}Cr_{16}Al_{59}$. As in the case of $Ti_{25}Cr_8Al_{67}$ (Fig. 5), as-cast materials of both alloys contain an extensive volume fraction (about 5% in both) of second phases in the interdendritic regions (Figs 7(a) and (c)). However, interestingly, both alloys show a near absence of porosity after homogenization (Figs 7(b) and (d)). In order to understand better the formation behavior of pores, the composition of the second phase in these alloys was measured by EDX analysis. The results are shown in Table 4 together with the composition of the second

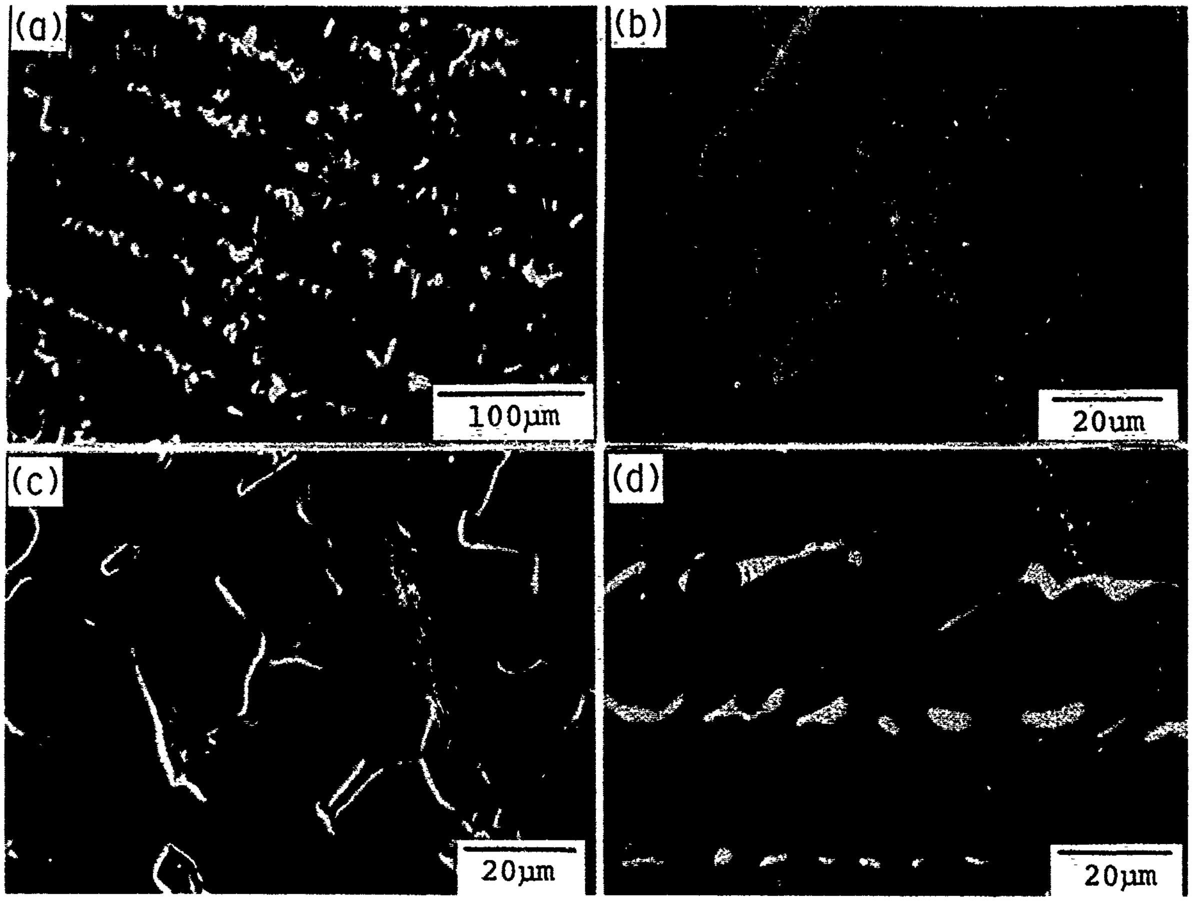

Fig. 7. SEM microstructures of the as-cast and homogenized $Ti_{25}Cr_{13}Al_{62}$ ((a) and (b)) and $Ti_{25}Cr_{16}Al_{59}$ ((c) and (d)) alloys.

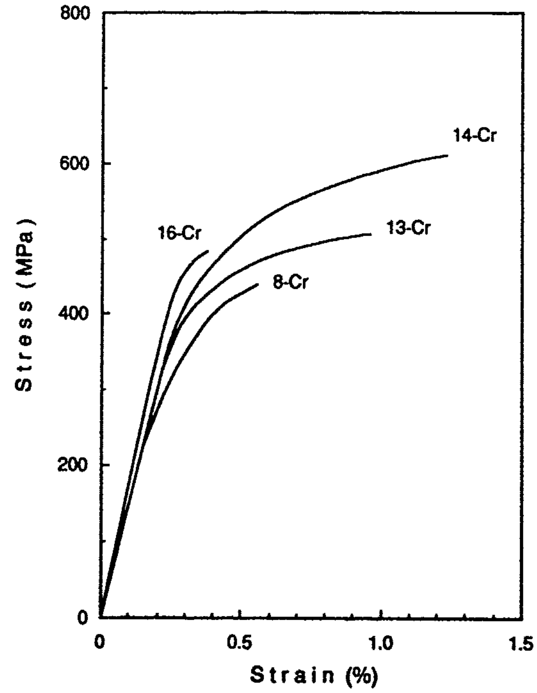

Fig. 8. The effect of Cr content on the bend stress–strain curves for the homogenized $Ti_{25}Cr_xAl_{75-x}$ (x = 8, 13, 14, and 16 at.%) alloys.

phase in the $Ti_{25}Cr_8Al_{67}$ alloy in which an extensive amount of pores are formed after homogenization. The second phase in alloy $Ti_{25}Cr_8Al_{67}$ is the $Al_{17}Cr_9$ phase. However, in alloy $Ti_{25}Cr_{13}Al_{62}$, the composition of the second phase corresponds to that for the Cr_2Al phase, which is expected from the observed Al–Ti–Cr phase diagram (Fig. 2(a) or Fig. 3). Similarly, in alloy $Ti_{25}Cr_{16}Al_{59}$, the composition of the second phase in both as-cast and homogenized materials is close to that for the TiAlCr phase. It seems, therefore, that the formation of pores during homogenization treatment is closely associated with the second phase formed during homogenization. However, the reasons why pores are formed when $Al_{17}Cr_9$ is formed and they are not when Cr_2Al or TiAlCr is formed are not yet clear.

Finally, Fig. 8 shows the results of bend tests at ambient temperature for four homogenized $Ti_{25}Cr_xAl_{75-x}$ (x = 8, 13, 14, and 16 at.%) alloys. Strain was measured with a strain gage glued to the tension side of the specimens. As shown in Fig. 8, these $L1_2$ compounds have some intrinsic ductility at ambient temperature: about 0·25% for the $Ti_{25}Cr_8Al_{67}$ alloy, which can be increased to about 0·9% by increasing the Cr content, except for $Ti_{25}Cr_{16}Al_{59}$ with two-phase structure. Thus, the single-phase $Ti_{25}Cr_{14}Al_{61}$ with the highest Cr content shows the maximum bend ductility. Interestingly, in this alloy no pores were observed, although a slight amount of second phase was observed. We may thus conclude that the bend ductility of the ternary $L1_2$ compounds at ambient temperature increases when porosity is reduced.

4 CONCLUSIONS

Ternary intermetallic compounds in various Al–Ti–X systems were formed using elemental powders and powder metallurgy processing. It was confirmed that the $L1_2$ compounds are formed in Al_3Ti-base alloys containing Cr, Mn, Fe, Co, Ni, Cu, Zn, Rh, Pd, Ag, Pt, and Au. However, no ternary $L1_2$ compound was observed in the ternary alloys with alloying third elements such as V, Nb, and Mo. In some ternary systems, the extent of the $L1_2$ phase fields and the surrounding equilibrium phases at 1273 K or 1423 K were determined. The composition of the $L1_2$ phase is altered significantly by the alloying third element. There is a general trend that the composition is similar when the alloying third element is in the same group of the periodic table.

In the arc-melted, and the as-cast conditions, the alloys investigated contain a substantial volume fraction of second phases. Homogenization results in the increase in porosity, but the second phases are mostly eliminated. In general, the porosity is approximately proportional to the amount of second phases existing in the as-cast condition. However, this behavior was not observed in higher Cr content alloys. For the $Ti_{25}Cr_{14}Al_{61}$ alloy, no porosity was observed after homogenization and ambient temperature ductility up to 0·9% was achieved in bending.

ACKNOWLEDGEMENTS

This work was supported in part by a Grant-in-Aid for Scientific Research on the priority area 'Intermetallic Compounds as New High-Temperature Structure Materials' from the Japanese Ministry of Education, Science and Culture. The authors would like to thank Dr H. Tsuda for his useful advice and discussions. In addition, the authors are very grateful for the experimental assistance of Mr A. Kito.

REFERENCES

1. Yamaguchi, M., Umakoshi, Y. & Yamane, T., *Phil. Mag.*, **55A** (1987) 301.
2. Raman, A. & Schubert, K., *Z. Metallk.*, **56** (1965) 40.
3. Raman, A. & Schubert, K., *Z. Metallk.*, **56** (1965) 99.
4. Virdis, P. & Zwicker, U., *Z. Metallk.*, **62** (1971) 46.
5. Seibold, A., *Z. Metallk.*, **72**, (1981) 712.
6. Kumar, K. S. & Pickens, J. R., *Scripta Metall.*, **22** (1988) 1015.
7. Huang, S. C., Hall, E. L. & Gigliotti, M. F. X., *J. Mater. Res.*, **3**(1) (1988) 1.
8. Tarnacki, J. & Kim, Y-W., *Scripta Metall.*, **22** (1988) 329.
9. George, E. P., Porter, W. D., Henson, H. M., Oliver, W. C. & Oliver, B. F., *J. Mater. Res.*, **4**(1) (1989) 78.
10. Mazdiyasni, S., Miracle, D. B., Dimiduk, D. M., Mendiratta, M. G. & Subramanian, P. R., *Scripta Metall.*, **23** (1989) 327.
11. Powers, W. O., Wert, J. A. & Turner, C. D., *Phil. Mag.*, **60A** (1989) 227.
12. Powers, W. O. & Wert, J. A., *Phil. Mag.*, **60A** (1989) 585.
13. Turner, C. D., Powers, W. O. & Wert, J. A., *Acta Metall.*, **37** (1989) 2635.
14. Mysko, D. D., Lumsden, J. B., Powers, W. O. & Wert, J. A., *Scripta Metall.*, **23** (1989) 1827.
15. Winnicka, M. B. & Varin, R. A., *Scripta Metall.*, **23** (1989) 1199.
16. Winnicka, M. B. & Varin, R. A., *Scripta Metall. Mater.*, **24** (1990) 57.
17. Zhang, S., Nic, J. P. & Mikkola, D. E., *Scripta Metall. Mater.*, **24** (1990) 57.
18. Mabuchi, H., Hirukawa, K. & Nakayama, Y., *Scripta Metall.*, **23** (1989) 1761.
19. Mabuchi, H., Hirukawa, K., Tsuda, H. & Nakayama, Y., *Scripta Metall. Mater.*, **24** (1990) 505.
20. Mabuchi, H., Hirukawa, K., Katayama, K., Tsuda, H. & Nakayama, Y., *Scripta Metall Mater.*, **24** (1990) 1553.
21. Powers, W. O. & Wert, J. A., *Metall. Trans.*, **21A** (1990) 145.
22. Kumar, K. S. & Brown, S. A., *Phil. Mag.*, **65A** (1992) 91.
23. Inui, H., Luzzi, D. E., Porter, W. D., Pope, D. P., Vitek, V. & Yamaguchi, M., *Phil. Mag.*, **56A** (1992) 245.
24. Kumar, K. S. & Brown, S. A., *Acta Metall. Mater.*, **40** (1992) 1923.
25. Morris, D. G. & Gunter, S., *Acta Metall. Mater.*, **40** (1992) 3065.
26. Durlu, N. & Inal, O. T., *Mater. Sci. Eng. A*, **152** (1992) 67.
27. Schneibel, J. H., Horton, J. A. & Porter, W. D., *Mater. Sci. Eng. A*, **152** (1992) 126.
28. Nic, J. P., Klansky, J. L. & Mikkola, D. E., *Mater. Sci Eng A*, **152** (1992) 132.
29. Chen, X., Chen, S., Wu, X., Fang, L. & Hu, G., *Mater. Sci. Eng. A*, **153**, (1992) 370.
30. George, E. P., Pope, D. P., Fu, C. L. & Schneibel, J. H., *ISIJ Int.*, **31** (1991) 1063.
31. Winnicka, M. B. & Varin, R. A., *Metall. Trans.*, **23A** (1992) 2963.
32. van Loo, F. J. J. & Rieck, G. D., *Acta Metall.*, **21** (1973) 61.
33. Nic, J. P., Zhang, S. & Mikkola, D. E., *Script Metall. Mater.*, **24** (1990) 1099.
34. Mabuchi, H., Asai, T. & Nakayama, Y., *Scripta Metall.*, **23** (1989) 685.
35. Lindahl, T., Pilotti, A. & Westman, S. *Acta Chem. Scand.*, **22** (1968) 748.
36. McAlister, A. J., *Binary Alloy Phase Diagrams*, ed. T. B. Massalski. Am. Soc. Metals, Metals Park, Ohio, 1986.
37. Meissner, H-G. & Schubert, K., *Z. Metallk.*, **56** (1965) 523.
38. Mysko, D. D., Lumsden, J. B., Powers, W. O. & Wert, J. A., *Scripta Metall.*, **23** (1989) 1827.
39. Florio, J. V., Rundie, R. E. & Snow, A. I., *Acta Cryst.*, **5** (1952) 449.
40. Winnicka, M. B. & Varin, R. A., *Scripta Metall. Mater.*, **25** (1991) 2297.

Intermetallics 1 (1993) 49–58

Strengthening mechanisms in cubic titanium trialuminide alloys

D. G. Morris, S. Günther & J. C. Joye

Institute of Structural Metallurgy, University of Neuchâtel, 2000 Neuchâtel, Switzerland

(Received 2 December 1992; accepted 22 December 1992)

Titanium trialuminide alloys stabilised to the cubic crystal structure show strength variations with temperature that vary from one alloy to another. For some alloys significant strength increases are seen at low temperatures, while for other alloys such strengthening may occur at high temperatures. These strength increases are not explained by dislocation core structures or cross-slip processes but by solute effects or by fine Al_2Ti precipitate particles present in the material or formed during testing. Analysis of dislocation mobility at low temperatures by measurements of activation volume suggests that mobility at very low temperatures is controlled by a mechanism of unblocking and blocking of dislocation segments through Peierls valleys, probably influenced by solute additions.

Key words: trialuminides, titanium trialuminides, strengthening mechanisms, activation volumes, dislocation mobility

INTRODUCTION

The yield or flow stress of titanium trialuminide alloys stabilised to the cubic crystal structure by the substitution of some of the aluminium by transition metals, such as Fe, Mn or Cu, has been reported on many occasions, for example Refs 1–6. The most important features of the strength variations with temperature observed are the following: (i) a weak stress anomaly (increase in strength with temperature above the variation expected from changes in elastic moduli) at high test temperatures, typically about 500–600°C[1-4] which is sometimes detected as a strength peak, sometimes as a strength plateau on the decreasing stress–temperature slope, or again, not clearly distinguished; (ii) a significant flow stress increase on testing at low temperatures (77 K and below);[3,6] (iii) significant variations from one alloy system to another and between results reported on the same system by various workers.[1-4,7] These results have been interpreted in various ways, for example: (i) the operation of cube cross-slip processes at high temperatures, leading to Kear–Wilsdorf locks causing a strength increase;[4] (ii) superdislocation dissociation into a pair of super Shockley partials separated by a superlattice intrinsic stacking fault (SISF). These partial dislocations are known to have non-planar cores, as in the Pt_3Al and Co_3Ti intermetallics,[8-17] and lead to significant strengthening at low temperatures; (iii) different bond strengths between the atoms in the cubic trialuminide according to the choice of ternary element,[7] or depending on the Ti content of the particular alloy considered.[18] The validity of the second hypothesis depends of course on the dissociation of dislocations in this way, which is by no means certain since there is considerable discrepancy in the literature,[19] with some reports of dissociation creating SISF,[20,21] and other reports of dissociation creating antiphase domain boundaries (APB).[4,22-24]

The present work sets out to examine the extent and origins of strengthening in a series of cubic trialuminides containing different ternary additions and different amounts of titanium. At the same time, the strengthening observed is related to the tendency to formation of Al_2Ti precipitation in these materials.[25] Measurements of activation volume have also been carried out in an attempt to learn more about the processes controlling deformation.

Intermetallics 0966-9795/93/$6.00 © 1993 Elsevier Science Publishers Ltd, England. Printed in Great Britain

EXPERIMENTAL

The alloys used for the present study were prepared by spray deposition of kilogram quantities of pre-alloyed melts. Details of deposition and the hot isostatic pressing (HIP) treatments used to remove traces of porosity in the deposited billets have been described in Refs 4 and 25. The chemical compositions determined on these deposited and HIP-treated billets are given in Table 1. Shown in this table are the compositions of materials for which no clear precipitation was detected in this starting state. Other alloys have been examined during the course of this work (Al–Ti–Fe(II) and Al–Ti–Cu) for which precipitation had already occurred during deposition or HIP treatment;[25] these are not considered here. X-ray diffraction confirmed that in each case the material had the $L1_2$ ordered crystal structure. Cylindrical samples of diameter 3 mm and length 6 mm for compression testing were cut by spark machining and were tested at a strain rate of 2×10^{-4}/s in specially constructed grips installed on 10 kN and 100 kN capacity Schenck Universal testing machines. Tests at temperatures above ambient temperature were carried out under an argon atmosphere and tests at low temperature with the sample held within a suitable liquid maintained at the desired temperature. Heating was carried out in a fast-response image furnace which required typically 30 minutes to reach temperature and to stabilise the temperature of the testing assembly. Following straining to the desired strain, furnace heating was stopped with the sample still under load, and the split furnace was removed. In both cases of high- and low-temperature testing, extensometer rods fixed close to the sample ends allowed precise measurements of sample defor-mation.

For all the tests, there was considerable plastic deformation before failure. For test temperatures below about 500°C, failure generally occurred at the maximum stress following the gradual accumulation of internal longitudinal cracks. At the highest temperatures the sample often did not fail and tests were interrupted after a strain of about 25%, since at this point the extension measuring system was incapable of measuring further. While there was a general trend to increased failure ductility at higher temperatures,[4] in view of the complex nature of the failure process no analysis of maximum stress and failure ducility is made here.

Table 1. Analysed composition of alloys (atomic %)

Alloy designation	Aluminium content	Titanium content	Ternary addition
Cr(I)	65·0	26·9	8·1 Cr
Cr(II)	64·5	27·5	8·0 Cr
Fe(I)	64·0	28·0	8·0 Fe
Fe(III)	66·5	25·5	8·0 Fe
Mn	66·7	25·7	7·6 Mn

Measurements of activation volume were made based on the analysis of changes in flow stress as the imposed strain rate was changed abruptly to a higher or lower value. The strain rate jumps used were by a factor of 3 or 10, and were carried out at intervals throughout the entire straining period: a typical cycle involved a strain rate increase ×3, followed by a strain rate decrease ×3, followed by a strain rate increase ×10, followed by a strain rate decrease ×10, followed finally by a period at the initial strain rate to restabilise the dislocation structure. Within the range of scatter of data each of these strain rate jumps gave essentially the same deduced activation volume, although on some occasions the final strain rate decrease (by 10) led to unusually high values for activation volume, for unexplained reasons. It has been shown[4,26] that the trialuminide alloys can show dynamic strain-ageing over an intermediate temperature range, for example from 300°C to 600°C, and for such test conditions an apparent negative activation volume is obtained as dislocation breakaway from pinning obstacles occurs and a lower flow stress results from increasing the imposed strain rate. Such ageing effects will be discussed in a later publication.[27] The activation volume was deduced on the basis of the standard equation for thermally activated flow:

$$\dot{\varepsilon} = A \exp \{(-Q + \tau V)/kT\} \quad (1)$$

where $\dot{\varepsilon}$ is the strain rate, A is a constant, Q is the activation energy and V the activation volume for the critical dislocation unlocking mechanism, and τ is the applied shear stress. k is the Boltzmann constant and T the test temperature. The activation volume can be deduced form the change in strain rate and the change in measured flow stress ($\Delta\sigma$) as

$$V=3kT \{\Delta \ln \dot{\varepsilon}/\Delta\sigma\} \quad (2)$$

Here the change in shear stress, $\Delta\tau$ is taken to be 1/3 the change in applied stress $\Delta\sigma$, that is, a Taylor factor of 3 was assumed. No other corrections, to take account of machine elasticity, for example, were made.

Following mechanical testing, samples of selected materials were examined by transmission electron microscopy to identify dislocation characteristics and the extent and form of any precipitation. Preparation techniques and equipment have been described in Refs 4 and 25.

RESULTS

Strength variations with temperature

The variation of flow stress with test temperature for all the alloys tested here is shown in Fig. 1. It may be seen that two essential types of flow stress variation are found. For the first, there is a certain increase in flow stress at low temperatures as the test temperature is decreased below about room temperature, with a more gentle flow stress decrease as the test temperature is raised above room temperature—examples of this are the Al–Ti–Fe(III), Al–Ti–Mn and Al–Ti–Cr(I) alloys. For other materials, represented here by the Al–Ti–Cr(II) and Al–Ti–Fe(I) alloys, there is a similar increase in flow stress below room temperature, but at test temperatures above about 350°C the flow stress shows a considerable anomalous increase.

The different flow stress variations found may be related to the Ti content of the alloy, as illustrated in Fig. 2. For the alloys examined the yield or flow stress always increases with the Ti level, for any given temperature. The room temperature flow stress level shows a steady increase with the Ti level from the lowest value 25·5% (atomic) up to the highest value (28%). At the highest temperature studied here, 700°C, the behaviour is different, the flow stress increasing gradually with Ti content over the range 25·5–27%, but then showing a dramatic increase as the Ti level increases further, to flow stresses higher than those measured at room temperature; this is in fact a consequence of the anomalous strength increase shown by the high-Ti alloys. The variation observed at 500°C is intermediate between that at room temperature and at 700°C, with a mild stress anomaly visible.

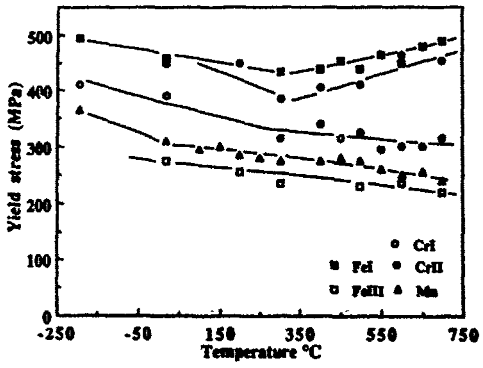

Fig. 1. Yield stress variation with test temperature for the titanium trialuminides examined.

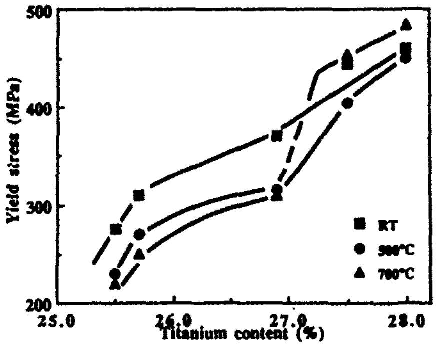

Fig. 2. Yield stress variation with Ti content for the trialuminides examined, for three test temperatures.

Microstructural variations

Examination of the materials tested here shows no evidence of precipitation of second phases detectable by TEM before testing. This is in contrast with alloys such as Al–Ti–Fe(II) containing 29% Ti and 8% Fe, where both coarse (μm-sized) and fine (nm-sized) needles of Al_2Ti phase are seen in the starting material. (The nomenclature is taken from earlier papers.) Figure 3 shows an example of such fine precipitation. Following deformation at room temperature or temperatures close to this, no changes in precipitation are noted, but following testing at 700°C fine precipitation becomes clear

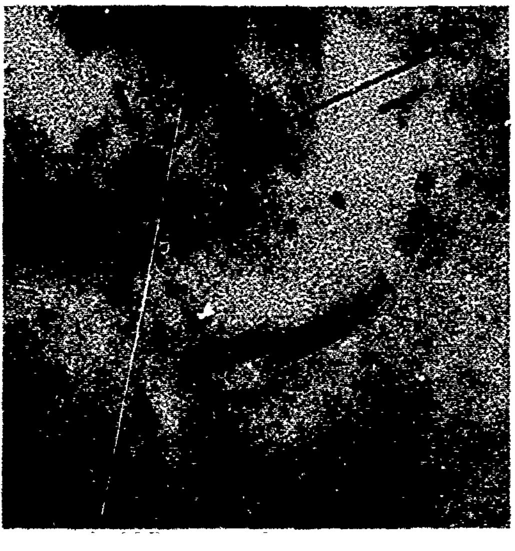

Fig. 3. High resolution electron micrograph showing fine precipitates of Al_2Ti in the Al–Ti–Fe(II) alloy in the as-prepared state, without any further heat-treatment.

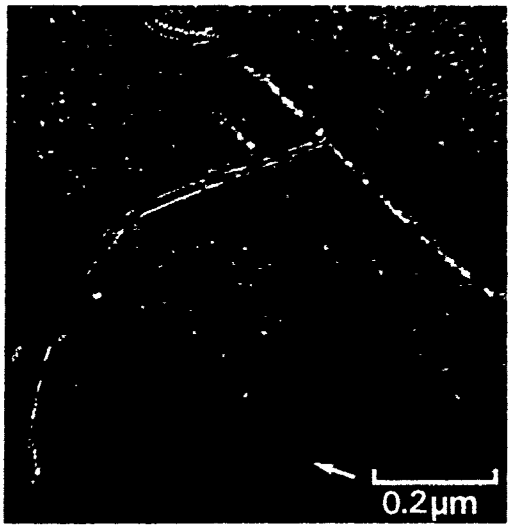

Fig. 4. Fine precipitates of Al_2Ti phase in Al–Ti–Fe(I) alloy after mechanical testing at 700°C; foil orientation (011), g vector $\bar{1}\,\bar{1}\,1$.

for the alloys showing the high-temperature stress anomaly (Al–Ti–Fe(I) and Al–Ti–Cr(II)), as illustrated in Fig. 4. For the other alloys tested there was no sign, by X-ray or electron diffraction, by bright field, dark field or by high resolution electron microscopy, of any precipitation in the matrix of these alloys after high temperature testing. Careful examination of dislocation core regions in such materials by high resolution electron microscopy, Fig. 5, was able to distinguish, however, a change in lattice plane distances which correspond to that seen at Al_2Ti precipitates (as in Fig. 3) and hence it appears that incipient precipitation was taking place. In Fig. 5, Al_2Ti precipitates of about 1–2 nm length appear to be forming at the cores of the dissociated superdislocation. It thus seems reasonable to associate the high temperature strength increases found for some alloys with the formation of precipitates at dislocations and throughout the matrix.

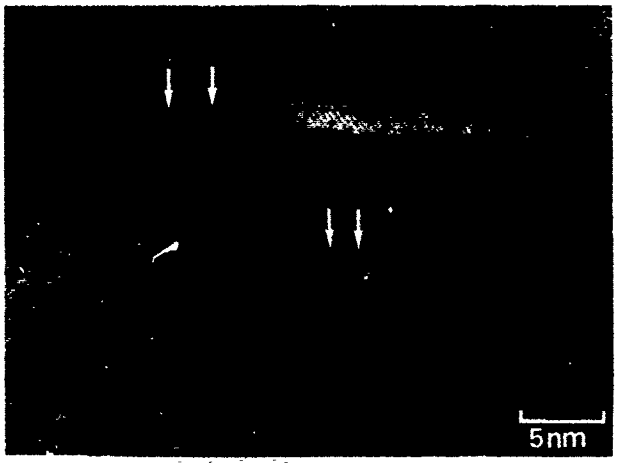

Fig. 5. High resolution electron micrograph showing fine precipitation of Al_2Ti at a superdislocation in Al–Ti–Cr(I) alloy strained to 1% at 500°C.

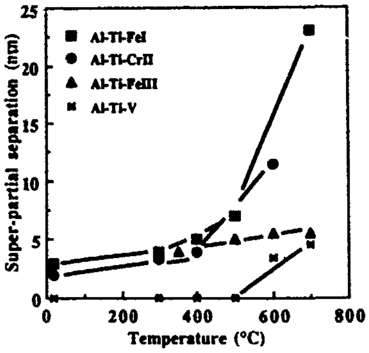

Fig. 6. Variation in separation of superpartial dislocations on annealing for 5 minutes at each temperature. Samples were initially deformed 1% at room temperature.

It has been reported earlier[4,24,28,29] that the dislocations present in trialuminide alloys tested at high temperature are dissociated into superpartial dislocations of Burgers vector 1/2⟨110⟩ separated by APB, and that the dissociation distance of these partials varies considerably with testing or annealing temperature as a result of structural relaxation of the APB, as predicted earlier by Brown for β brass.[30] Figure 6 shows the variation of superpartial separation for several alloys deformed at room temperature and then annealed for 5 minutes at various temperatures. It is evident that there are large changes in dissociation distance for all the alloys, but that the changes are much greater for the two alloys (Al–Ti–Fe(I) and Al–Ti–Cr(II)), which show the anomalous strength on testing at high temperature (Fig. 1). However, even for alloys that do not show a high temperature strength anomaly, for example Al–Ti–Fe(III), there is still a significant relaxation of APB and increase in superpartial separation on high-temperature annealing. Also included in Fig. 6 are data from an Al–Ti–V alloy, which showed no high temperature stress anomaly, and no sign of precipitation in the matrix or at the dislocations. This alloy, of composition 75% Al, 23·75% V and 1·25% Ti had the DO_{22} crystal structure and deformed at room temperature by a mixture of twinning and dislocation guide. As indicated in Fig. 6, these dislocations were in fact perfect, undissociated dislocations that remained undissociated up to temperatures of 500°C, and it was only at higher temperatures that dissociation into superdislocations took place.

After testing all the present materials (with the exception of the Al–Ti–V alloy shown in Fig. 6) at room temperature and at low temperatures (77 K), the dislocations seen were dissociated into super-

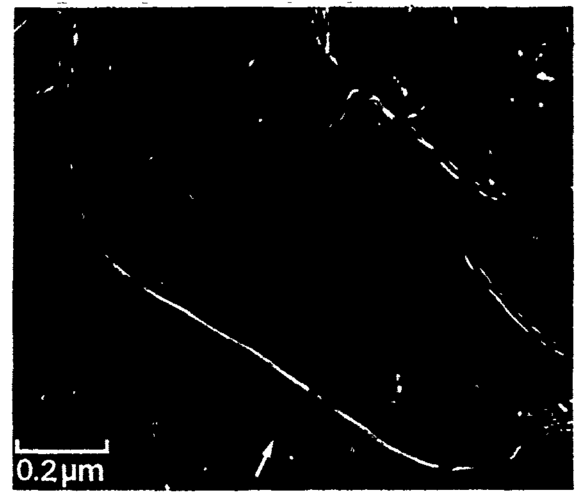

Fig. 7. Smoothly curved APB-dissociated superdislocations in Al–Ti–Mn alloy deformed 1% at 500°C. The straight dislocation segment lies on an octahedral plane, while nearly screw-oriented segments lie on cube planes; foil orientation (101), g vector $\bar{1}\,\bar{1}\,1$.

partial dislocations of type $1/2\langle 110\rangle$, that is, separated by an APB fault.[24,29] There was no sign that dislocation segments were dissociated into $1/3\langle 211\rangle$ type superpartials, that is, separated by SISF, and there is thus no justification to invoke the immobile nature of such dislocation cores to explain low-temperature stress variations. After testing at high temperatures, many superdislocations have their APB faults lying on $\{001\}$ planes.[4] It was this observation, made on the Al–Ti–Fe(I) alloy, that led to the interpretation of high-temperature strengthening in terms of cube cross-slip dislocation locking. Examination of addition materials here, for example the Al–Ti–Mn alloy, Fig. 7, shows that even for materials that do not show high-temperature strengthening, many dislocations lie on cube planes, and are clearly mobile there. It thus seems unlikely that cube cross-slip blocking mechanisms are responsible for the high-temperature strengthening observed for some of the alloys.

Activation volume measurements

Measurements of activation volume have been carried out for most of the alloys over a wide range of test temperatures and strains. Figure 8 shows results obtained on testing the Al–Ti–Fe(I) alloy at room temperature and the Al–Ti–Mn alloy at several temperatures. In all cases the activation volume measurements cover a range of strains from about 1% up to about 10%, the stress range varying according to the flow stress at these strains and temperatures. There is a certain scatter in the results for each material and condition, but it is nevertheless possible to make several deductions from the results. The scatter in data is generally randomly distributed throughout a test, but for some cases, for example the room temperature tests of both Al–Ti–Fe(I) and Al–Ti–Mn, it is the

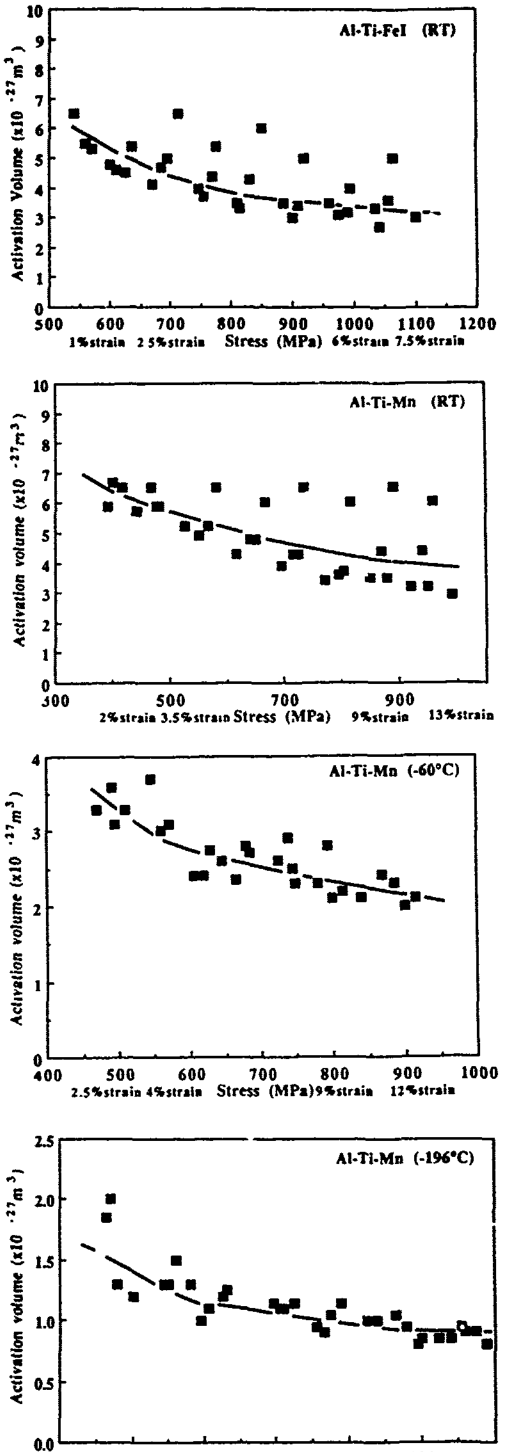

Fig. 8. Values of activation volume measured on Al–Ti–Fe(I) at room temperature and Al–Ti–Mn at temperatures ranging from room temperature to −196°C. The general flow stress over the range of measurements is shown in each case: the approximate strain is indicated at certain points.

fourth strain rate jump of a given cycle (where the strain rate is decreased by a factor of 10, see the Experimental Section) that gives different results. An important result from the data of Fig. 8 is that the activation volume changes only slightly with applied stress or strain and that it is therefore possible to define a representative value for each material and temperature. The value quoted below is typically the average over the strain range tested or the value at a strain of 5–8%. The first activation volume measurements at small strains (about 1%) were often much higher than those recorded later. Such measurements were made during the slight yield plateau shown by these materials where a steady mobile dislocation density may not yet be established and therefore these high values were not used for analysis. The observation that the activation volume varies only slowly with stress (over a range of about three) and with strain (from about 2% to more than 10%) and has a rather large value is a useful indication that certain strengthening mechanisms, for example dislocation forest interaction, are not the important strain-controlling processes.

Figure 9 summarises values of activation volume measured on three of the alloys over a wide range of temperatures. In this plot, the activation volume is expressed in units of (Burgers vector)^3, taking the value of the 1/2⟨110⟩ vector to be 0·287 nm on the basis of X-ray values of lattice parameter. Over the low-temperature range, from about 200°C to the lowest temperature used, the activation volume is generally similar for each alloy, decreasing with test temperature down to very low extrapolated values at absolute zero temperature. At temperatures in the range about 250–400°C, dislocation strain-ageing phenomena occur and the flow stress shows discontinuities with generally a decreased flow stress as the strain rate is increased. Apparent activation volumes are therefore negative and are not recorded in Fig. 9. At the higher temperatures, above 500°C, the flow stress behaviour becomes normal again and activation volume measurements are possible. The values obtained are high, generally higher for Al–Ti–Mn and Al–Ti–Cr(I) than for Al–Ti–Fe(I), showing generally a slow fall in activation volume at the highest temperatures.

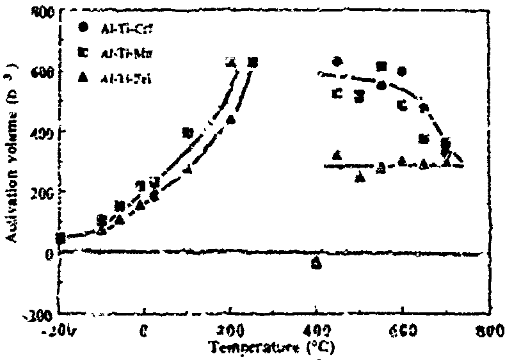

Fig. 9. Activation volume measurements on three alloys over the full temperature range where measurements were possible. Strain-ageing phenomena prohibited sensible measurements over the temperature range about 250–400°C.

DISCUSSION

High-temperature strengthening

The results shown in Figs 1 and 2 clearly relate a strength anomaly at high temperatures, that is, an increase in strength as the temperature is increased above about 300°C, to a high level of Ti and to the formation of fine Al$_3$Ti precipitates during mechanical testing. A strength increase due to the formation of Kear–Wilsdorf locks by a cube cross-slip and core-locking process, as occurs in Ni$_3$Al, is eliminated as an explanation since dislocations lying on cube planes are seen after high-temperature deformation both in alloys showing a strength anomaly (e.g. Al–Ti–Fe(I)) as well as in those that do not (e.g. Al–Ti–Mn). In addition, it should be noted that these dislocations lying on cube planes are curved and clearly mobile on these planes, not straight, locked in crystallographic directions.

On the basis of the explanation of high-temperature strengthening due to precipitation, the strength increase seen in Fig. 1 can be related to the formation of a number and size of precipitates according to the test (annealing) temperature. In effect, the test temperature is properly regarded as a 30-minute annealing temperature for age-hardening before mechanical testing. An estimate of the strengthening expected from these particles may be made on the basis of standard particle strengthening theories.[31] In the present case we need to evaluate the strengthening due to particles in the form of needles of the order 10-nm long and 1-nm thick.[25] It seems reasonable to consider that these coherent particles induce a coherency strain which is responsible for the hardening. We can then say[31] that the increased shear strength ($\Delta\tau_p$) that is needed to move a dislocation is related to the maximum force F_m that a particle can exert on an intersection dislocation, according to

$$\Delta\tau_p = F_m/bD \qquad (3)$$

where b is the Burgers vector and D the inter-particle spacing. Considering that the maximum force, F_m, is given by

$$F_m = 2L \cdot q\varepsilon R/b \qquad (4)$$

where L is the line tension, q a constant of value 1-3, ε the misfit strain, and R the particle radius, and taking as a simple approximation the line tensions to be the energy of a screw dislocation, namely about $(\mu b^2/4\pi)$ ln (D/b), where μ is the shear modulus of the matrix, it is possible to estimate the strengthening produced by this mechanism. For the Al–Ti–Fe(I) alloy tested at 700°C, the particle size R estimated from photographs such as that of Fig. 4 and from previous publications[4,25] is 0·5 nm (the thickness of the needle) and the interparticle spacing D is estimated as 20 nm. Taking the misfit strain ε to be 1% on the basis of the lattice parameters quoted for cubic Al_3Ti and binary Al_3Ti compounds (0·394 and 0·398 nm),[25,32] and a value of 80 GPa for the shear modulus,[33] the shear stress increment is deduced to be 30 MPa. Considering a Taylor factor of 3 to convert this value to an applied stress increase, we deduce a strengthening of about 90 MPa due to the particles produced by annealing/testing at 700°C. The observed strengthening anomaly is about 110 MPa, in good agreement with the theoretical value.

As a final point we may consider the variation of anomalous strengthening with temperature, analyzed previously[4] in terms of an activated strengthening process with activation energy of 63 kJ/mol, in terms of the variation of the terms in eqn (3) and (4) with temperature. The only term in these equations which shows any significant variation with temperature is the interparticle spacing D in eqn (3), since the particle radius R is maintained fixed by the particle morphology. Considering that D is given by $(N)^{-1/3}$ where N is the number of needle particles produced during the 30-minute annealing time before mechanical testing, and N can be directly related to the nucleation rate during this period, the strengthening due to precipitation will be expected to increase exponentially with the temperature according to an activation energy $Q/3$, where Q is the activation energy for nucleation. Considering that this activation energy is the same as that of diffusional transport, which is estimated to be 260–350 kJ/mol for these materials,[34] we expect strengthening to vary with temperature according to an activation energy of 90–120 kJ/mol. This value is different from that describing the experimental variation of strength. The present discussion nevertheless serves to illustrate how the precipitation strengthening hypothesis can lead to a rather similar strength variation to that seen.

It has been shown in Fig. 6 that the spacing of the superpartial dislocations increases dramatically with temperature. Such changes occur most strongly for those alloys showing a strong high-temperature stress anomaly, but are still found for other alloys where strength decreases steadily at high temperatures. The relaxation of the APB which is responsible for the spacing increase may be the cause of the load oscillations seen on the load–extension plots[4,27] at intermediate temperatures, but is apparently not directly related to the increased strength at high temperatures. The relaxation seen is greater in alloys of high Ti content where precipitation takes place at the same time as this relaxation. In such cases it may be considered that the composition of the alloy is outside that of the single-phase $L1_2$ zone at the intermediate temperatures such that solute present after the prior high-temperature treatment precipitates out. The case of the Al–Ti–V alloy is interesting because this alloy is expected to have a composition well inside the single-phase zone[35] and it is more certain that no fine precipitation occurs. Nevertheless, as seen in Fig. 6, APB relaxation still occurs for this alloy on annealing.

A further point may be noted with respect to the relaxation taking place at the APB. The fast precipitation taking place at the dislocation cores (see for example Fig. 5) will be expected to cause a reduction in the strain field around a core, which will itself lead to increased attraction between the two cores under the influence of the APB surface energy. The fact that the two partial dislocations separate implies that the APB energy decreases at the same time to an even greater extent than was *a priori* evident: for example (in Fig. 6) when the dislocation separation increases by a factor of 10, from 2·5 nm to 25 nm, the APB energy is reduced by much more than a factor of 10.

Low-temperature strengthening

The analysis of additional strengthening occurring at temperatures below ambient will be carried out here, comparing the strength at 77 K with the strength at room temperature, that is, in terms of the ratio $\sigma_{77K}/\sigma_{300K}$. For the present materials, this ratio (see Fig. 1) takes values of 1·05–1·15. The question of importance to consider is whether this strength increase is 'normal', that is completely explained by changes in elastic moduli, or whether additional strengthening mechanisms operate at the low temperatures. This question is particularly important since on some occasions[3] much greater low-temperature strengthening has been observed (for example, values of the strength ratio of 1·3–1·4) which has been explained on the basis of dislocation dissociation to immobile partials separated by SISF.[21] The model systems where dislocations dissociate into partials producing a ribbon fault are Ni_3Al, where an APB fault separates the partials, and Pt_3Al and Co_3Ti, where a SISF separates the partials. In these cases the strengthening ratio ($\sigma_{77\,K}/\sigma_{300\,K}$) is about 1 (i.e. no low-temperature strengthening) and 1·3–1·5, respectively. The present case of trialuminide alloys showing low temperature strengthening by 1·05–1·15 is intermediate and no way of distinguishing between strengthening mechanisms is obvious. Purely on the basis of changes in elastic moduli, it may be expected that low-temperature strengthening by approximately 1·1 may occur, as has been shown elsewhere.[4] In the present studies there has been no evidence of dissociation leading to the formation of SISFs, even though this type of dissociation has been reported for similar trialuminides.[20,21] Another possible cause of low temperature strengthening is solute strengthening, which is known to be more important at very low temperatures.[36] Examination of lattice site occupation of the added ternary element (Fe, Cr, Mn, etc.) shows a strong tendency to specific site filling,[25] which may suggest that the added elements are associated with anisotropic bonding or oriented elastic misfit/molulus fields, and this could lead to significant dislocation–solute interaction and strengthening at low temperatures.

Interpretation of activation volume analysis

Figure 9 shows that the activation volume determined on each alloy changes considerably over the temperature range where measurements have been made. In the very high-temperature regime it seems reasonable to associate the activation volume with cross-slip processes, in view of the extensive cross-slip found at such temperatures.[4] In such a case the activation volume can be interpreted as $V = \alpha d^2 b$,[37] where α has a value of about six and d is the separation of the Shockley partials. On the basis of the experimental results, namely an activation volume for the Al–Ti–Cr and Al–Ti–Mn alloys varying from $600b^3$ at 450°C to $300b^3$ at 700°C, and an activation volume for the Al–Ti–Fe alloy steady at about $300b^3$, we deduce spacings of the Shockley partials varying from about 2·9 nm to 2 nm. These values appear rather high, since partial dislocations separated by about 2 nm should be visible by weak-beam electron microscopy, but have not in fact been distinguished (see e.g. Refs 4, 21 and 24). This discrepancy between dissociated partial dislocations that should be distinguished separately but have not been, may imply that the measured activation volumes are overestimated. On the other hand, this discrepancy is not taken to be so important as to put seriously in doubt the measurements or the analysis.

Measurement of activation volume near and below room temperature show that this parameter decreases significantly as the temperature decreases and as the measured flow stress increases. Such results can be analyzed in terms of the Peierls mechanism controlling dislocation mobility or in terms of a locking–unlocking modification to the Peierls mechanism.[38–40] In these mechanisms a dislocation lies initially immobile in a Peierls valley, then a small segment will bulge out rapidly following unlocking from the Peierls valley; later the segment becomes relocked, leaving two superkinks that move laterally along the now advanced dislocation. The unlocking process can be described in terms of a Friedel mechanism[41] whereby the activation volume will generally be small and vary with stress according to $1/\sigma^2$. The relocking mechanism has been considered by Escaig[42] in the case of a cross-slip mechanism and normally has a very low activation volume. For the case where the relocking process is rapid the dislocation bulge will relock in the next Peierls valley beyond the original dislocation position such that the dislocation moves about one lattice plane spacing and the normal Peierls mechanism is considered to operate. If the relocking process is slow, the bulge may move over several Peierls valleys or more at one time before being relocked. Examples of such a mechanism operating in Ni_3Al have been analyzed by Caillard *et al.*[40] and in Ti crystals by Biget and Saada.[43] The analysis below is based on that of these authors.

In order to establish that a Peierls-like (or unlocking–locking) mechanism controls dislocation motions it is necessary to demonstrate that the activation volume varies with effective stress as expected ($V \propto 1/\sigma^2$) and that the value of activation volume deduced for absolute zero temperature is a reasonable value. Figure 10 shows the low-temperature data for the Al–Ti–Fe(I) and Al–Ti–Mn alloys plotted to show the reciprocal square root of the activation volume as a function

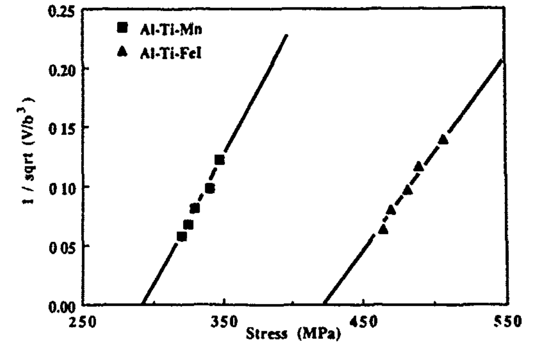

Fig. 10. Reciprocal square root of the activation volume (in units of Burgers vector cubed) as a function of applied stress of the Al–Ti–Fe(I) and Al–Ti–Mn alloys. The intercept on the stress axis permits the estimation of the internal stress.

of the applied stress. The first point to notice is the reasonable straight line relationship obtained for both alloys, confirming the correct stress dependence of the activation volume. The intercept on the stress axis gives the value of the athermal internal stress (σ_{int}) for the two alloys, namely values of about 290 MPa and 425 MPa for Al–Ti–Mn and Al–Ti–Fe(I), respectively. Secondly, we use the relationship between the effective stress, σ_{eff}, (that is $\sigma_{\mathrm{applied}} - \sigma_{\mathrm{int}}$) and the temperature in order to deduce σ_{eff} at absolute zero, and to be able to deduce $\sigma_{\mathrm{applied}}$ for imaginary tests performed at this temperature: the functional relationships between parameters lead to a linear relationship between $1/\sigma_{\mathrm{eff}}$ and the temperature,[43] and it is this that is shown in Fig. 11. From Fig. 11 we can deduce the effective stress at absolute zero (about 130 MPa for Al–Ti–Mn and 155 MPa for Al–Ti–Fe(I)) from which we deduce the applied stress at this temperature to be 415 MPa and 580 MPa for the two alloys. The evaluation carried out in this way is believed to give a more accurate value[43] than direct extrapolation of flow stress data as in Fig. 1 to absolute zero temperature. Finally, inserting these stress values back into the plots of Fig. 10, we can deduce the activation volumes corresponding to deformation at absolute zero. For Al–Ti–Mn we obtain values of about 14 ± $3b^3$ and for Al–Ti–Fe(I) we obtain values of about 16 ± $3b^3$.

The values for activation volume corresponding to absolute zero are so small that any mechanism controlling dislocation movement that takes account of interactions between forest dislocations or recombination of partial dislocation is excluded from consideration. The values are equally too high for the standard Peierls mechanism, where activation volumes of a few b^3 only are typical. Interpretation in terms of the unlocking–locking model seems reasonable, since we consider a semicircular loop of diameter 5–7b (1·5–2 nm) being formed before relocking occurs. An alternative explanation may consider that the dislocation segment mobility is determined by interactions with solute, and it is known that strong solute–dislocation interactions can control the activation volume.[44] If we consider the added ternary element (Fe or Mn) as the solute element, present in concentrations of the order 7–8%, we can probably consider that a semicircular segment will expand from a given point until the segment reaches the next solute atom, at which stage it will be stopped. The area covered during segment movement will be of the order b^3/c (where c is the solute concentration), that is about 12–14b^3, identical to the experimentally deduced value.

Dislocations examined by transmission electron microscopy show some, but rather limited, tendency to lie in well-defined crystallographic directions, as would be expected from a Peierls-type unlocking-from-atomic-valleys mechanism.[4] After testing at 77 K[24] this tendency is more marked but is still far from perfect. This observation is probably to be taken as further support for solute-controlled mechanism determining dislocation mobility.

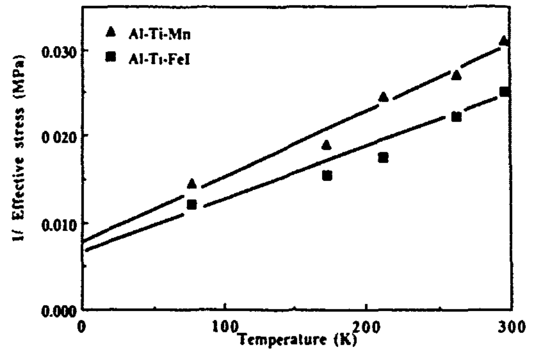

Fig. 11. Reciprocal of the effective stress applied to Al–Ti–Fe(I) and Al–Ti–Mn alloys as a function of the test temperature.

CONCLUSIONS

The variations in strength of cubic aluminium trialuminide alloys which occur between one alloy and another and as the test temperature is varied can largely be explained by solute and precipitate effects in the intermetallic matrix.

On testing at high temperatures of certain alloys, particularly those here with a high Ti content, precipitation of fine Al_2Ti particles occurs throughout the matrix and more rapidly on dislocations, leading to additional strengthening.

Dislocations cross-slip to cube planes at high temperature and glide there: this occurs for all the alloys examined, irrespective of whether the high-temperature strengthening is seen and is not believed to play an important role in determining the strength.

At low test temperatures the alloying additions in solution play a significant role in controlling the strength. There has been no evidence in the present investigations of dislocations dissociating to sessile configurations, for example by dissociating to produce SISFs. Measurements of activation volume lead to the deduction of very low activation volumes (14–16b^3) for conditions of athermal deformation. This low value may be interpreted by an unlocking–locking mechanism for dislocation movement where the flight path of the mobile segment may well be determined by the distribution of solute atoms.

ACKNOWLEDGEMENTS

We thank Mr R. Lerf for assistance with measurements of activation volume, and the Swiss National Science Foundation and Commission for Encouragement of Scientific Research for financial support of parts of this work.

REFERENCES

1. Kumar, K. & Pickens, J. R. *Scripta Metall.*, **22** (1990) 1099.
2. Zhang, S., Nic, J. P., Mulligan, W. W. & Mikkola, D. E. *Scripta metall. mater.*, **24** (1990) 1441.
3. Wu, Z. L., Pope, D. P. & Vitek, V. *Scripta metall. mater.*, **24** (1990) 2187.
4. Lerf, R. & Morris, D. G. *Acta metall. mater.*, **39** (1991) 2419.
5. Kumar, K. S. & Brown, S. A. *Phil. Mag.*, **A65** (1992) 91.
6. Kumar, K. S. & Brown, S. A. *Acta metall. mater.*, **40** (1992) 1923.
7. Nic, J. P., Zhang, S. & Mikkola, D. E. *Scripta Metall.*, **24** (1990) 1099.
8. Wee, D. M. & Suzuki, T. *Trans. Japan Inst. Metals.*, **20** (1979) 634.
9. Wee, D. M., Noguchi, O., Oya, Y. & Suzuki, T. *Trans. Japan Inst. Metals.*, **21** (1980) 237.
10. Wee, D. M., Pope, D. P. & Vitek, V. *Acta. metall.*, **32** (1984) 829.
11. Tichy, G., Vitek, V. & Pope, D. P. *Mater. Res. Soc. Symp. Proc.*, Research Society, Pittsburgh, (1985) Vol. 39, p. 213.
12. Yamaguchi, M., Paidar, V., Pope, D. P. & Vitek, V. *Phil. Mag.*, **A45**, (1982) 867.
13. Paidar, V., Yamaguchi, M., Pope, D. P. & Vitek, V. *Phil. Mag.*, **A45** (1982) 883.
14. Tichy, G., Vitek, V. & Pope, D. P. *Phil. Mag.*, **A53** (1986) 467.
15. Tichy, G., Vitek, V. & Pope, D. P. *Phil. Mag.*, **A54** (1986) 485.
16. Takasugi, S, Hirakawa, S., Izumi, O., Ono, S. & Watanabe, S. *Acta metall.*, **35** (1987) 2015.
17. Liu, Y., Takasugi, T., Izumi, O. & Takahashi, T. *Acta metall.*, **36** (1987) 2297.
18. Winnicka, M. B. & Varin, R. A. *Scripta metall. mater.*, **25** (1991) 2297.
19. Veyssière, P. & Morris, D. G. *Phil. Mag.* (in press).
20. Gengxiang, H., Shipu, C., Xiaohua, W. & Xiaofu, C. *J. Mater. Res.*, **6** (1991) 957.
21. Inui, H., Luzzi, D. E., Porter, W. D., Pope, D. P., Vitek, V. & Yamaguchi, M. *Phil. Mag.*, **A65** (1992) 245.
22. Vasudevan, V. K., Wheeler, R. & Fraser, H. L. *Mater. Res. Soc. Symp. Proc.*, Materials Research Society, Pittsburgh, (1989) Vol. 133, p. 705.
23. George, E. P., Horton, J. A., Porter, W. D. & Schneibel, J. H. *J. Mater. Res.*, **5** (1990) 1639.
24. Morris, D. G. *J. Mater Res.*, **7** (1992) 303.
25. Morris, D. G. & Gunther, S., *Acta metall. mater.*, **40** (1992) 3065.
26. Potez, L., Lapasset, G. & Kubin, L. P., *Scripta metall. mater.*, **26** (1992) 841.
27. Lerf, R. & Morris, D. G. (in press),
28. Morris, D. G., (*Scripta metall. mater.*, **25** (1991) 713.
29. Morris, D. G., *Phil. Mag.*, **A65** (1992) 389.
30. Brown, N. *Phil. Mag.*, **4** (1959) 693.
31. Gerold, V. In *Dislocations in Solids*, ed. F. R. N. Nabarro. North-Holland, Amsterdam, (1979) Vol. 4.
32. Loiseau, A. PhD thesis, Université Pierre et Marie Curie, Paris, 1985.
33. Turner, C. D., Powers, W. O. & Wert, J. A. *Acta. metall.* **37** (1989) 2635.
34. Kumar, K. S. & Whittenberger, J. D. *J. Mater. Res.*, **7** (1992) 1043.
35. Yamaguchi, M., Umakoshgi, Y. & Yamane, T., *Mater. Res. Soc. Symp. Proc.*, Materials Research Society, Pittsburg, (1987), Vol. 81, p. 275.
36. Kocks, U. *Met. Trans.*, **A16** (1985) 2109.
37. Vanderschaeve, G., Martinez, R. & Escaig, B., in *Dislocations in Solids, 9th Yamada Conference*, ed. H. Suzuki, T. Ninomiya, K. Sumino & S. Takeuchi. Univ. of Tokyo Press, 1985.
38. Couret, A. & Caillard, D., *Phil. Mag.*, **A59** (1989) 783.
39. Couret, A. & Caillard, D., *Phil. Mag.*, **A59** (1989) 801.
40. Caillard, D., Couret, A., Clement, N., Farenc, S. & Molenat, G., in *Proc. 9th Int. Conf. on Strength of Metals and Alloys*, ed. D. G. Brandon, R. Chaim & A. Rosen. Freund, London, 1991, p. 139.
41. Friedel, J., in *Internal Stresses and Fatigue in Metals*, ed. G. M. Rassweiler & W. L. Grube. Elsevier, Amsterdam, (1959), p. 220.
42. Escaig, B., *J. Phys.*, **35** (1974). 151.
43. Biget, M. P. & Saada, G., *Phil. Mag.*, **A59** (1989) 747.
44. Groh, P., in *Dislocations et Deformation Plastique*, ed. P. Groh, L. P. Kubin & J. L. Martin. Diffusion des Editions de Physique, Société Francaise de Physique, Paris, 1979, p. 67.

Intermetallics 1 (1993) 59–63

Bonding mechanisms and point defects in TiAl

C. L. Fu & M. H. Yoo

Metals and Ceramics Division, Oak Ridge National laboratory, P.O. Box 2008, Oak Ridge, Tennessee 37831, USA

(Received 17 December 1992; accepted 6 January 1993)

The bonding mechanism and point defect structure in TiAl were investigated using a first-principles quantum mechanical calculation. The most remarkable feature found in the calculated binding charge density is the polarization of the p-electron at the aluminum sites, which gives rise to a large bond bending force between the Ti and Al layers. For the point defects, the absence of structural vacancies is predicted in TiAl, and the deviations from stoichiometry are accommodated by the substitutional antisite defects on both sublattices. High vacancy formation energies are obtained, which are closely related to the strong Ti–Al bonding and the similar atomic radii of Ti and Al.

Key words: bonding charge density, defect formation energies, defect concentrations, structural vacancies, antisite defects

1 INTRODUCTION

Fundamental information on the temperature and composition dependencies of point defect concentrations in an intermetallic compound is important for understanding and/or controlling the physical and mechanical properties of the material. Even though there has been a steady increase in research and development activities on γ-phase TiAl with the $L1_0$ structure (e.g., about one-fourth of the papers presented in a recent symposium[1] were related to this compound), this information has not been fully available for TiAl.

In 1954, Elliot and Rostoker[2] concluded from their X-ray diffraction study of Al-rich (50–62 at.%) TiAl that excess Al atoms replace Ti atoms but otherwise preserve long-range $L1_0$ order. Recently, Vujic *et al.*[3] have confirmed this result in the composition range between 50 and 58 at.% Al from X-ray measurements of the lattice parameters and gravimetric density measurements. They found that no constitutional vacancies exist in fully homogenized Al-rich TiAl, and antisite defects (Al → Ti) are the predominant structural defect in hyperstoichiometric TiAl. More recently, Shirai and Yamaguchi[4] have investigated three specific compositions (49, 52, and 56 at.% Al) using positron lifetime spectrometry, and concluded that deviations from the stoichiometric composition of TiAl are compensated by anti-site atoms, and there are no structural vacancies on either side of stoichiometry. Very recently, Brossmann *et al.*[5] have studied the formation of thermal vacancies in Al-rich (51 at.%) TiAl using positron lifetime spectrometry. An effective formation enthalpy of vacancies of 1·38 eV (133 kJ/mol) was deduced from this study, which gives a vacancy concentration of about $1{\cdot}6 \times 10^{-4}$ at. fraction near the peritectic decomposition temperature (1708 K) of γ-TiAl.[6]

The purpose of this paper is threefold: (a) to investigate the bonding mechanism in TiAl by considering the bonding charge density; (b) to report the results of first-principles quantum mechanical calculations of the self-energies for four types of intrinsic point defects (i.e., vacancies on Ti and Al sites and on Ti → Al and Al → Ti antisite defects); and (c) to determine the equilibrium defect concentrations for varying temperature and composition of γ-TiAl. In section 2, we consider the electronic structure and the bonding charge density of TiAl. The methodology, based on the non-interacting defect model, to obtain the defect structure and concentrations is briefly described in section 3. The results of our calculation is presented in section 4. Finally, in section 5, implications of the calculated point defect structure for the mechanical properties of γ-phase TiAl are discussed.

Our first-principles calculation is based on the local-density-functional (LDF) theory.[7] We solve the LDF equations by using the full-potential linearized augmented plane-wave (FLAPW) method.[8] This method represents a major

Intermetallics 0966-9795/93/$6.00 © 1993 Elsevier Science Publishers Ltd, England. Printed in Great Britain

advance in applying LDF theory to crystalline solids in that the LDF equations are solved without any shape approximation to the potential or charge density and a high degree of variational freedom (precision) can be obtained. The uniqueness of these features makes it possible to determine the energetics associated with shape deformations and lattice defects (extended or point) accurately.

2 BONDING CHARGE DENSITY OF TiAl

Recently, there has been a growing interest in measuring the bonding charge density by electron diffraction microscopy.[9] The binding charge density is defined as the response of the electron distribution, referred to the overlapping atomic charge density at the lattice sites, in the presence of a crystal field. In Fig. 1 we present the bonding charge density of TiAl on the (001) and (100) planes. The solid (dashed) contour lines in Fig. 1 denote contours of increased (decreased) electronic density as atoms are brought together to form a crystal. Figure 1(a) clearly shows the formation of directional d-bonds between nearest-neighbor Ti atoms, as expected from the open d-shell of Ti atoms. The most remarkable feature in the bonding charge density, however, is the polarization of p-electrons at the Al sites pointing directly along the [001] direction. It is noticable that the distribution of bonding charge of the Al site is highly non-spherical, i.e., a charge depletion in the (001) pure-Al plane accompanied with a build-up of charge in the [001] direction which can result in an enhancement of the Ti–Al bonding. The bonding charge density gives an indication for bond formation and the tendency for bond enhancement. However, it is important to calculate the bond strength associated with the charge density in order to gain an in-depth understanding of the interplay between bonding and strength. The binding behaviour in TiAl was examined in terms of the calculated elastic constants and the energetics associated with shear stacking faults.[10]

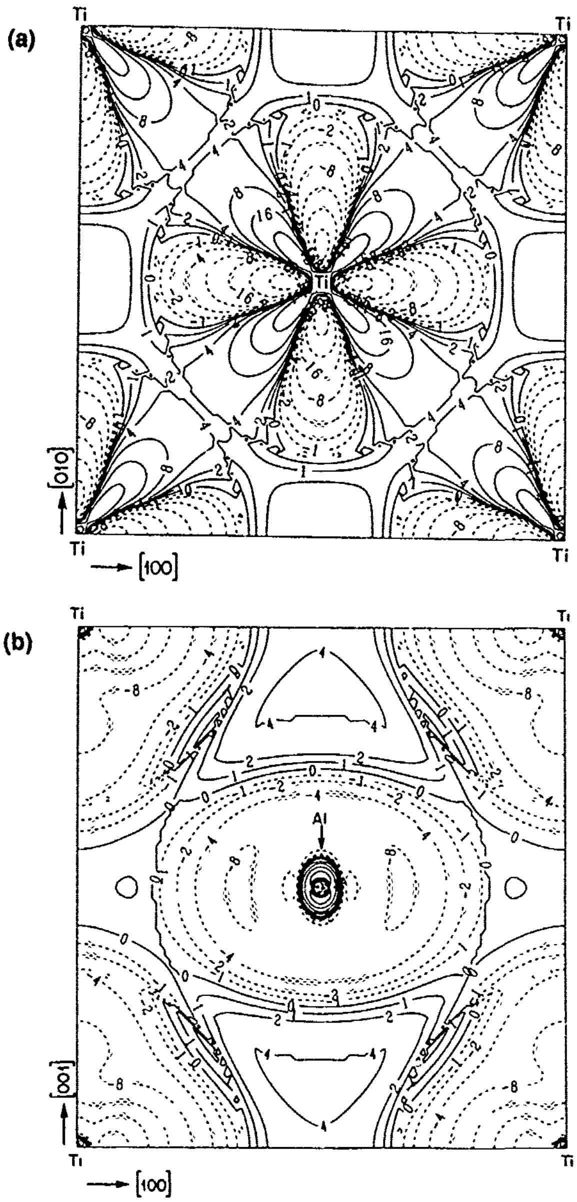

Fig. 1. The bonding charge density in TiAl on the (a) (001) and (b) (100) planes in units of 10^{-3} e/(a.u.).[3] The charge density difference plot (referred to overlapping atomic densities) shows the polarization of p-electrons on the Al sites.

It has been shown that the large bond bending force between Ti and Al layers is the physical source that gives rise to a large elastic shear modulus between Ti and Al layers (i.e., $C_{44} = 120$ GPa) as compared to the elastic shear of mixed Ti–Al planes (i.e., $C_{66} = 50$ GPa).[10] It is not only the directional Ti–Ti nearest-neighbor d-bonding but also the strong cohesion between the Ti and Al layers which controls the mechanical behavior of γ-TiAl. The relatively low stacking fault and twin boundary energies (e.g. $E_{\mathrm{twin}} = 60$ mJ/m) as compared to high antiphase boundary (APB) and complex stacking fault (CSF) energies (e.g. $E_{\mathrm{APB}} = 510$ mJ/m^2 and $E_{\mathrm{CSF}} = 600$ mJ/m) indicate that deformation twinning plays an important role in the strength and ductility of TiAl-base aluminides.[11]

3. COMPUTATIONAL APPROACH FOR POINT DEFECTS

In our approach to calculating the point defect properties, we assumed dilute defect concentrations (i.e., non-interacting defects) and considered only the configurational entropy for the entropy term. The defect concentrations were then determined from the minimization of a grand potential, Ω, which is given by

$$\Omega = E - TS - \sum_i \mu_i N_i \tag{1}$$

where the summation is over the types of atoms and μ_i and N_i are the chemical potential and the number of atoms for each component, respectively. The quantity S is the configurational entropy and E is the internal energy of the system, which is given by

$$E = E_0 + \sum_i \mu_i E_i \tag{2}$$

where the summation is over the type of defects (in the present case, there are four kinds of point defects, i.e. vacancies and substitutional antisite defects on both sublattices). In eqn (2), E_0 is the energy for a perfect crystal, and n_j and E_j are the defect concentration and internal energy for each kind of point defects, respectively. The internal energies of point defects are determined at 0 K (i.e., the effect of thermal expansion is neglected). The minimization procedure leads to the following expressions for point defect concentrations of vacancies and substitutional antisite defects at site A in thermal equilibrium (for a binary AB compound):

$$n_v = \frac{1}{2}\left[\frac{\exp\left[-(E_v^A + \mu_A)/k_B T\right]}{1 + \exp\left[-(E_v^A + \mu_A)/k_B T\right] + \exp\left[-\left(E_{\text{anti}}^{AB} - (\mu_B - \mu_A)\right)/k_B T\right]}\right] \tag{3}$$

and

$$n_{\text{anti}} = \frac{1}{2}\left[\frac{\exp\left[-\left(E_{\text{anti}}^{AB} - (\mu_B - \mu_A)\right)/k_B T\right]}{1 + \exp\left[-\left(E_{\text{anti}}^{AB} - (\mu_B - \mu_A)\right)/k_B T\right] + \exp\left[-(E_v^A + \mu_A)/k_B T\right]}\right] \tag{4}$$

In eqns (3) and (4), $(E_v^A + \mu_A)$ and $(E_{\text{anti}}^{AB} - (\mu_B - \mu_A))$ give the effective vacancy and antisite defect formation energies, respectively. The internal energies of defects (e.g., E_v^A and E_{anti}^{AB}) were determined from first-principles calculation with the inclusion of lattice relaxations at the absolute zero.

By introducing periodic arrays of point defects we used a supercell approach to calculate point defect internal energies. As long as these periodic point defects do not interact with each other, the method should provide a good representation for the energetics of a single point defect. A 32-atom unit cell was used to simulate a single point defect. This supercell geometry allowed the lattice relaxations of the first two atomic shells around each point defect site to be computed.

4 RESULTS FOR POINT DEFECTS

For stoichiometric TiAl, the calculated defect concentration as a function of temperature is shown in an Arrhenius plot (Fig. 2). No structural vacancies are predicted from our calculation, which is consistent with the recent experimental result of positron annihilation by Shirai and Yamaguchi.[4] The vacancy formation energies are calculated to be high on both Ti and Al sublattices (cf. Table 1). For example, the vacancy formation energy on the Ti sublattice (1·95 eV) gives a vacancy concentration of 10^{-6}–10^{-7} at 1500 K. Thus, the point defects in TiAl at stoichiometry are of Shottky defect type with antisite defects on both sublattices. The antisite defect concentration is predicted to be larger than 10^{-4} above 1000 K (Fig. 2). The formation energies for antisite defects at stoichiometry are also summarized in Table 1.

As in other close packed alloys (e.g. Ni_3Al), the dominant point defect types in off-stoichiometric TiAl are of antisite defects on both sublattices. Figure 3 shows the dependence of point defect types and their concentrations on the atomic percentage of aluminum at a high temperature (1273 K). In addition to the dominant substitutional antisite defects, at this temperature, the vacancy concentration (mainly on Ti sublattices) was found to be about 10^{-7} for aluminum-rich TiAl and 10^{-9} for titanium-rich TiAl. The vacancy formation energy at the titanium sites is found to decrease with increasing aluminum content: the effective vacancy formation energies of 1·80 eV and 1·68 eV are obtained for the cases of 51 at.% aluminium and 55 at.% aluminium, respectively.

The effect of lattice distortion (i.e., local tetragonal distortion) due to point defects is found to be generally small in TiAl. For Ti-rich TiAl, the main effect of lattice relaxation is to decrease the interatomic distance of substitutional defects with the first neighboring shell of Ti atoms, which corresponds to a decrease of *c/a* ratio from 1·01 to 1·00. On the other hand, for Al-rich TiAl, the lattice relaxation of the neighboring Al shell is in the direction to increase the *c/a* ratio to 1·02. The direction of atomic relaxation occurs mainly in the [001] direction. It should be mentioned that,

Table 1. The formation energies (in eV) of point defects in TiAl at stoichiometry. E_v(Ti) and E_{anti}(Ti → Al) are the vacancy formation energy at the Ti sites and substitutional antisite defect formation energy at the Al sites, respectively

E_v(Ti)	E_v(Al)	E_{anti}(Ti → Al)	E_{anti}(Al → Ti)
1·95	2·46	0·72	0·72

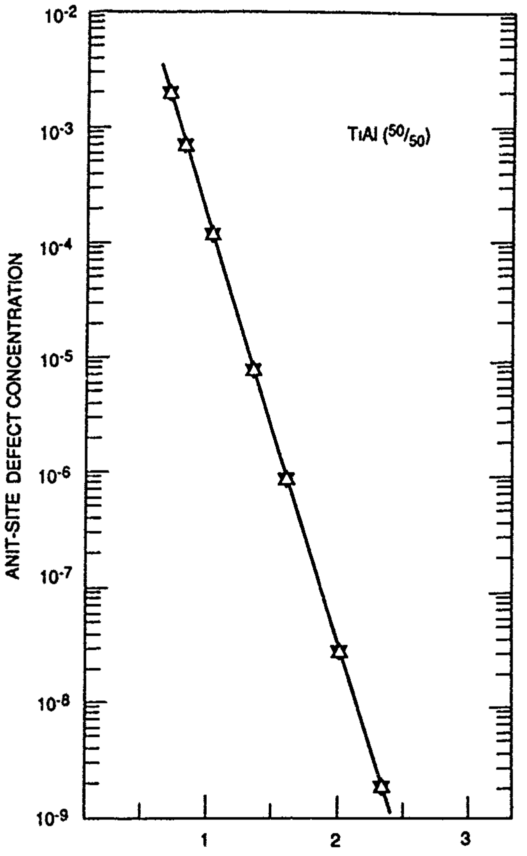

Fig. 2. An Arrhenius plot for the point defect concentrations of TiAl at stoichiometry.

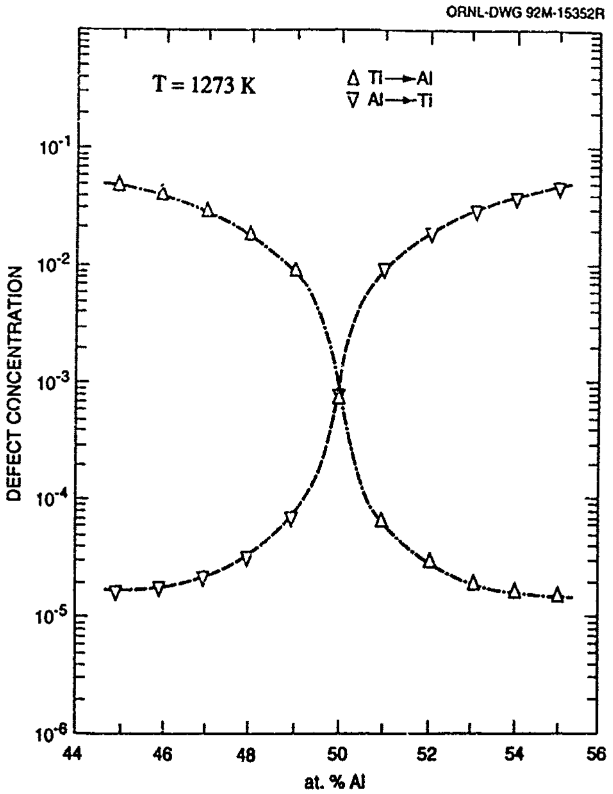

Fig. 3. The dependence of point defects structure and defect concentrations on and off stoichiometry for TiAl at 1273 K.

however, a decrease of *c/a* ratio for Ti-rich TiAl does not imply an increase in ductility, since, chemically, the structure is still not cubic.

The absence of structural vacancies in TiAl has two causes: (1) Ti and Al have similar atomic radii (which also explains the relatively small lattice distortion around the defect sites) and (2) the presence of strong Ti–Al bonding favors a close-packed structure (cf. section 2).

5 DISCUSSION

According to a recent version of the TiAl phase diagram,[12] the composition range of homogeneous γ-phase is approximately 48–68 at.% aluminum. As was mentioned in section 1, all the available experimental data[2–4] for the aluminum-rich side of off-stoichiometry are consistent with the present calculation that the dominant defects are of the Al → Ti antisite type.

Only one case of a titanium-rich (51 at.%) sample has been investigated;[4] this contained a large number of $(111)(11\bar{2})$ twins, with thin plates of α_2-Ti_3Al located on the twin boundaries.[13] According to analytical electron microscopy examination of such a lamellar microstructure, the so-called polysynthetically twinned microstructure,[14] the chemical composition of thin γ-plates is generally lower in aluminum concentration than the bulk composition.[15] Since the lamellar microstructure is known to appear over a wide range of composition, e.g., 48 to 52 at.% aluminum,[15] it is not certain whether the main constituent γ-phase of the titanium-rich specimen investigated by positron lifetime spectroscopy[4] was truly titanium-rich or not.

In any case, our calculation shows that deviations to either side of the stoichiometric TiAl are taken up by the intrinsic point defects of antisite type. The microhardness data of Vujic *et al.*[3] from the annealed samples showed that γ-phase TiAl becomes harder on either side of stoichiometry. Such a composition dependence of the hardness in TiAl (as cast) was first observed by Bumps *et al.*[16] This phenomenon is known as defect hardening in some other intermetallic compounds (e.g. Ni_3Al,[17] NiAl[18]). The hardness data on the annealed samples of TiAl are consistent with the calculated concentrations of antisite defects (Fig. 3). The almost twofold increase in the hardness of as-quenched alloys observed by Vujic *et al.*[3] may, in part, be attributed supersaturation of thermal vacancies.

The vacancy formation energies are, in general, high in TiAl. The high vacancy formation energy found in our calculation for aluminum-rich TiAl (lower than 1·80 eV) is consistent with the recent result deduced from positron annihilation experiment by Brossmann *et al.*[5] for thermal vacancies in $Ti_{49}Al_{51}$. It is noteworthy that the calculation simulates a thermal equilibrium state (which corresponds to a sufficiently long annealing time) under the assumption that the defects are well separated. Thus, it is not surprising to find that the calculated defect concentrations tend to be lower than those deduced from experiments (or a higher formation energy is calculated compared with experiments).

6 CONCLUSIONS

a. No structural vacancies in TiAl are predicted from first-principles total-energy calculations. This is due to the similar atomic size of Ti and Al and the strong p–d hybridization in TiAl of the $L1_0$ structure.
b. The dominant point defect types in TiAl are antisite defects on both sublattices. The available microhardness data on well-annealed TiAl are consistent with the calculated results.
c. Thermal vacancy concentrations are predicted to be very low, even at high temperatures (e.g., 10^{-7}–10^{-6} at 1500 K).

ACKNOWLEDGMENT

This research was sponsored by the Division of Materials Science, Office of Basic Energy Sciences, U.S. Department of Energy under contract DE-AC05-84OR21400 with Martin Marietta Energy Systems, Inc. The anonymous reviewer is gratefully acknowledged for helpful comments on the manuscript.

REFERENCES

1. Baker, I., Darolia, R., Whittenberger, D. & Yoo, M. H., *High Temperature Ordered Intermetallic Alloys V. MRS Symp. Proc.*, **288** (1993), (in press).
2. Elliott, R. P. & Rostoker, W., *Acta Metall*, **2** (1954) 884.
3. Vujic, D., Li, Z. & Whang, S. H., *Metall. Trans*, **19A** (1988) 2445.
4. Shirai, Y. & Yamaguchi. Y., *Mater. Sci. Eng. A*, **152** (1992) 173.
5. Brossmann, U., Badura, K. & Schaefer, H. H., to be published (quoted in Ref. 6).
6. Mehrer, H., Sprenzel, W. & Denkinger, M., *Diffusion in Intermetallic Compounds and Order Alloys*, eds. B. Fultz, R. W. Cahn and D. Gupta. TMS Symp. Proc., 1993, to be published.
7. Hohenberg, P. & Kohn, W., *Phys. Rev. B*, **136** (1984) 864.
8. Wimmer, E., Krakauer, H., Winert, M. & Freeman, A. J., *Phys, Rev. B.*, **24** (1981) 864.
9. Fox, A. G. & Tubbernor, M. A., *Acta Metall.*, **39** (1991) 669.
10. Fu, C. L. & Yoo, M. H., *Phil. Mag. Lett.*, **62** (1990) 159.
11. Yoo, M. H., Fu, C. L. & Lee, J. K., *MRS Symp. Proc.*, **213** (1991) 545.
12. Massalski, T. B. (ed.), *Binary Alloy Phase Diagrams.* ASM, Metals Park, Ohio, 1986.
13. Sastry, S. M. L. & Lipsitt, H. A., *Metall Trans*, **8A** (1977) 299.
14. Fujiwara, T., Nakamura, A., Hosomi, M., Nishitani, S. R., Shirai, Y. & Yamaguchi, M., *Phil. Mag. A*, **61**, (1990) 591.
15. Umakoshi, Y., Nakano, T. & Yamane, T., *Mater. Sci. Eng. A*, **152** (1992) 81.
16. Bumps, E. S., Kessler, H. D. & Hensen, M., *Trans. AIME*, **194** (1952) 690.
17. Suzuki, T., Mishima, Y. & Miura, S., *ISIJ Int.*, **29** (1989). 1.
18. Noebe, R. D., Bowman, R. R. & Nathal, M. V., *Int. Mater. Rev.* to be published.

Intermetallics 1 (1993) 65–78

Observation of high index {511} type fracture planes and their influence on toughness in NiAl single crystals

R. Darolia

GE Aircraft Engines, 1 Neumann Way, Cincinnati, Ohio 45215, USA

K.-M. Chang

Industrial Technology Research Institute, Chutung, Hsinchu, 310 Taiwan

&

J. E. Hack

Department of Mechanical Engineering, Yale University, New Haven, Connecticut 06520, USA

(Received 4 January 1993; accepted 18 January 1993)

The cleavage fracture of NiAl has been investigated by fracture toughness tests on single crystals. Unlike FeAl single crystals, which cleave along {100} planes similar to many bcc metals, the preferred cleavage plane in NiAl is {110}. In addition to the unusual {110} cleavage plane, NiAl single crystals also form transient high-index fracture facets near the notch of fracture toughness specimens. Like most cleavage facets, the transient fracture facets are macropically flat and optically shiny. Laue X-ray diffraction, scanning electron microscopy, and surface trace analysis were used to determine that the transient fracture facets are high-index crystallographic planes near {511}. The area fraction of fracture surface consisting of transient fracture facets was found to be a function of specimen orientation. A direct correlation between the measured fracture toughness and the transient fracture area was also observed. Alloying additions to NiAl for improved strength and toughness influenced the formation of {511} facets. In highly alloyed NiAl alloys, the tendency to form high-index fracture facets was reduced. The mechanism of formation of high-index planes is not clearly understood; however, experimental observations indicate that their occurrence is related to deformation in the material prior to crack instability. These facets were not present when NiAl was deformed under high strain rates. The measured fracture toughness values and fracture planes were highly sensitive to specimen geometry, orientation, test technique, and the alloying additions, as well as to stoichiometry.

Key words· nickel aluminide, NiAl single crystals, fracture plane, fracture toughness, {511} transient plane

INTRODUCTION

Alloys based on NiAl offer significant payoffs as structural materials in gas turbine applications due to a unique range of physical and mechanical properties. These properties include low density, high thermal conductivity, high melting temperature, and excellent oxidation resistance. Very significant improvements in the strength and ductility of NiAl single crystals have been achieved through alloying.[1,2] Ambient-temperature tensile ductility as high as 6% has been achieved in NiAl single crystals containing less than 0·5% (at.) of Fe, Ga or Mo.[3] In addition, tensile strength and stress–rupture properties which compete with current Ni-base superalloys have been achieved through precipitation of an ordered $L2_1$ Heusler phase in NiAl single crystals. However, NiAl single-crystal

Intermetallics 0966-9795/93/$6.00 © 1993 Elsevier Science Publishers Ltd, England. Printed in Great Britain

alloys which possess the best high-temperature strengths are less ductile than binary NiAl, and possess low fracture toughness values. The low fracture toughness of single-crystal alloys remains an issue which must be resolved through further understanding of the fracture processes.

Fracture in NiAl single crystals does not occur in a single cleavage plane, and several crystallographic facets are often seen.[4–6] Unlike FeAl, which cleaves on {100} planes,[5] the cleavage plane for NiAl is not well defined. Prior to final cleavage on the {110} plane, which appears to be the predominant cleavage plane in NiAl, cleavage on 'transient' fracture planes such as {511} or {711} is seen in NiAl when tested in a bend test. Low-index fracture planes are also not generally seen in single-crystal tensile specimens, and facets of several high-index planes, such as {511}, {711}, {123}, and {221}, are often observed.[6] The occurrence of the {511} or the {711} cleavage planes has been confirmed under a variety of other test conditions. The cleavage phenomena on such high-index planes are not yet understood. We have performed an in-depth study on the formation of {511} transient fracture facets in NiAl single crystals and their crystallographic features. This paper describes the experimental conditions under which {511} planes occur, discusses their effect on the fracture toughness of NiAl, and provides evidence that their occurrence is related to deformation in the material prior to crack instability.

2 EXPERIMENTAL PROCEDURE

Single-crystal slabs, 25 mm × 32 mm × 100 mm, of binary stoichiometric NiAl and NiAl alloys were grown in argon by a Bridgman method. The slabs were homogenized in an argon atmosphere at 1316°C for 50 h. They were then oriented using the back-reflection Laue technique and specimens were electro-discharge machined (EDM) wire-cut from the slabs in the desired crystallographic orientations. Specimens of various test configurations were produced using low-stress grinding techniques. The specimens were electropolished in a solution of 10% perchloric acid and 90% methanol at −30°C to remove residual grinding strains. Tests were conducted in air at ambient temperature and at selected elevated temperatures. The long axis of the specimens was ⟨100⟩, ⟨110⟩, or ⟨111⟩. A through, single-edge notch or a chevron notch was cut along specified crystal directions by EDM at the center of the specimen (Fig. 1). Figure 2 is a schematic diagram of the test set-up, with a bend bar of rectangular cross-section 7·6 mm × 3·8 mm used to determine fracture toughness. In addition to determining fracture surface orientations from the bend specimens, fracture surfaces from double cantilever beam toughness specimens (Fig. 3) were also analyzed. In selected cases, fracture surfaces from uniaxial tension, strain-controlled low-cycle fatigue, and tensile stress–rupture specimens were also determined. In another series of experiments, a compact tension specimen was explosively cracked by detonating a small amount of high explosive in the notch of the specimen to evaluate the effect of very high strain rates on the occurrence of the {511} planes.

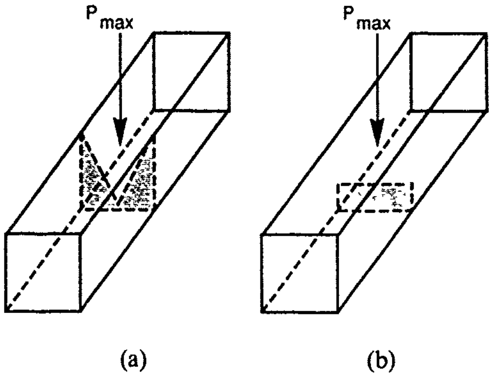

Fig. 1. Four-point bend toughness test specimens: (a) chevron-notched; (b) through-notched.

The fracture surfaces were examined by optical as well as scanning electron microscopy. The orientation of the fracture surface facets in several regions of each specimen was determined by using the back-reflection Laue X-ray diffraction technique. For this determination, the specimen after fracture was mounted on a holder having three mutually perpendicular axes of rotation. The fracture surface was examined under an optical microscope. A high-intensity light beam was aimed at the area of interest through an optical

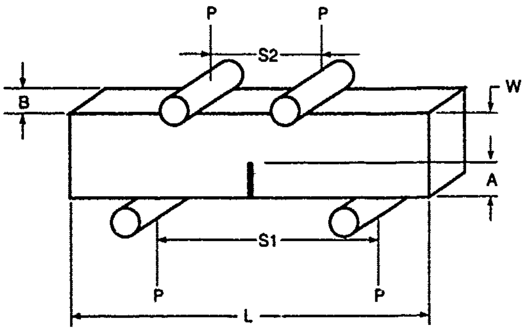

Fig. 2. Four-point bend toughness test specimen and test set-up.

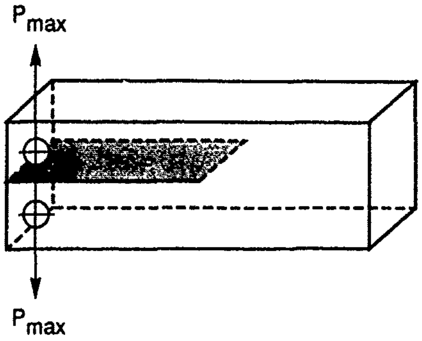

Fig. 3. Double cantilever beam toughness specimen.

fiber tube, mounted parallel to the optical axis of the microscope. The specimen was aligned by observing the reflection of the light beam. The flat facets were set in a horizontal position as the full reflection of the light beam was reached. The aligned specimen on the specimen holder was then moved to a Laue X-ray diffractometer for orientation determination. The accuracy of this technique was independently verified by Schneibel *et al.*[6] using an Hitachi S-800 scanning electron microscope (SEM). The details of this technique are described in Ref. 6. Briefly, in the SEM technique, the specimens are mounted such that, with the specimen stage untilted, their axes coincide with the optical axis of the instrument. Micrographs of individual facets are taken at tilts of 0 and 40°C in two orthogonal directions. From the changes in projected lengths between fiducial features, the angles in two orthogonal directions are calculated. The facet normals are subsequently evaluated in polar coordinates and related to the crystallographic directions of the specimen. In both these techniques, the facet normals were plotted on stereographic projections containing the specimen axes as origins. A comparison between the SEM technique and the X-ray technique showed that the two techniques gave similar results, typically within 5–10°. In this paper, unless otherwise stated, results from the X-ray technique are discussed.

3 RESULTS

3.1 Fracture surfaces of the toughness specimens

3.1.1 Through-notched bend specimens

In all specimens, except in highly alloyed and explosively deformed specimens, the initiation area at and near the initiation point always consisted of small facets, as shown in Fig. 4. These facets are believed to be crystallographic planes because of their visual brightness. The crystallographic orientation of these facets was determined to be either {511} to {711}. The {511} planes were mostly observed, with occasional observation of the {711} planes. The location of the planes is shown in standard stereographic triangle in Fig. 5. Depending on the orientation of the specimen, the final fracture facet could be a {110} plane, which appears to be the preferred cleavage plane in NiAl. The area fraction of the initial fracture facets, which we call 'transient' planes, appear to be related to the orientation of the test specimen, as will be discussed later.

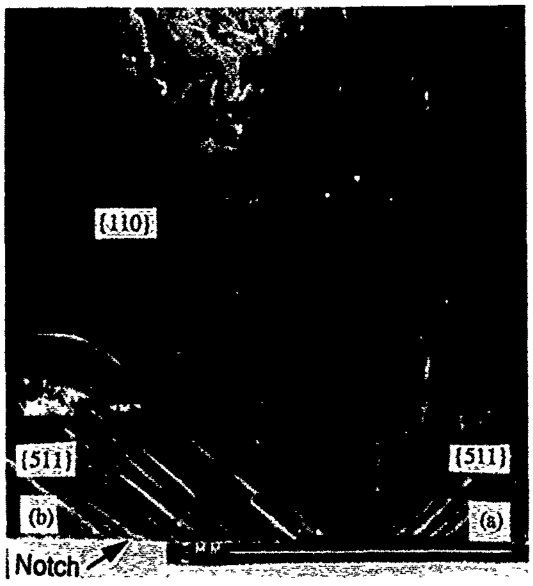

Fig. 4. Prior to final cleavage on the {110} plane, cleavage on transient fracture planes such as {511} seen in NiAl in a ⟨100⟩ oriented bend specimen with a through notch.

In the case of ⟨100⟩ oriented bend test specimens with a through notch, the transient fracture region consists of a closely spaced layer structure next to the notch root (areas a and b in Fig. 4) made up of fracture facets which were determined to be symmetrically equivalent {511} planes, as shown in Fig. 5. Each variant occupies

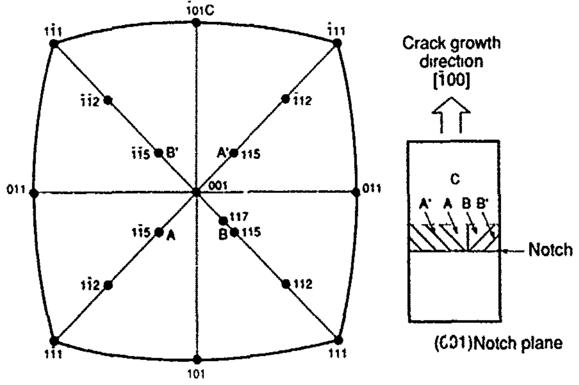

Fig. 5. Orientation of fracture facets of Fig. 4 observed in an NiAl ⟨100⟩ oriented bend specimen with a through notch.

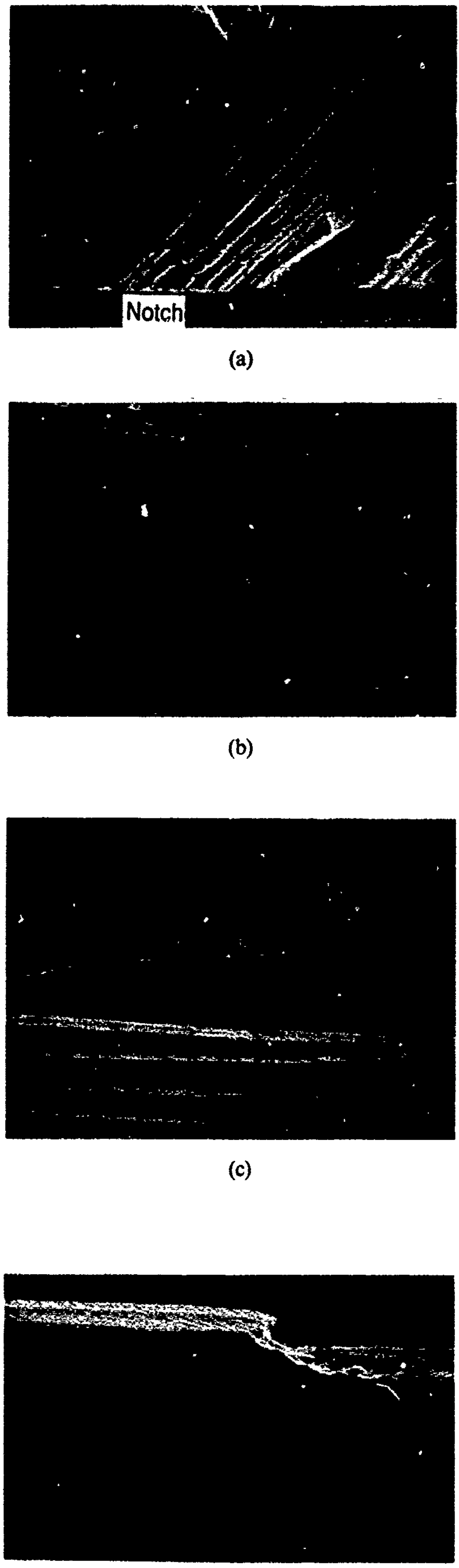

(a)

(b)

(c)

(d)

Fig. 6. (a)–(c) Higher magnifications of the layer structure; (d) cleavage step bridging two {511} facets.

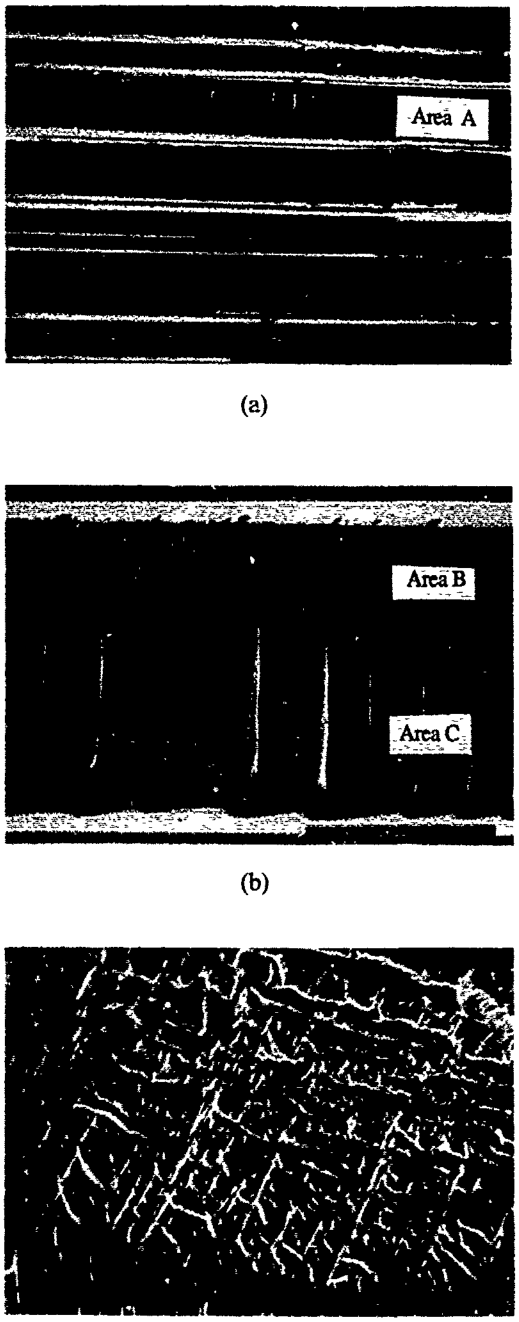

(a)

(b)

(c)

Fig. 7. (a) Side view of the fracture facets; (b) high-magnification fractography of the area A of Fig. 7; (c) high-magnification fractography of the area B of Fig. 7(b).

a certain portion of the transient fracture area, and generally consists of a series of parallel cleavage-like facets with spacing ranging from 10 to 200 μm. The surface traces of two variant on the {100} plane form angles of +45°C and −45°C, respectively, with the [100] crack growth direction. In some ⟨100⟩ specimens, only one variant of the transient fracture facets forms across the notch root. Figure 6 shows several higher magnifications of the layer structure. High-magnification fractography of {511} facets is featureless except for

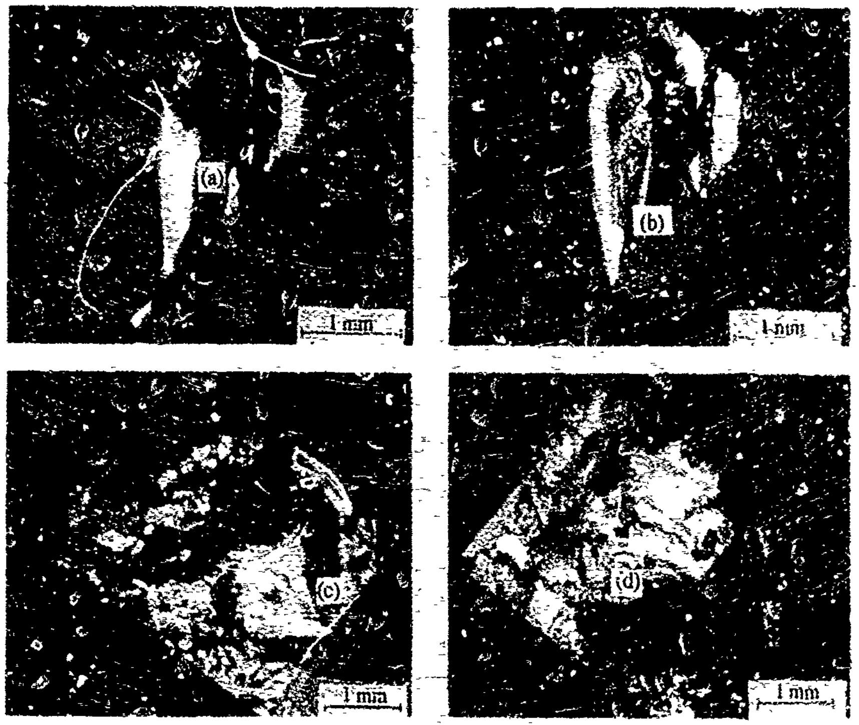

Fig. 8. Fracture facets in ⟨111⟩-oriented bend bar. Four high reflection areas are shown.

some lines, as seen in Fig. 6(c). No river patterns typical of cleavage fracture were observed. On the other hand, the fracture steps bridging two {511} facets exhibited interesting features, as shown in Figs 6(d) and 7. Several of these features are shown in the high-magnification fractographs of the steps connecting the fracture facets in Figs 7(a), (b), and (c). A considerable amount of deformation is obvious in these steps.

The transient fracture facets show a different morphology on the fracture surface of the ⟨111⟩ specimen. There is only one facet instead a series of parallel facets for each variant. Two facets of different variants and sizes are observed at the notch root. The large transient facet is somewhat curved. In Fig. 8, these facets are shown with the highest reflection when they are accurately aligned with the optical beam. Figure 9 shows the result of optical alignment and Laue X-ray diffraction of the facets in Fig. 8. Both facets are near {511}, although a variation from {711} to {311} was measured on the different areas of the large facet due to its curvature. Again, featureless {511} facets did not shown a river pattern typical of cleavage fracture.

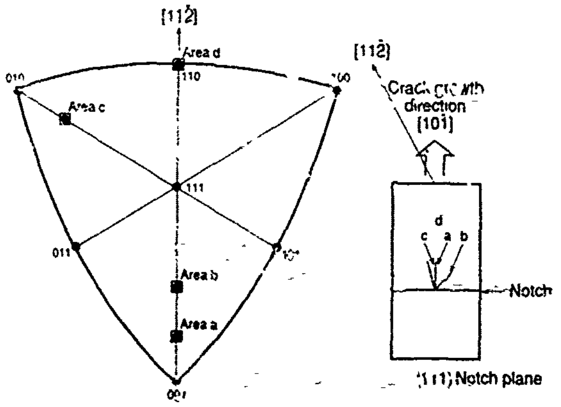

Fig. 9. Orientation of fracture facets of Fig. 8 observed in an NiAl ⟨111⟩ oriented bend specimen with a through notch.

The transient facet area fraction in the ⟨110⟩ specimen is the smallest of the various orientations studied, because the notch plane is parallel to the preferred cleavage plane. Nevertheless, in stoichiometric NiAl, where some tensile ductility is observed in this orientation, transient fracture places are still seen. As will be discussed later, in stronger NiAl alloys, where the material shows no tensile plasticity at ambient temperature, the transient fracture area is absent.

Figure 10 shows a scanning probe microscope image of one of the fracture facets, which shows 25 μm wide parallel cleavage facets separated by 2–5 μm high steps. In this technique, the features shown in areas A, B, and C are generally representative of the topological details of the surface, whereas the details shown on the steps are instrumentation-related artifacts that are not related to the surface features of the steps. Evaluation at very high magnifications of area A shows a fairly flat surface.

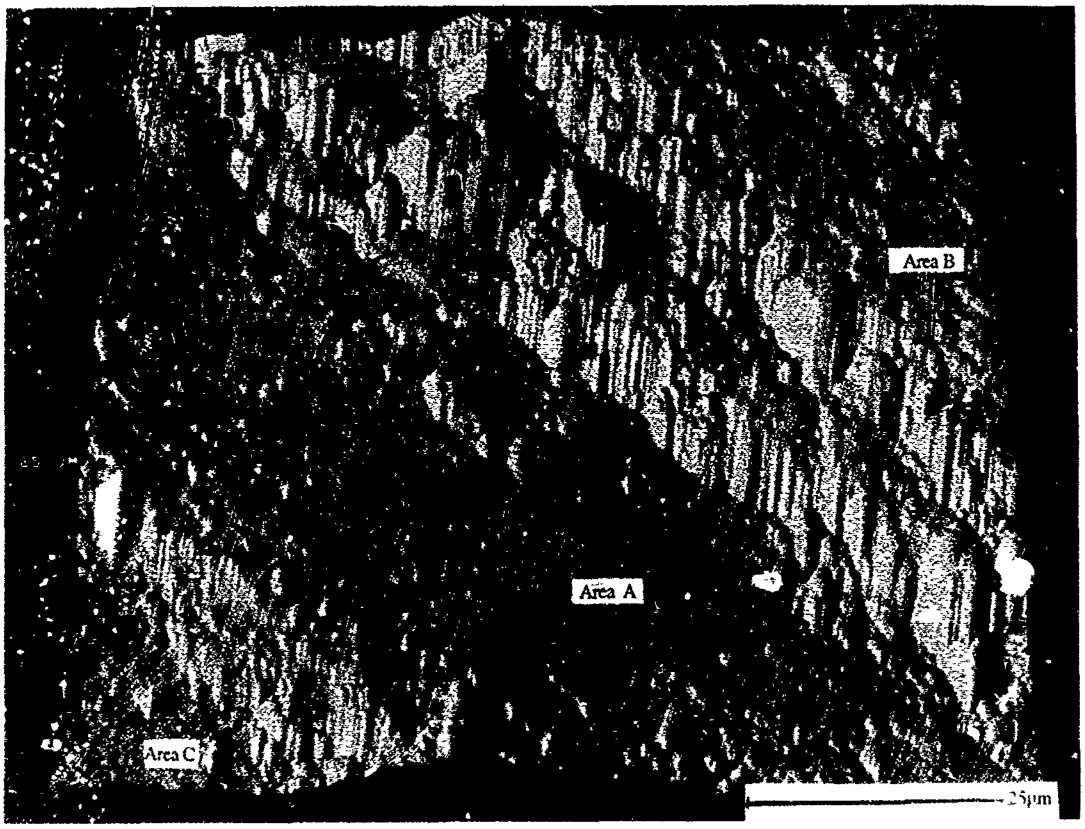

Fig. 10. Scanning probe microscope image of one of the fracture facets.

3.1.2 Chevron-notched bend specimens

A $\langle 100\rangle$-oriented NiAl bend bar of near-stoichiometric composition with a chevron notch was tested at ambient temperature for fracture toughness determination. After the test, the fracture surface was analyzed to determine the cleavage planes. Three clearly distinguishable fracture facets, A, B, and C (Fig. 11), originating at the root of the notch, were identified by the light-reflection technique. The cleavage habit of these facet was subsequently determined by the Laue technique. As seen in the stereographic projection in Fig. 12, these planes were identified as $\{511\}$. A small cleavage area of $\{110\}$ planes was seen toward the end of the fracture surface.

3.1.3 Double cantilever beam toughness specimens

As was the case with the bend specimens, the fracture surface of the double cantilever beam toughness specimens also consisted of transient fracture facets near the root of the notch, whereas $\{110\}$ cleavage was observed away from the notch. The transient fracture facets were analyzed by the Laue techniques to be $\{511\}$ type planes. An example is given for a $\langle 110\rangle$-oriented stoichiometric NiAl single-crystal specimen in Fig. 13, where the transient fracture area consisted of crescent-shaped facets. These facets were sub-sequently analyzed to be high-index planes near $\{711\}$.

3.1.4 Explosive loading experiments with double cantilever beam toughness specimens

The fracture surface of a $\langle 110\rangle$-oriented stoichiometric NiAl double cantilever beam toughness specimen deformed explosively is shown in Fig. 14. This specimen was tested at three loading rates. The first two rates were high strain rates, and were obtained by detonating small amounts of explosive: fracture area A was formed during the first explosion while area B was formed during a second explosion. Area C was deformed at a standard strain rate. Except for the small fracture area near the root of the notch, the cleavage plane of which was identified near $\{210\}$, the cleavage plane of the fracture surfaces A and B was identified at $\{110\}$. The fracture surface C, which was formed at the standard slow strain rate, consists of two fracture areas: (1) a transient fracture initiation area, with a cleavage plane near the $\{210\}$; and (2) the final fracture area, with a $\{110\}$ cleavage plane. This experimental observation clearly demonstrates that the formation of high-index fracture can be suppressed when the mobility of dislocations is minimized by higher strain loading in NiAl.

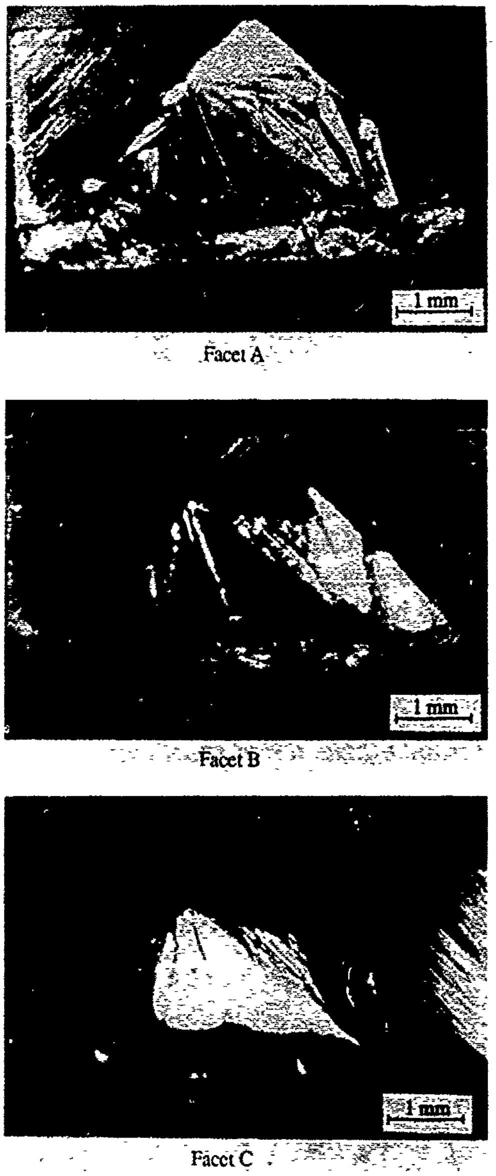
Facet A

Facet B

Facet C

Fig. 11. Fracture facets in a ⟨100⟩-oriented chevron-notched bend bar. Three high reflection areas are shown.

3.2 Fracture surfaces of the tensile, stress-rupture and fatigue specimens

3.2.1 Smooth bar tensile specimens

The fracture surface of stoichiometric NiAl tensile specimens was composed of many fracture 'facets' of various orientations. Some 'facets' were close to {511} but none of them were of a low-index crystallographic plane. In Fig. 15(a), the fracture surface of a ⟨110⟩ oriented ambient-temperature tensile specimen is shown. The orientation of the fracture facets for this specimen were analyzed by X-ray diffraction. Schneibel *et al.*[6] also analyzed the fracture surface of this specimen using SEM, as described earlier. The stereographic projection in Fig. 15(b) contains a comparison between the SEM and the X-ray diffraction techniques. Since the fracture surfaces are not completely smooth, a perfect match from the two techniques is not expected. However, as shown for facets 1, 2, 3, and 4, the two techniques provide similar facet orientations. Facet 4 consisted of a semi-periodic arrangement of two alternating microfacets, numbers 4A and 4B. Both of these microfacets were evaluated by the SEM technique, whereas the X-ray technique evaluated only the 4A facet.

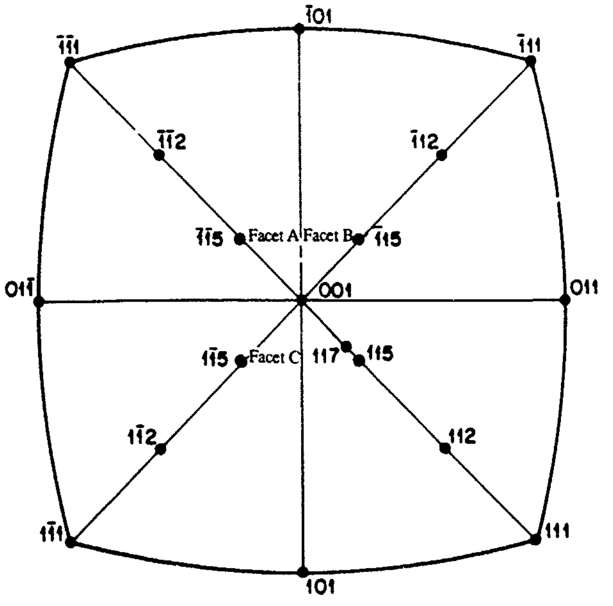

Fig. 12. Orientation of fracture facets of Fig. 11 observed in an NiAl ⟨100⟩-oriented chevron-notched bend specimen.

3.2.2 Notched tensile specimens

Two tensile specimens of stoichiometric NiAl were prenotched prior to tests at ambient temperature to determine whether a prenotch will promote the formation of the {511} fracture facets as opposed to facets of several different types of high-index planes. The evaluation of the fracture surfaces of

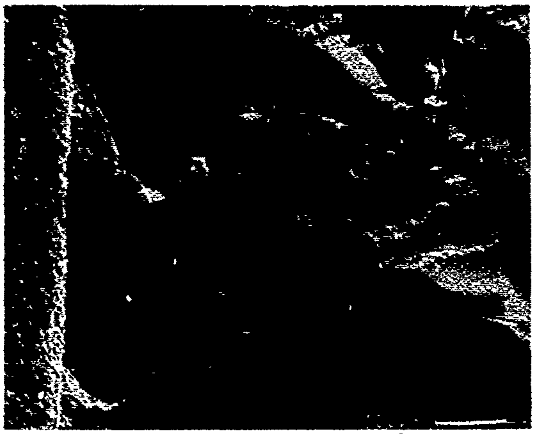
Fig. 13. Transient fracture area consisting of crescent-shaped fracture facets near the notch root in a double cantilever beam toughness specimen.

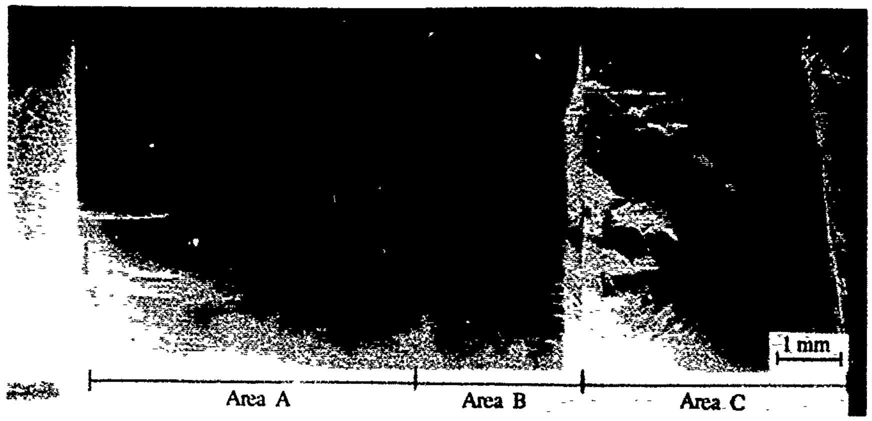

Fig. 14. Fracture surfaces of an explosively cracked stoichiometric NiAl double cantilever beam toughness specimen.

these specimens still showed fracture facets of several different high-index planes, including a plane near {711}, as shown in a stereographic projection of one of the specimens (Fig. 16).

3.2.3 Tensile stress–rupture tested specimens

The fracture surface of a ⟨110⟩-oriented smooth bar tensile stress–rupture specimen of an Hf-containing NiAl alloy was analyzed after the test to determine the cleavage planes. This specimen had an elongation of approximately 30% (see elliptical cross-section of the specimen in Fig 17) after the test at 871°C at a stress of 240 MPa. Three clearly distinguishable fracture facets. A, B, and C (Fig. 17), were identified by the light-reflection technique. The cleavage planes of these facets were determined by the Laue technique. As seen in the standard stereographic projection in Fig. 18, these planes were identified to be {511} type.

3.2.4 Tensile fatigue tested specimens

Fracture surfaces of two low-cycle fatigue ⟨100⟩ specimens of a high-strength Hf-containing NiAl alloy were analyzed to determine cleavage planes under low-cycle fatigue conditions. The specimen F1 had undergone over 96 000 cycles before

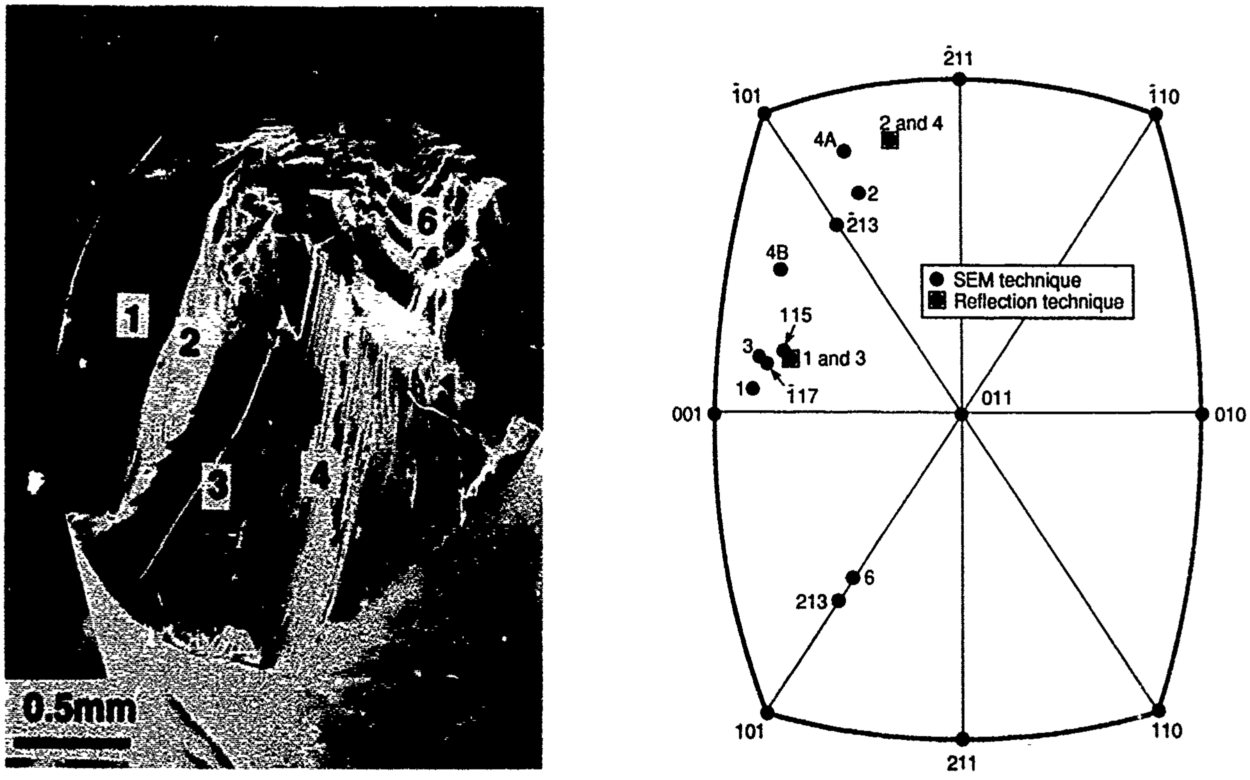

(a) (b)

Fig. 15. (a) Fracture surfaces of a stoichiometric NiAl ⟨110⟩-oriented ambient-temperature tensile specimen; (b) orientation of fracture facets determined by SEM and X-ray diffraction.

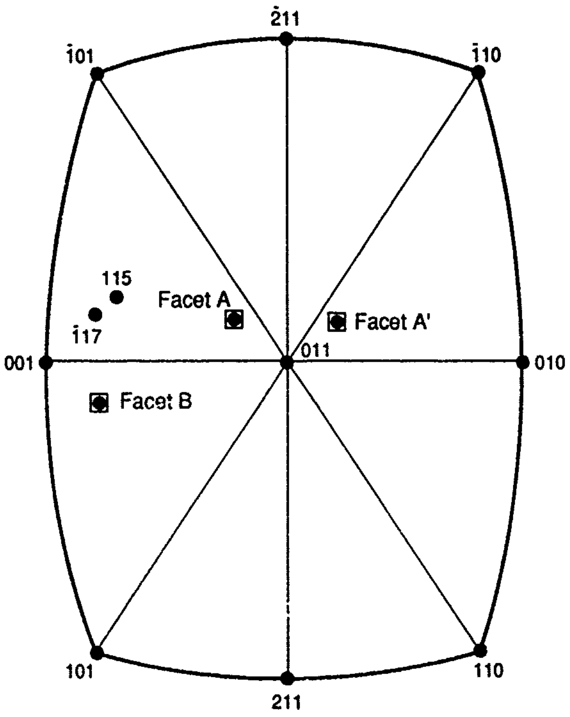

Fig. 16. Stereographic projection of the fracture facets in a prenotched tensile specimen.

failure at 649°C, and the specimen F2 had undergone 91 000 cycles before failure at 649°C. Four high-reflection facets in specimen F1 (Fig. 19) and three high-reflection facets in specimen F2 were identified by the light-reflection technique. It is remarkable that all these facets were identified as {511} planes, as shown in the stereographic projections in Fig. 20 for specimen F1.

3.3 Effect of stoichiometry and alloying

The strength of NiAl is known to be a strong function of its stoichiometry; a small deviation from the stoichiometry can significantly increase its strength. For example, the tensile yield strengths at ambient temperature, measured in the ⟨110⟩ direction are about 190 MPa for Ni–50Al and 400 MPa for Ni–48Al; in contrast, a Ni–46Al composition does not show any plasticity at ambient temperature, and has a fracture strength of around 620 MPa. Even though, in isolated cases, small areas of transient facets are seen, the fracture surfaces in the Ni–48Al and Ni–46Al compositions do not generally show {511} facets in the bend specimens.

The influence of alloying additions in NiAl, which improve strength at the expense of ambient-temperature ductility, on the formation of {511} transient fracture facets was also studied. Several of the high-strength NiAl alloys were evaluated for toughness in bend tests of through-notched as well as chevron-notched ⟨110⟩-oriented specimens. In all cases, the fracture surface consisted of {110} cleavage plane without any indication of {511} type high index facets. An example of the fracture surface of a low-ductility NiAl alloy chevron-notched bend specimen tested at ambient temperature is shown in Fig. 21. The {110} cleavage plane was easily identifiable by surface trace analysis. Another example of a typical fracture surface of a through-notched bend specimen in a high strength, low-ductility alloy is shown in Fig. 22. As can be seen in Figs 21 and 22, fracture took place on a single cleavage plane, which was determined as {110}. It should be mentioned that the fracture surface of these alloys, when tested in a stress–rupture test, consisted of only {511} facets. The failure in this specimen took place after con-

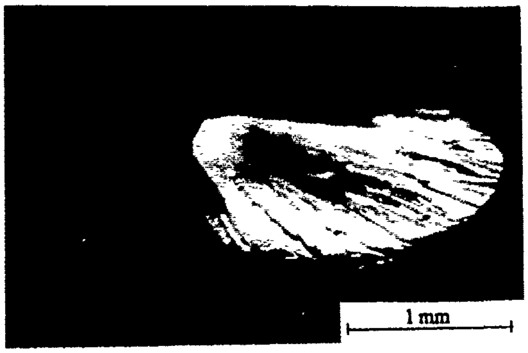

Facet A

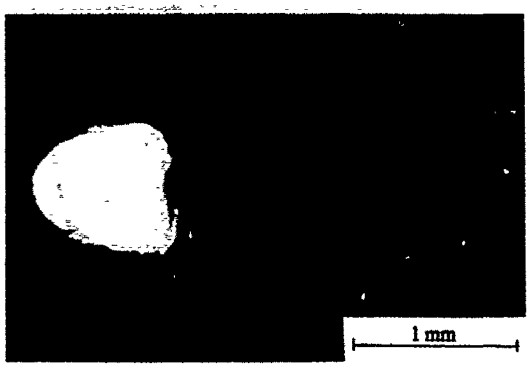

Facet B

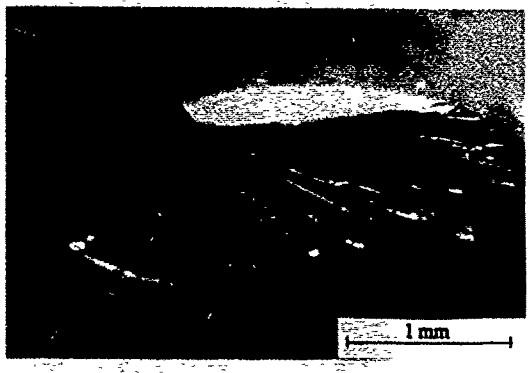

Facet C

Fig. 17. Fracture facets in a ⟨110⟩-oriented stress–rupture tested specimen. Three high reflection areas are shown.

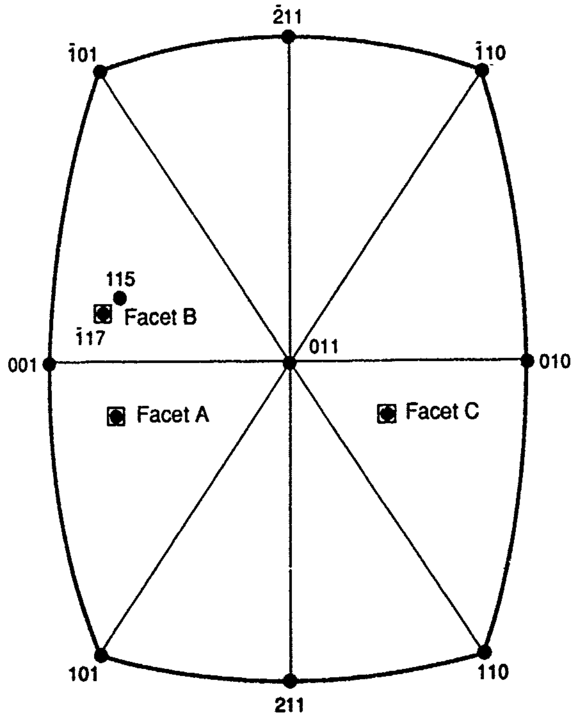

Fig. 18. Stereographic projection of the fracture facets of Fig. 17.

siderable creep deformation, thereby prompting the formation of high-index fracture facets. These results confirm the theory that prior plastic deformation is involved in the formation of {511} facets.

As was mentioned earlier, the fracture surface in stoichiometric NiAl in tensile tests always consisted of several high-index planes, including {511}. In the case of strong, low-ductility alloys, a clear trend was not observed. In most cases, the fracture surfaces of the tensile specimens still consisted of many high-index facets, including {511}, which were always observed at or near the fracture initiation sites. However, in isolated incidences, a single cleavage plane was observed. In such specimens, it was difficult to locate the fracture initiation sites. It is possible that localized deformation at the fracture initiation sites promotes the formation of high-index facets.

3.4 Orientation dependence

The area fraction of the fracture surface of through-notched specimens containing {511} facets

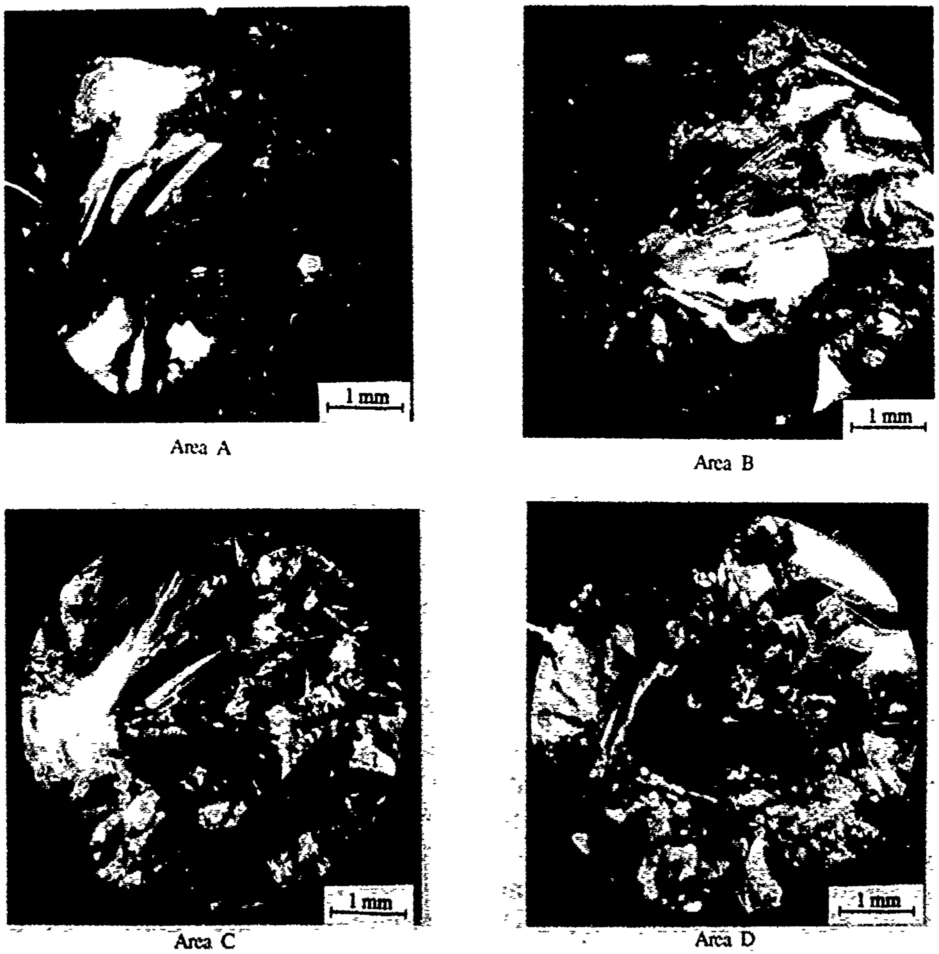

Area A

Area B

Area C

Area D

Fig. 19. Fracture facets in a ⟨100⟩-oriented low-cycle fatigue tested specimen. Four high reflection areas are shown.

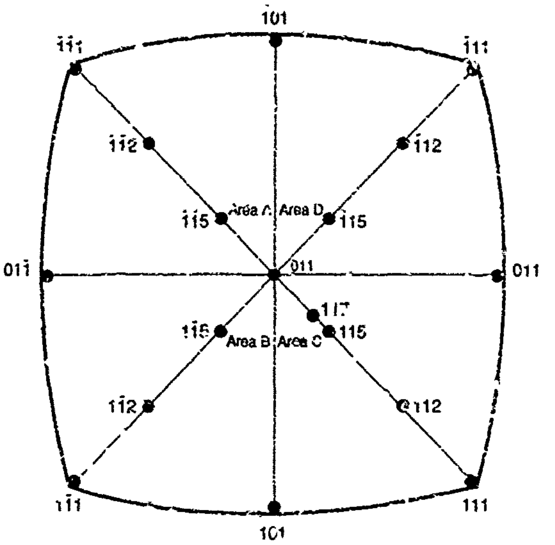

Fig. 20. Stereographic projection of the fracture areas of Fig. 19.

was found to be dependent on the orientation of the specimen; it was found to be related to the deviation of the specimen orientation from the normal of the preferred {110} cleavage plane. To further investigate the dependence of formation of {511} facets on specimen orientation, single-crystal specimens of stoichiometric NiAl were oriented along six crystallographic directions, and fracture toughness specimens were machined with a wire EDM notch normal to the specimen direction. An ideal fracture test occurs when the notch plane is parallel to the preferred cleavage plane {110}. The measured fracture toughness in this case can be considered as the intrinsic fracture resistance of NiAl crystals. In other cases, crack deflection from the notch plane to an active {110} plane will occur For each orientation, the percentage of transient fracture area with respect to the total fracture area was measured. Duplicate tests were performed for each orientation. Table 1 lists the transient fracture area fraction for all the orientations investigated, and the corresponding fracture toughness. The formation of transient {511} fracture facets is clearly orientation-dependent. The observed transient fracture area can be correlated with the fracture toughness for that orientation. When a single-crystal specimen is oriented near the normal of a preferred cleavage plane {110}, the measured fracture toughness is low, as is the transient fracture area fraction. There is some scatter in the fracture toughness and transient fracture area data between the two duplicate tests for each orientation. Lack of precracking to generate a consistent and sharp crack tip might be the cause for the observed scatter. Several precracking techniques, including fatigue testing, were tried, but the crack direction could not be controlled in the notch plane. Nevertheless, the specimen in every orientation with a high value of fracture toughness seems to have a high area fraction of transient {511} fracture.

Fracture specimens of various orientations were

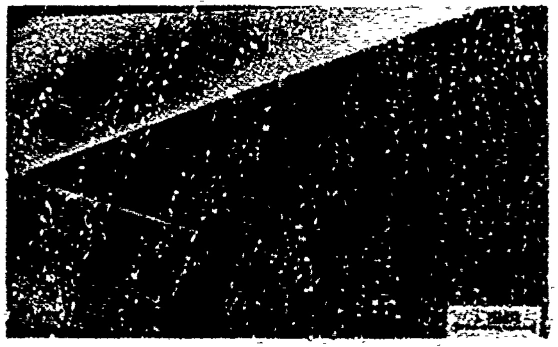

Fig. 21. Fracture surface of a low-ductility NiAl alloy chevron-notched bend specimen tested at ambient temperature. The {110} cleavage plane was easily identifiable by surface trace analysis.

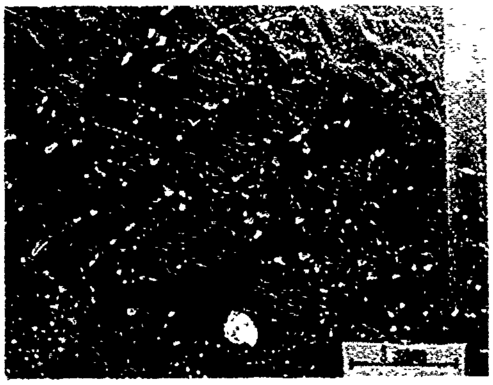

Fig. 22. Fracture surface of a through-notched bend specimen in a high-strength, low-ductility alloy; fracture took place on a single cleavage plane, which was determined to be {110}.

Table 1. Orientation dependence of fracture toughness and transient fracture area in a stoichiometric NiAl

Orientation	Fracture toughness (MPa√m)	{511} fraction (%)
⟨100⟩	6·2	9·7
	8·3	15·7
⟨510⟩	12·1	29·3
	7·6	9·5
⟨210⟩	4·1	0·0
	5·0	0·0
⟨110⟩	4·9	0·0
	5·6	3·5
⟨221⟩	4·1	7·1
	6·6	18·9
⟨111⟩	7·6	29·3
	7·3	36·3

Table 2. Orientation dependence of fracture toughness in an Ni–46Al single-crystal slab at ambient temperature and 400°C

Orientation	Ambient temperature fracture toughness (MPa$\sqrt{m}$)	400°C fracture toughness (MPa$\sqrt{m}$)
⟨110⟩	2·4	5·8
⟨441⟩	2·7	Not measured
⟨332⟩	2·7	Not measured
⟨223⟩	1·6	4·7
⟨221⟩	3·3	Not measured
⟨111⟩	7·6	12·0
⟨112⟩	3·3	Not measured
⟨113⟩	3·6	Not measured
⟨115⟩	3·3	Not measured

also machined from a high-strength Ni–46Al single-crystal slab. Fracture toughness measured at ambient temperature and 400°C are shown in Table 2. At ambient temperature, the anisotropy of fracture toughness cannot be clearly determined, because of the very low toughness values of about 3 MPa$\sqrt{m}$. The experimental accuracy at such low values may mask the orientation effect. In no orientation was there any indication of transient {511} fracture facets on the flat cleavage fracture surface. However, the fracture toughness of the strong Ni–46Al single crystals increases significantly at 400°C, to 12·0 MPa$\sqrt{m}$. The ductile-to-brittle transition temperature (DBTT) of the Ni–46Al single crystals was not measured; however, the DBTT has been found to be 300°C in Ni–50Al single crystals.[1] Therefore, a DBTT of about 300–400°C is expected in Ni–46Al single crystals. Figure 23 compares the fracture surfaces of ⟨111⟩-oriented bend specimens tested at ambient temperature and at 400°C. A flat fracture surface without the {511} fracture facets is formed at ambient temperature. Transient fracture facets are observed on the fracture surface tested at 400°C, where an increase in fracture toughness occurs, and the specimen is presumably ductile.

Table 3. Percent {511} fracture area as a function of fracture toughness in stoichiometric NiAl

Specimen	Ambient room temperature fracture toughness (MPa$\sqrt{m}$)	Percent of {511}
6A	2·4	0·4
5L	2·8	0·7
2C	4·0	0·8
6H[a]	5·8	4·0
5B[a]	9·5	7·0
3K[a]	13·2	7·0
5C[a]	15·6	13·0
6E[a]	16·7	12·0

[a] Did not fail on {110}.

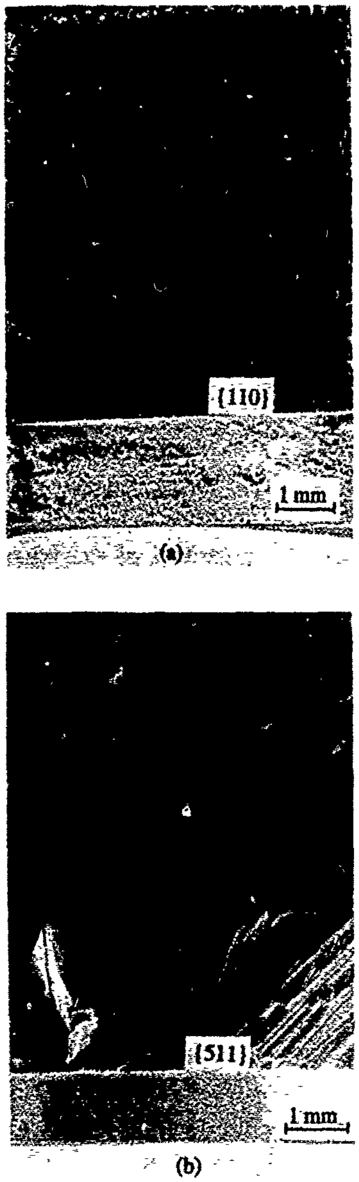

Fig. 23. Fracture surfaces of ⟨111⟩ oriented bend specimens tested (a) at ambient temperature and (b) at 400°C. A flat fracture surface without the {511} fracture facets is formed at ambient temperature. Transient fracture facets are observed on the fracture surface tested at 400°C.

3.5 Fracture toughness dependence

Table 3 lists the percentages of the projected area of the {110} fracture plane near the notch which failed by {511} cleavage in double cantilever beam specimens that were heat treated to get various degrees of fracture toughness.[7] It should be noted that the specimens with fracture toughness values in excess of 4 MPa$\sqrt{m}$ did not show final fracture by cleavage on the {110} plane normal to the stress axis. Final separation occurred by tearing-off of the specimen arms after excessive high-index cleavage. The data are normalized to the ideal surface area of the {110} plane perpendicular to the stress axis for comparison purposes. It is clear from the table that the extent of the {511} cleavage shows a strong correlation with fracture toughness and, therefore, with plastic deformation near the starter notch.

4 DISCUSSION

Cleavage fracture readily occurs in single crystals of most intermetallic compounds at ambient temperature since their DBTTs are usually high. This brittle fracture mode normally has a preferred cleavage plane of a low crystallographic index. The fracture surface is relatively flat and shiny with very few features except the river patterns that reflect the crack growth direction. Generally, cleavage fracture indicates limited plastic deformation and a low fracture toughness. Unlike FeAl, which cleaves on {100} planes, the cleavage plane for NiAl is not well defined. Prior to final cleavage on the {110} plane, which appears tc be the preferred cleavage plane in NiAl, cleavage on 'transient' fracture planes, such as {511} or {711}, is seen in NiAl. Although several investigators[5,8–11] have attempted to rationalize the {110} cleavage plane in NiAl on the basis of cleavage energy considerations, none of these considerations adequately explain the {110} and {100} planes in NiAl and FeAl, respectively. For example, the molecular dynamics simulations of the embedded atom method by Clapp *et al.*[11] predicted {100} to have lower surface energy in NiAl, while the first-principle calculations of Yoo and Fu[8] predicted lower cleavage energies for the {110} planes for both FeAl and NiAl. Chang *et al.*[5] tried to rationalize the {110} cleavage plane of NiAl and the {100} cleavage plane for FeAl on the basis of the degree of order and the number of broken bonds for these two aluminides. Our results show that, in NiAl single crystals, cleavage on low-index planes is observed only under special conditions. The fracture surface of NiAl single crystals consists of unique fracture facets when fractured below the DBTT. These facets were observed next to the notch root before the final fracture occurred on {110} cleavage planes. Laue X-ray diffraction, SEM and surface trace analysis have established that the transient fracture facets have a high crystallographic index near {511} under various test conditions and specimen orientations.

Like some other intermetallic compounds, the fracture toughness of binary NiAl is generally low. The reported fracture toughness values are dependent on the heat treatment, specimen configuration, crystallographic direction with respect to loading direction, and the orientation and geometry of the notch. Typically, a value of 8 MPa√ is obtained[1] for a specimen orientation in the ⟨100⟩ direction in a four-point bend test with a through notch; this decreases to 4 MPa√m in the ⟨100⟩ orientation. In a chevron-notch configuration, a value as high as 15 MPa√m is obtained in a ⟨100⟩-oriented bend specimen.[12] Recently,[7] the ductility and toughness in the ⟨110⟩-oriented NiAl single crystal were shown to be improved by minimizing strain-age embrittlement by fast cooling through the temperature range 400–20°C. Fracture toughness in the range 13–17 MPa√m was shown in ⟨110⟩-oriented double cantilever beam toughness specimens. Therefore, specimen and notch configuration, specimen heat treatment, and the test method should be specified when quoting fracture toughness values. Like ductility, the fracture toughness increases with temperature, as a result of increased plasticity at the tip of the growing crack. Data obtained at GE Aircraft Engines[2] indicate that the alloying elements which improve ductility also improve fracture toughness. The ductilizing additions of Fe and Ga, which increased the RT ductility of {110} single crystals, improved the RT fracture toughness by 50%, while 50% reduction in the RT fracture toughness is measured in high-strength NiAl alloys.[12]

Considerable plastic deformation is seen in the fracture steps bridging the {511} facets (Fig. 7). It is, therefore, possible that the occurrence of {511} facets is a result of some sort of slip interaction in front of the crack tip. It is possible to visualize localized deformation leading to slip bands, and microcracks nucleating at the intersections of these slip bands. The absence of {511} planes in explosively deformed specimens lends credance to this hypothesis. The results of our study of the influence of alloying additions, including defect hardening by stoichiometry deviations, on the formation of {511} transient fracture facets also confirm the mechanisms of formation of {511} facets by localized plastic deformation since their formation appears to be suppressed in alloys with low ductility. It is not clear, however, how and why deformation in the material favors the formation of {511} type planes. Based on the observations of fracture facets in the ⟨100⟩ oriented tensile specimens, Schneibel *et al.*[6] have suggested that the facets tend to occur on the plane of maximum shear stress. Since {511} or {711} planes are formed irrespective of the specimen orientation, therefore, an argument for higher resolved shear stress on these planes is difficult to apply to explain the formation of these particular planes. It is interesting to recall that localized deformation has been reported to occur along high-index planes in cube-oriented NiAl single crystals.[13] Hirsch *et al.*[14] rationalized the extent of stable crack growth ahead of the starter cracks in brittle materials by shielding induced by dislocations on slip planes remote from the crack tips. Although a similar analysis for this study may show large normal stress possible on the {511} planes, it would still not explain the peculiar susceptibility of these planes to cleavage.

The higher values for ⟨100⟩-oriented chevron-notched specimens can be explained by the orientation-dependence of the area fraction of the {511} fracture facets. The higher toughness for the ⟨100⟩ oriented chevron-notched specimen compared with the through-notched specimen results because the two specimen geometries fracture on different crystallographic planes. The chevron notched specimen fails on {511} or {711} planes which are near the normal to the ⟨100⟩ axis because of the constraints of the side grooves. The through-notched toughness specimen tends to fail along an angle 45° to the axis of the specimen on a {110} type plane. Fracture at an angle of greater than 10° to the normal invalidates the K-solution for this specimen as defined by ASTM E399. Therefore, the exact fracture toughness for the ⟨100⟩-oriented through-notched specimen is not known.

CONCLUSIONS

1. In NiAl single-crystal specimens, except in highly alloyed and explosively cracked specimens, the area in the fracture surface at and near the initiation point consisted of small facets; the crystallographic orientation of these facets was determined to be either {511} or {711}. The {511} planes were mostly observed, with occasional observation of the {711} planes.
2. In low-ductility NiAl alloys, the tendency to form high-index fracture facets is reduced.
3. The mechanism of high-index planes formation is not clearly understood. Prior deformation or crack-tip plasticity appear to promote cleavage along {511}. These facets are not present when NiAl is cracked under high strain rates.
4. Fracture toughness values and transient fracture planes are highly sensitive to specimen geometry, orientation, test technique, and the alloying additions, as well as to stoichiometry.

ACKNOWLEDGEMENTS

The authors would like to acknowledge R. T. Smith of GE Aircraft Engines for his excellent contribution and very tedious work in identifying the fracture facets by the Laue back-reflection technique. We would also like to acknowledge many stimulating discussions with R. D. Field, D. F. Lahrman, K. Bain, and W. S. Walston of GE Aircraft Engines, and J. H. Schneibel of the Oak Ridge National Laboratory. One of the authors (J.E.H.) wishes to acknowledge the support of the Office of Naval Research.

REFERENCES

1. Darolia. R., *J. Metals*, **43**(3), (1991) 44.
2. Darolia, R., Lahrman, D. F., Field, R. D., Dobbs, J. R., Chang, K-M., Goldman, E. H. & Konitzer, D. G., in *Ordered Intermetallics—Physical Metallurgy and Mechanical Behavior*, ed. C. T. Liu, R. W. Cahn and G. Sauthoff. *NATO ASI Ser. E: Applied Sciences*, **213** (1992) 679.
3. Darolia, R., Lahrman, D. F. & Field, R D., *Scripta Metall. Mater.*, **26** (1992) 1007.
4. Chang, K-M., Darolia, R. & Lipsitt, H. A, in *High-temperature Ordered Intermetallic Alloys IV*, ed. L. Johnson, J. O. Stiegler and D. P. Pope. *MRS Proc.*, **213** (1991) 597.
5. Chang, K-M., Darolia, R. & Lipsitt, H. A., *Acta Metall. Mater.*, **40** (1992) 2727.
6. Schneibel, J. H., Darolia, R., Lahrman, D. F. & Schmauder, S., *Metall. Trans.* (in press).
7. Hack, J. E., Brzeski, J. M. & Darolia, R., *Scripta Metall Mater.*, **27** (1992) 1259.
8. Yoo, M. H. & Fu, C. L., *Scripta Metall. Mater.*, **25** (1991) 2345.
9. Vehoff, H., to be published in *High-temperature Ordered Intermetallic Alloys V*, ed. I. Baker, R. Darolia, J. D. Whittenberger and M. H. Yoo. *MRS Proc.*, **288** (1993).
10. Vehoff, H., in *Ordered Intermetallics—Physical Metallurgy and Mechanical Behavior*, ed. C. T. Liu, R. W. Cahn and G. Sauthoff. *NATO ASI Ser. EL: Applied Sciences*, **213** (1992) 299.
11. Clapp, P. C., Rubins, M. J., Charpenay, S., Rifkin, J. A. & Yu, Z., in *High-Temperature Ordered Intermetallics Alloys III*, ed. C. T. Liu, A. I. Taub, N. S. Stoloff and C. C. Koch. *MRS Proc.*, **133** (1989) 29.
12. K. Bain, in *Intermetallic HP Turbine Technology Development, Phase I Interim Report.* Air Force Contract F 33615-90-C-2006, WL-TR-92-2016, AF Wright Laboratory, 1992.
13. Loretto, M. H. & Wasilewski, R. J., *Phil. Mag.*, **23** (1971) 1311.
14. Hirsch, P. B., Booth, A. S., Ellis, M. & Roberts, S. G., *Scripta Metall. Mater.*, **27** (1992), 1723.

Intermetallics 1 (1993) 79–80

Conferences

In this occasional Section, we shall offer particulars of the published proceedings of recent conferences concerned with intermetallics, and information about forthcoming conferences. We invite our readers to send to the chairman of editors information relating to both categories, to enable us to be as complete as possible in our coverage Some of the conferences cited in this Section may cover a range of topics extending beyond intermetallics.

PUBLISHED PROCEEDINGS

1. **Concerted European Action on Magnets (CEAM)**, a conference held in Madrid, Spain, in April 1988, sponsored by the Commission of the European Communities. (Devoted largely to intermetallics with permanent-magnet characteristics). Proceedings edited by I. V. Mitchell, J. M. D. Coey, D. Givord, I. R. Harris and R. Hantsch, published by Elsevier Applied Science, London and New York, in 1989. ISBN 1-85166-383-5.

2. **High Temperature Aluminides and Intermetallics**, a symposium sponsored by TMS and ASM and held in Indianapolis, 1–5 October 1989, at the TMS Fall Meeting, with support from Martin Marietta, GE and TMS. Proceedings edited by S. H. Whang, C. T. Liu, D. P. Pope and J. O. Stiegler, published by the Minerals, Metals and Materials Society (TMS), Warrendale, Pennsylvania, in 1990. ISBN 0-87339-117-9.

3. **High-Temperature Ordered Intermetallic Alloys IV**, Boston, 27–30 November 1990. Organized by the Materials Research Society, sponsored by the US Air Force Office of Scientific Research. Proceedings edited by L. A. Johnson, D. P. Pope and J. O. Stiegler, published as volume 213 of the Materials Research Society Symposium Proceedings, in 1991. (Materials Research Society, Pittsburgh, Pennsylvania).

4. **High Temperature Intermetallics**, a symposium sponsored and organised by the Institute of Metals, London, and held at the Royal Society, London, 30 April–1 May 1991, with support from the US Naval Research European Office. Preprints of invited talks published by the Institute of Metals in 1991.

5. **Intermetallic Compounds—Structure and Mechanical Properties (JIMIS-6)**, an international symposium organized by the Japan Institute of Metals, Sendai, and held in Sendai, 17–20 June 1991. Co-sponsored by 9 other societies. Proceedings edited by O. Izumi, and published by the Japan Institute of Metals, Aoba Aramaki, Sendai 980, in 1991.

6. **Ordered Intermetallics—Physical Metallurgy and Mechanical Behaviour**, Irsee, Germany, 23–28 June 1991. Sponsored by NATO, with support from the US Department of Energy, the Commission of the European Communities, and the US Naval Research European Office. Published as volume 213 of the NATO Advanced Study Institute Series (Series E: Applied Sciences), by Kluwer Academic Publishers, Dordrecht, Netherlands, Boston & London, in 1992. ISBN 0-7923-1726-2.

7. **Ordering and Disordering in Alloys**, European Workshop in Grenoble, France, 10–12 July, 1991. Sponsored by the Commission of the European Communities and the Centre National de la Recherche Scientifique. Proceedings edited by A. R. Yavari, and published by Elsevier Applied Science, London and New York, in 1992. ISBN 1-85166-762-8.

8. **International Conference on High-Temperature Aluminides and Intermetallics**, San Diego, California, 16–19 September 1991. Sponsored by ASM International. Edited by C. T. Liu, S. M. L. Sastry, D. P. Pope and S. H. Whang. Proceedings published in *Materials Science and Engineering*, **152A** (1992).

9. **Kinetics of Ordering Transformations in Metals**, a symposium sponsored by ASM International, held at the TMS-AIME Annual Meeting in San Diego, 4–5 March, 1992. Proceedings edited by H. Chen and V. K. Vasudevan and published by The Minerals, Metals and Materials Society (TMS), Warrendale, Pennsylvania, in 1992. ISBN 0-87339-187-X.

10. **Rare-Earth Magnets and Their Applications**, 12th International Workshop, together with **Magnetic Anisotropy and Coercivity in Rare-Earth Transition Metal Alloys**, 7th International Symposium, held in Canberra, Australia, 12–16 July 1992. Edited by Hi-Perm Laboratory, The University of Western Australia. In press, 1993.

© 1993 Elsevier Science Publishers Ltd, England. Printed in Great Britain

11. **Diffusion in Ordered Alloys and Intermetallic Compounds**, a symposium sponsored by the TMS and ASM, with support from the US Office of Naval Research and Oak Ridge National Laboratory, held at the TMS Annual Meeting in Chicago, 3–4 November 1992, Proceedings edited by B. Fultz, R. W. Cahn and D. Gupta, to be published by TMS, Warrendale, Pennsylvania, in 1993.

12. **High-Temperature Ordered Intermetallic Alloys V**, Boston, 30 November–3 December 1992. Organized by the Materials Research Society, sponsored by the Thayer School of Engineering (Dartmouth College), GE, NASA and Oak Ridge National Laboratory. Proceedings edited by I. Baker, R. Darolia, J. D. Whittenberger and M. H. Yoo, to be published as volume 288 of the Materials Research Society Symposium Proceedings, in 1993. (Materials Research Society, Pittsburgh, Pennsylvania).

FORTHCOMING CONFERENCES

1. **International Symposium on Structural Intermetallics**, organized and sponsored by the TMS, co-sponsored by 5 other societies. To be held at Seven Springs Mountain Resort, Champion, Pennsylvania, USA, 26–30 September, 1993. Inquiries to the chairman of the Organizing Committee, Dr R. Darolia, GE Aircraft Engines, Mail Drop M-89, Cincinnati, OH 45215, USA. For registration details contact TMS, 420 Commonwealth Drive, Warrendale, Pennsylvania 15086-7514, USA. Fax: +1 412 776 3770.

2. **Symposium on High-Temperature (Structural) Silicides and Refractory Alloys**, to be held at MRS Fall Meeting, Boston, 29 November–3 December 1993. Organizers: B. P. Bewlay, C. L. Briant, H. A. Lipsitt, J. J. Petrovic, A. K. Vasudevan. Inquiries to Bewlay or Briant, GE CRD, Fax: +1 518 387 7495.

3. **International Symposium on Intermetallic Compounds for High-Temperature Structural Applications**, in conjunction with the **3rd International SAMPE Symposium**, sponsored by the Japan Chapter of SAMPE, with support from MITL. To be held 7–9 December 1993, in the Nippon Convention Center (Makuhari Messe), Chiba, near Tokyo, Japan. MSS to be submitted before 31 August 1993. Inquiries to: Japan Chapter of SAMPE, Meguroeki Higashiguchi Bldg., 3-1-5 Kamiosaki, Shinagawa-ku, Tokyo 141, Japan. (Fax: +81 3 3445 8013).

4. **High-Temperature Intermetallics**, an international conference to be held at Hyatt Islandia Hotel, San Diego, California, to be organized by ASM International, 16–19 May 1994 Organizing committee: D. P. Pope, C. T. Liu, S. H. Whang. Abstracts to be submitted before 30 July 1993 to Prof. D. P. Pope, Dept. of Materials Science & Engineering, University of Pennsylvania, 3231 Walnut Street, Philadelphia, Pennsylvania 19104, USA. (Fax: +1 215 573 2128). Further details from ASM International, Materials Park, OH 44073–0002, USA. (Fax: +1 216 338 4634).

5. **International Conference on Nitromagnetics**, to be held in Honolulu, Hawaii, 15–17 June 1994. Inquiries to: Prof. H. Uchida, Department of Applied Physics, Tokai University, Hiratsuka, Kanagawa, 159-12, Japan.

6. **Thirteenth International Workshop on Rare-Earth Magnets**, and **Eighth International Symposium on Magnetic Anisotropy and Coercivity in Rare-Earth Transition Metal Alloys**, to be held in Birmingham, England, 11–15 September 1994. Inquiries to the chairman, Prof. I. R. Harris, School of Metallurgy and Materials, The University of Birmingham, Edgbaston, Birmingham B15 2TT, England. (Fax: +44 121 471 2267).

Intermetallics 1 (1993) 81

News item

THE CONCERTED EUROPEAN ACTION ON STRUCTURAL INTERMETALLICS (CEASI)

The Concerted European Action on Structural Intermetallics (CEASI) has been approved by the Commission of the European Communities, Brussels as a four-year programme from 1 November 1992. The aims of this programme are defined by the terms of reference of European-funded Concerted Actions and those for this specific programme are detailed below. Briefly, the aim of the CEASI programme is to coordinate research on intermetallic-based alloys throughout Europe in order to provide a platform for subsequent industrial development.

An industrial advisory board and a management board have been set up to define the mechanisms for coordinating research and to define topics for scientific meetings. The first topical meeting was held in Grenoble on 14 December 1992, when the membership of the management committee was also agreed. The membership of this management board is as follows:

Prof. M. H. Loretto (Chairman and main coordinator), IRC, University of Birmingham, UK.
Dr T. Khan (coordinator), ONERA, Paris, France.
Dr G. Sauthoff (coordinator), Max Planck Institute, Düsseldorf, Germany.
Prof. D. G. Morris, Neuchâtel, Switzerland.
Dr P. Threadgill, TWI, Abington, UK.
Prof. R. Wagner, GKSS, Germany.
Dr J. Ducszyck, Delft, Netherlands.
Dr A. Mazzarano, CSM, Rome, Italy.
Dr F. Moret, CENG, Grenoble, France.
Prof. M. D. Baró, Barcelona, Spain.

There are at present about 100 institutions which have shown interest in the CEASI programme and of these about 40 were represented at the first meeting which was attended by over 60 people. A quarterly newsletter will be sent out to all members of CEASI and anyone who has not registered their interest through earlier correspondence and who would like to become involved should write to the chairman of the coordinating committee so that they can be added to the address list for circulation of information. Address: Prof. M. H. Loretto, Director, IRC in Materials for High-Performance Applications, University of Birmingham, North Campus, Edgbaston, Birmingham, UK, B15 2TT. Fax: +44 (0)21 414 5232.

The objectives of the concerted action are as follows

(i) To provide a framework by which a coherent pre-competitive research programme can be carried out in Europe in the field of structural intermetallic-based alloys.
(ii) To ensure that there is a balance of activity in the research programme across the whole discipline, so that European intermetallics research goes ahead in a well-balanced way rather than in the incoherent way that it is proceeding at present.
(iii) To supply, process and circulate reference materials to participants where appropriate.
(iv) To develop a forum for discussion of research and exchange of information on these materials in order to ensure that European research, which is currently not focused, benefits through interaction on a peer basis and with an informed industrially-based group.
(v) To develop a fundamental understanding of alloying behaviour in intermetallics so that alloy development and alloy processing is on a firm basis for future application to the manufacture of components.

The principal tasks required to meet the objectives, to be financed by CEASI, are

(i) The formation of topical discussion groups to coordinate research activities in the areas: alloy development, property assessment and characterisation, material processing and fabrication, joining.
(ii) To arrange regular meetings to plan collaborative programmes, to exchange information and to receive advice from the industrial advisory board.
(iii) To institute a newsletter and research report, together with an appropriate circulation system.
(iv) To arrange short-term exchange visits of research personnel between participants.

Intermetallics 1 (1993)—© 1993 Elsevier Science Publishers Ltd, England. Printed in Great Britain

NOTES FOR AUTHORS

Submission of Papers

Original manuscripts may be submitted to any of the Editors, but the following procedure is preferred. Contributors in the Americas and China may submit their papers to Dr C. T. Liu, Metals and Ceramics Division, Oak Ridge National Laboratory, PO Box 2008 Oak Ridge, TN 37831-6115, USA, contributors from German-speaking countries to Dr G. Sauthoff, Max-Planck-Institut für Eisenforschung, Max-Planck-Str. 1, Postfach 140444, D-4000 Düsseldorf, Germany, contributors from Japan and Korea to Professor M. Yamaguchi, Department of Metal Science & Technology, Kyoto University, Sakyo-ku, Kyoto 606, Japan, contributors from the UK, continental Europe (other than German-speaking countries), and India to Professor R. W. Cahn, Department of Materials & Metallurgy, Cambridge University, Pembroke Street, Cambridge, CB2 3QZ, UK. Authors from other countries should submit to any editor. Editors will reach their decisions independently.

Submission of a paper implies that it has not previously been published in a journal and that it is not being simultaneously considered for publication elsewhere. Any necessary permissions for publication need to be secured prior to submission.

Upon acceptance of a paper, the author(s) will be asked to transfer the copyright of the paper to the publisher, Elsevier Science Publishers Ltd, Barking, Essex, UK. This transfer will ensure the widest possible dissemination of the information.

Types of Paper

(1) *Research Papers* (experimental or theoretical). An abstract and five key words are required.

(2) *Review Papers.* These will normally be invited by one of the Editors, but suggestions for topics and/or authors will be welcomed. Such suggestions should be sent to the Chairman of the Editors.

(3) *Short Communications* These should not exceed 1000 words and should have no more than three illustrations. A very brief abstract and five key words are required

(4) *Comments on papers published in* Intermetallics. Such comments will normally be published together with a reply from the author(s)

Disks

For papers produced using a word-processor of TEX, please submit a disk with the **final revised version** of the manuscript The file on disk should correspond exactly to the hard copy The operating system and the word-processor used should be specified clearly.

Illustrations or chemical structures in electronic format may be supplied provided that the file format and the program used to produce them is clearly indicated and that a hard copy is also supplied.

More detailed guidelines and further information are available from the publisher.

Preparation of Manuscripts

Three copies should be provided, in double-spaced typing, with a wide margin at the left. Generally, the length of the manuscript should be the minimum consistent with clarity. Each paper should be provided with an abstract 100–150 words and five key words for use in indexing. All papers should be written in English.

The title should be carefully chosen to reflect the contents as clearly as possible. A suggestion for a running title (less than 60 characters long) may be given. Names and addresses of the authors should follow the title and the author for correspondence should be indicated.

If possible the authors should consult an issue of the journal for style and layout. The editors and publishers reserve the right to adjust style in the interests of uniformity. The SI system (see, e.g. *Physics*, **146A** (1987) 1-68) should be used for all quantitative data, though values in other systems may be added in parentheses after the SI units if the authors consider it necessary Temperatures should be given in Celsius (°C) or Kelvin (K) scales. No full stop should be used in abbreviated units. Compound units should take the form, e.g m^2/s, *not* $m^2\ s^{-1}$. The meaning of **all** abbreviations should be spelled out in full when first used, with the abbreviations following in brackets.

Tables, the list of references and captions to illustrations should each appear on separate sheets at the end of the paper. Footnotes should be avoided

The use of proprietary names of alloys and instruments should be avoided as far as possible but may be accepted if the proprietary name is a universally known description of the category in question, e g. NIMONIC. Papers essentially of an advertising nature will not be accepted.

References

References to published work should be numbered sequentially in order of citation in the text and cited by superscript numerals without brackets, with a reference list in numerical order The list should give the authors' surnames and initials, contracted title of the periodical in italics or underlined (as in *World List of Scientific Periodicals* 4th edn, 1963-65), volume number in bold, and the initial page number of the cited paper. The title of books should be in italics or underlined, followed by the publisher, town and the year of publication. For collected works (e.g. conference proceedings), the editor's name should always be cited Reference to unpublished reports should only be made when no alternative published form can be located Typical examples of the correct style are

1. Baker, I., Schulson, E M. & Michael, J. R., *Phil Mag*., **B57** (1988) 379
2. Vedula, K., Hahn, K. H. & Boulogne, B., in *High Temperature Ordered Intermetallic Alloys 3.* MRS Symp. Proc. 133 (1989) 299
3. Yamaguchi, M., Nishtani, S. R. & Shirai, Y., in *High Temperature Aluminides & Intermetallics*, ed. S. H Whang *et al.* TMS, Warrendale, USA, 1990, p. 63.
4. Ananatharaman, T R. & Suryanarayana, C., *Rapidly Solidified Metals.* Trans Tech Publications, Aedermansdorf, Switzerland, 1987, p. 25

Illustrations

One *original* and two copies of each illustration should be provided Line drawings may be submitted in any medium providing that the image is black and very sharp. They should preferably require the same degree of reduction. Lettering should be large enough to be legible after reduction to fit a column width of 85 mm. Micrographs should always carry micron markers to show magnification. All illustrations should have the authors' names and figure number on the back. Colour printing is available, but the author will be required to pay for the printing cost.

Proofs

The selected author will receive a set of proofs for checking. No new material may be inserted in the text at the time of proof reading unless accepted by the Editors. All joint communications must indicate the name and full postal address of the author to whom proofs should be sent.

Page Charges and Offprints

There will be no page charges. Twenty-five offprints of each article will be supplied free of charge. Additional copies can be ordered at current printing prices.

ELSEVIER SCIENCE PUBLISHERS LTD
Crown House, Linton Road, Barking, Essex IG11 8JU, England